DEEP COLLAPSE MODE CAPACITIVE MICROMACHINED ULTRASONIC TRANSDUCERS

A DISSERTATION SUBMITTED TO
THE DEPARTMENT OF DEPARTMENT OF ELECTRICAL AND
ELECTRONICS ENGINEERING
AND THE INSTITUTE OF ENGINEERING AND SCIENCE
OF BILKENT UNIVERSITY
IN PARTIAL FULFILLMENT OF THE REQUIREMENTS
FOR THE DEGREE OF
DOCTOR OF PHILOSOPHY

By
Selim Olçum
December, 2010

I certify that I have read this thesis and that in my opinion it is fully adequate, in scope and in quality, as a dissertation for the degree of doctor of philosophy.

Prof. Dr. Abdullah Atalar(Supervisor)

I certify that I have read this thesis and that in my opinion it is fully adequate, in scope and in quality, as a dissertation for the degree of doctor of philosophy.

Prof. Dr. Hayrettin Köymen(Supervisor)

I certify that I have read this thesis and that in my opinion it is fully adequate, in scope and in quality, as a dissertation for the degree of doctor of philosophy.

Prof. Dr. Atilla Aydınlı

I certify that I have read this thesis and that in my opinion it is fully adequate, in scope and in quality, as a dissertation for the degree of doctor of philosophy.

Prof. Dr. Orhan Aytür

I certify that I have read this thesis and that in my opinion it is fully adequate, in scope and in quality, as a dissertation for the degree of doctor of philosophy.

Asst. Prof. Dr. Sanlı Ergün

I certify that I have read this thesis and that in my opinion it is fully adequate, in scope and in quality, as a dissertation for the degree of doctor of philosophy.

Asst. Prof. Dr. Coşkun Kocabaş

Approved for the Institute of Engineering and Science:

Prof. Dr. Levent Onural
Director of the Institute

Copyright Information

ABSTRACT

DEEP COLLAPSE MODE CAPACITIVE MICROMACHINED ULTRASONIC TRANSDUCERS

Selim Olçum
Ph.D. in Department of Electrical and Electronics Engineering
Supervisor: Prof. Dr. Abdullah Atalar
Supervisor: Prof. Dr. Hayrettin Köymen
December, 2010

Capacitive micromachined ultrasonic transducers (CMUTs) are suspended microelectromechanical membrane structures with a moving top electrode and a rigid substrate electrode. The membrane is actuated by electrical signals applied between the electrodes, resulting in radiated pressure waves. CMUTs have several advantages over traditional piezoelectric transducers such as their wider bandwidth and microfabrication methodology. CMUTs as microelectromechanical systems (MEMS), are fabricated using CMOS compatible processes and suitable for batch fabrication. Low cost production of large amount of CMUTs can be fabricated using already established integrated circuit (IC) technology infrastructure. Contrary to piezoelectrics, fabricating large 2-D arrays populated with transducer elements using CMUTs is low-cost. The technological challenges of CMUTs regarding the fabrication and integration issues were solved during the past 15 years, and their successful operation has been demonstrated in many applications. However, commercialization of CMUTs is still an overdue passion for CMUT community. The bandwidth of the CMUTs are inherently superior to their piezoelectric rivals due to the nature of the suspended membrane structure, however, their power output capability must be improved to achieve superior signal-to-noise ratio and penetration depth.

In this thesis, we gave a comprehensive discussion about the physics and functionality of CMUTs and showed both theoretically and experimentally that their power outputs can be increased substantially. Using the conventional uncollapsed mode of CMUTs, where the suspended membrane vibrates freely, the lumped displacement of the membrane is limited. Limited displacement, unfortunately, limits the power output of the CMUT. However, a larger lumped displacement is possible in the collapsed state, where the membrane gets in contact with the substrate. By controlling the movement of the membrane in this state, the power output of the

CMUTs can be increased. We derived the analytical expressions for the profile of a circular CMUT membrane in both uncollapsed and collapsed states. Using the profiles, we calculated the forces acting on the membrane and the energy radiated to the medium during an applied electrical pulse. We showed that the radiated energy can be increased drastically by utilizing the nonlinear forces on the membrane, well beyond the collapse voltage.

Using the analytical expressions, we developed a nonlinear electrical equivalent circuit model that can be used to simulate the mechanical behavior of a transmitting CMUT under any electrical excitation. Furthermore, the model can handle different membrane dimensions and material properties. It can predict the membrane movement in the collapsed state as well as in the uncollapsed state. In addition, it predicts the hysteretic snap-back behavior of CMUTs, when the electric potential across a collapsed membrane is decreased. The nonlinear equivalent circuit was simulated using SPICE circuit simulator, and the accuracy of the model was tested using finite element method (FEM) simulations. Better than 3% accuracy is achieved for the static deflection of a membrane as a function of applied DC voltage. On the other hand, the pressure output of a CMUT under large signal excitation is predicted within 5% accuracy.

Using the developed model, we explained the dynamics of a CMUT membrane. Based on our physical understanding, we proposed a new mode of operation, the deep collapse mode, in order to generate high power acoustic pulses with large bandwidth (>100% fractional) at a desired center frequency. We showed both by simulation (FEM and equivalent circuit) and by experiments that the deep collapse mode increases the output pressure of a CMUT, substantially. The experiments were performed on CMUTs fabricated at Bilkent University by a sacrificial release process. Larger than 3.5 MPa peak-to-peak acoustic pulses were measured on CMUT surface with more than 100% fractional bandwidth around 7 MHz using an electrical pulse amplitude of 160 Volts. Furthermore, we optimized the deep collapse mode in terms of CMUT dimensions and parameters of the applied electrical pulse, i.e., amplitude, rise and fall times, pulse width and polarity. The experimental results were compared to dynamic FEM and equivalent circuit simulations. We concluded that the experimental results are in good agreement with the simulations. We believe that CMUTs, with their high transmit power capability in the deep collapse mode can become a strong competitor to piezoelectrics.

Keywords: Capacitive Micromachined Ultrasonic Transducers, CMUT, MEMS, Equivalent circuit, Collapse mode, Deep collapse, Microfabrication, Sacrificial release process, Deflection of circular plates, Underwater CMUT.

ÖZET

DERİN ÇÖKME MODUNDA KAPASİTİF MİKROİŞLENMİŞ ULTRASONİK ÇEVİRİCİLER

Selim Olçum
Elektrik Elektronik Mühendisliği Bölümü, Doktora
Tez Yöneticisi: Prof. Dr. Abdullah Atalar
Tez Yöneticisi: Prof. Dr. Hayrettin Köymen
Aralık, 2010

Kapasitif Mikroişlenmiş Ultrasonik Çeviriciler (CMUT), yüzey üzerinde askıda duran, mikro-elektromekanik (MEMS) zar yapılarıdır. CMUT'ların mekanik zara ve alttaşa entegre olmak üzere iki adet elektrotları bulunur. Elektrotlara uygulanan elektriksel sinyaller sayesinde uyarılan zar, hareket eder ve ortama akustik dalgalar yayar. CMUT'ların, piezoelektrik çeviricilerle karşılaştırıldıklarında, geniş bantlı olmaları gibi ve üretim teknolojisinin getirdiği (çok elemanlı diziler, CMOS uyumluluğu, seri üretim) avantajları vardır. Üretim ve elektronik entegrasyon ile ilgili teknolojik zorluklar ve problemler geçtiğimiz 15 yıl içerisinde çözülmüş ve birçok uygulama CMUT'lar kullanılarak başarı ile sonuçlandırılmıştır. Fakat CMUT'ların ticarileşmesi henüz gerçekleşmemiştir. Her nekadar zar yapılarının özelliği sayesinde geniş bantlı olsalar da, piezoelektriklere göre üstün bir sinyal-gürültü oranı ve çalışma derinliği elde edilebilmesi için çıkış güçlerinin artırılması gerekmektedir.

Bu tezde, CMUT'ların fiziği ve fonksyonları ile ilgili daha geniş kapsamlı bir analiz sunuyoruz. Bu analizi kullanarak CMUT çıkış güçlerinin önemli ölçüde arttırılabileceğinin deneyini yapıyoruz. Literatürde, CMUT'ların bükülme profillerinin analitik bağıntıları sadece çökmemiş zarlar için verilmektedir. Fakat, çökmüş bir zar kullanılarak daha fazla bir toplam bükülme elde edilebilir. Zarın çökmüş haldeki hareketi kontrol edilerek, çeviricinin çıkış gücü arttırılabilir. Bu tezde, yuvarlak zarlar için bükülme profilinin analitik bağıntıları çökmüş ve çökmemiş halde iken türetilmiştir. Bu profiller kullanılarak, zar üzerine etki eden kuvvetler bulunmuş ve bir elektriksel darbe uygulandığında, zarın ortama yayacağı enerji hesaplanmıştır. Sonuç olarak, çökme geriliminin çok üzerinde oluşan doğrusal olmayan kuvvetler kullanılarak, zarın yayacağı akustik enerjinin önemli ölçüde arttırılabileceği belirlenmiştir.

Elde edilen analitik bağıntılar kullanılarak doğrusal olmayan bir eşdeğer dev-re modeli geliştirilmiştir. Bu model kullanılarak yürütülen benzetimler ile herhangi bir elektriksel uyarı ile yayın yapan bir CMUT'ın mekanik davranışı belirlenebilmektedir. Öte yandan, model, farklı zar boyutlarını ve malzeme özelliklerini de kullanabilmekte ve zar hareketini, zarın çökmüş ve çökmemiş iken belirleyebilmektedir. Ayrıca, CMUT'ların hizterez özelliği de model tarafından öngörülebilmektedir. Doğrusal olmayan bu model, bir SPICE devre benzetimi kullanılarak uygulanmış ve modelin doğruluğu sonlu eleman metodu (FEM) kullanılarak sınanmıştır. Buna göre, zarın DC gerilimler altında durağan bükülmesi %3'ten daha iyi bir hassasiyet ile belirlenebilmiştir. Diğer taraftan, zara yüksek gerilimli bir darbe uygulandığında oluşan basınç dalga şekli, %5'ten daha iyi bir hassasiyet ile hesaplanabilmektedir.

Geliştirilen eşdeğer devre modeli kullanılarak, CMUT zarlarının dinamiklerini anlayabiliyoruz. Oluşturulan fiziksel anlayış temel alınarak, CMUT'lardan istenen frekansta geniş bantlı ve yüksek güçte bir basınç darbesi elde etmek amacıyla derin çökme modunu öneriyoruz. Bu yeni mod ile CMUT'ların çıkış güçlerinin önemli ölçüde arttırılabileceği, benzetim modelleri (eşdeğer devre ve FEM) kullanılarak ve deneysel olarak gösterilmiştir. Deneyler, Bilkent Üniversitesi'nde üretilen CMUT'lar kullanılarak gerçekleştirilimiştir. 160V genliğinde bir elektriksel darbe kullanılarak, yaklaşık 7 MHz etrafında 100% oransal bantlı ve 3.5 MPa'dan daha büyük basınç darbeleri ölçülmüştür. Öte yandan derin çökme modunu eniyileştiren CMUT boyutları ve elektriksel darbe özellikleri belirlenmiştir. Deneysel sonuçlar ve benzetim sonuçları karşılaştırılmış ve sonuçların uyumlu olduğu anlaşılmıştır. Bu tez sonucunda anlaşılmıştır ki, derin çökme modu kullanılarak CMUT'ların çıkış güçleri kontrollü bir şekilde ve önemli miktarlarda arttırılabilir ve dolayısıyla piezoelektrik çeviricilere karşı daha güçlü bir rakip olabilirler.

Anahtar sözcükler: Kapasitif Mikroişlenmiş Ultrasonik Çeviriciler, CMUT, MEMS, Eşdeğer Devre, Çökme Modu, Derin Çökme, Mikro-fabrikasyon, Dairesel Plakaların Bükülmesi, Sualtı CMUT.

Acknowledgement

This thesis would not have been possible without the collaboration of many wonderful people and without the financial supports of ASELSAN and TÜBİTAK. I would like to thank and express my gratitude to those who have contributed to this thesis in any way.

During my graduate school at Bilkent University, I have always felt privileged and fortunate to find the opportunity to work with my two advisors Professor Abdullah Atalar and Professor Hayrettin Köymen. I first met Prof. Atalar when I was a senior undergraduate student in 2003. It was an honor for me to work with him through all these years and benefit from his knowledge and experience. He has made available his experience in a number of ways other than my thesis topic, like his virtue as an ethical academician. Unfortunately for me, one time period of a Ph.D. study is definitely not enough to get exposed to all his knowledge in a wide variety of subjects. I first started working with Prof. Köymen in 2006. I benefited immensely from his extensive knowledge in the field of acoustics and transducers. I must thank him here for his confidence in me and letting me to manage the two research projects we have completed during my graduate study. I feel very fortunate, since I found the opportunity to work with him at his industrial projects. I believe, such experience i gathered from him will be indispensable for me during my professional development, not only as a researcher, but also as a professional engineer. I am grateful to him, because in addition to being a knowledgable advisor, he was an incredible mentor to me in every aspect of life. I will always feel indebted for my advisors' continuous support and encouragement during my graduate school. I sincerely hope that my friendship and collaboration with them endure in the future.

It was an honor and privilege for me to receive "ASELSAN Fellowship" award to support my dissertation during the last two years of my Ph.D. study. I believe, the fellowship constitutes the foundation of a long standing collaboration with ASELSAN for the upcoming years of my professional life.

This thesis would not have been possible without the financial support of

TÜBİTAK. Project grants 105E023 and 107T921 of TÜBİTAK provided the resources used for the experiments in this thesis. On the other hand, I received "National Scholarship for Ph.D. Students" and "International Research Fellowship" supports from TÜBİTAK during my graduate study. Especially, "International Research Fellowship" contributed greatly to my technical skills, which were proved very useful for the experimental work in this thesis.

I am grateful to Professor Atilla Aydınlı for his friendship and support during all these difficult years of my graduate student life. I met Prof. Aydınlı at his Physics 101 course at my freshman year at Bilkent. Since then, he has become an invaluable mentor and friend to me. He was always there for a quick chat or discussion or a solution about any problem I may face. He may show up in the middle of the night with his tools at hand and pyjamas on, to fix a broken door lock. For that and many others, I owe my deepest gratitude to him. I know that my friendship with him will endure for many years to come.

It was a pleasure to meet Orhan Aytür during the years I have been at Bilkent University. I took the best lectures at Bilkent from him and enjoyed his Photonics course and learned a lot. I am grateful to him for his warm friendship and also for being a supportive member of my Ph.D. qualification and Ph.D. thesis committees. I am sure he will be one of my long lasting friends in the many years to come.

I would like to thank Professor Levent Değertekin for accepting me as a visiting scholar to his group in Georgia Tech. My stay in his group contributed immensely to my professional development. I must acknowledge his financial support for the training and time in clean-room facilities, through which I excelled on microfabrication techniques and methodologies.

Aşkın Kocabaş was my first mentor in the cleanroom. I still miss the small chatting/gossipping sessions over coffee. The time we have spent together working on our creative projects, was definitely some of the best times at Bilkent for me. I hope to be close to him in the future for his valuable friendship and collaboration.

Niyazi Şenlik also deserves special thanks for being a close friend and original personality in the lab. He was my mentor for FEM simulations. In the first years,

we were the two graduate students of Prof. Atalar working on CMUTs. Much of this thesis would not be possible without his collaboration. I will always value him for being a close friend during the hard times.

I would like to thank to our collaborators, Dr. Ayhan Bozkurt and Yalçın Yamaner. Their collaboration made this thesis possible.

Below, I would like to thank all my friends and colleagues I have worked together for their companionship and collaboration throughout these years: Celal Alp Tunç, Ali Bozbey, Haydar Çelik, Ateş Yalabık, Sinan Taşdelen, Hamdi Torun, Kağan Oğuz, Elif Aydoğdu, Vahdettin Taş, Jaime Zahorian, Rasim Güldiken, Deniz Aksoy, Ertuğrul Karademir, Aslı Ünlügedik, Ceyhun Kelleci, Burak Köle, Münir Dede, Can Bayram, Mehmet Emin Başbuğ, Alper Özgürlük... I am sure that the list is incomplete.

I would like to thank our department chair Professor Ayhan Altıntaş and previous department chair Professor Bülent Özgüler for their support. I must not forget to thank our department secretary, Ms. Mürüvet Parlakay for her amazingly simple solutions and help. I acknowledge the support and friendship of our technicians Ergün Hırlakoğlu and Ersin Başar.

I want to include special thanks to the Advanced Research Lab technical staff, Murat Güre and Ergün Karaman for their sincere efforts for keeping the cleanroom operational at all times. I know, I was a pain for them, always complaining and finding something wrong in the lab, but they have never disregarded my requests and opinions. For that I am grateful to them.

I would like to thank our deputy manager of the procurement office, Serdal Elver, for his incredible effort and talent at his job. For the many years I have been at Bilkent, I bothered him a lot for an emergency purchase of some critical component or chemical. Not to mention the warm chats at his office, he was always creative and fast in solving my problems.

I would like to thank VAKSİS for their wonderful PECVD system we use in the cleanroom for low stress nitride membrane fabrication. I am sure, this work would not have been possible without this equipment.

I would like to thank all my teammates in soccer team Emekliler (the Champion of Bilkent), which made the evenings more fun and relaxing for me during the soccer tournaments.

I would like to thank my brother, Evrim, my parents, and my in-laws for their loving support and encouragement.

And the last, but definitely not the least, I am deeply indebted to my wife, Gökçe, for her endless support and love despite all the days and nights spent in the labs. I hope all this effort and time bring us a happy and a meaningful life, together, always...

Selim Olçum

Contents

List of Figures

List of Tables

Chapter 1

Introduction

Capacitive micromachined ultrasonic transducers (CMUTs) are first introduced as air transducers [1, 2] in 1994. Due to their lower mechanical impedances compared to piezoelectrics, they immediately attracted attention for airborne applications [3]. The development of the first fabrication technology for immersion CMUTs [4] with sealed cavities has been followed by a successful demonstration of CMUTs as an alternative transducer with large bandwidth [5] and suitability for integration with electronics [6–8]. Large numbers of CMUTs can be fabricated on the same wafer on a commercial production, resulting in reduced costs compared to its piezoelectric alternatives. In addition, CMUT technology can be used to manufacture transducer arrays integrated with driving electronic circuits.

CMUTs are micromachined suspended membrane structures with a moving top electrode and a rigid substrate electrode. Fabrication of CMUTs requires a number of processing steps [9]. Integrated circuit manufacturing technology enables CMUTs to be produced in different sizes and shapes using basic lithography techniques. The difficulties in the fabrication processes have been gradually solved and several different approaches have been proposed during the last decade. Basically the fabrication approaches of a suspended membrane structure can be discussed in two different technologies: sacrificial release [4] and wafer bonding [10]. Standard MEMS fabrication processes utilizing the sacrificial release process, e.g., PolyMUMPS [11], are utilized for fabrication of CMUT structures [12–14]. However, using such processes, sealing the cavity underneath the membrane is not possible. Therefore, such CMUTs suffer from squeezed film damping effects in air. Using these CMUTs in immersion applications is not possible. Other problems of the sacrificial release processes, e.g., membrane stress [15, 16], etch selectivity of the release chemicals [17], sealing [4, 17, 18] are solved consecutively by several university labs. However, the material parameter variations of deposited thin film membranes from batch to batch is a drawback for a PECVD or LPCVD deposited membrane. In addition, poor thickness uniformity compared to wafer bonding limits the performance of CMUTs in a high-Q sensing application [19, 20]. On the other hand, wafer bonding technology [10] solves these problems using the top silicon layer of a silicon-on-insulator (SOI) wafer as the membrane, which has a better thickness uniformity [9]. In addition, the material properties of a SOI wafer are well known, which make the design implementation more successful. The wafer bonding process, however, suffers from the conductive silicon membrane, since no electrode patterning can be performed on the membrane. Therefore, patterned electrode structures such as half electrode implementation [21] or dual-electrode CMUTs [22] are not possible with SOI wafer bonding. The engineering of the membrane itself, as in the case of a nonuniform membrane [23], would bring nonuniformity problems [24] as in the case of a surface micro-fabrication technology. High parasitic capacitance due to the conductive membrane in wafer bonded CMUTs can be solved by bonding a dielectric wafer instead of SOI as the membrane at the expense of uniformity [25]. Recently, the problem with the parasitic effects in a wafer bonding technology has been solved [26], by utilizing a SOI wafer with a thick buried oxide layer at the expanse of fabrication complexity.

Successful electronics integration of CMUTs fabricated by both the sacrificial release [6–8] and wafer bonding technology [27] have been demonstrated during the past decade. The advantage of CMUTs compared to piezoelectrics is proven with the implementation of highly integrated 2-D arrays [28], sophisticated catheter applications [29] and flexible transducers [30].

The technological aspects and drawbacks of CMUT fabrication and integration processes are not the focus of this thesis. The short discussion above is given to demonstrate that the technological problems of CMUTs were already solved or being solved. We believe that other technological problems can be solved by large commercial fabs if large quantities of CMUTs are to be fabricated.

During the past 15 years, CMUTs' unique capabilities have been implemented in many ultrasonic applications — e.g. medical imaging [31–36], high intensity focused ultrasound for therapeutics [37,38], intravascular ultrasound (IVUS) [39,40], intracardiac ultrasound [29, 41], diagnostics [42], minimally invasive ultrasound [43, 44], photo-acoustic imaging [45,46], elasticity imaging [47], airborne ultrasound [48], microphones [49]. The commercialization of CMUTs in one of the above applications, however, is an overdue passion for CMUT community. It is obvious that such a delay is not because of the technological problems, but because of economic reasons. "In order to achieve reliable and robust manufacturing of semiconductor-based microsystems, hundreds of wafers need to be fabricated" [50]. For commercialization in several of the above applications to achieve such a turnover, the performance of the CMUTs should not only be competitive to their piezoelectric rivals, but should be much superior. The bandwidth of the CMUTs are inherently superior to piezoelectrics due to the nature of a suspended membrane structure. The power output capability of CMUTs, on the other hand, must be improved to provide such superiority, as well. In this thesis, we will give a comprehensive discussion about the physics and functionality of CMUTs and show that their power outputs can be immensely increased.

When immersed in a liquid medium, CMUTs are capable of generating wideband acoustical pulses with more than 100% fractional bandwidth [23]. Ultrasound applications, however, require high transmit pressures for increased penetration depth and signal-to-noise ratio, as well as large bandwidth. For therapeutic applications higher output pressures are necessary for faster heating in the tissue. However, output power limitations of CMUTs when compared to piezoelectrics have been their major drawback since they have first been introduced. During the past decade several attempts have been made to increase the power output of the CMUTs. It has been demonstrated that use of rectangular membranes increases the fill-factor and hence the output pressure [51]. Dual electrode structures introduced by Güldiken et. al. [22] also improved the pressure output of the CMUTs by increasing the electromechanical coupling coefficient and displacement. Collapse mode of operation has boosted the pressure output considerably [52–54]. However, collapse mode of operation has been investigated using FEM simulations [55] and lacks accurate models for understanding the mechanics and the limits of the mode.

The efforts for simulating and modelling CMUTs have started with the development of an equivalent circuit model [5] based on Mason's equivalent circuit for electro-acoustic devices [56]. Different models for defining the equivalent circuit elements are available in the literature [57–64]. However, finite element method (FEM) simulations are still needed [65] in order to simulate the CMUT operation including the nonlinear effects [66], medium loading [67–69], cross talk [70–72], the effect of the higher order harmonics [73] and for determination of the CMUT parameters [74–77]. Recently, fully analytical models were developed for fast and efficient results of frequency response analysis [57, 78].

FEM simulation packages —e.g., ANSYS— are powerful tools and extensively used for the analysis of CMUTs. FEM analysis predicts the performance of a particular design very well and hence it is a very good testing and tuning tool. However, the computational expense required for the solution makes FEM tools unsuitable for using them in design stage. For instance, transient dynamic analysis of a CMUT is crucial in order to understand the nonlinear behavior of the CMUT, however, it has high computational cost and requires many cycles to reach the steady state. It does not rapidly respond when a parameter is altered and hence, an idea about its effect cannot be instantly grasped by the designer. Calculated design charts for large array of circular CMUTs are available in the literature [58] but lack the nonlinear effects when the CMUTs are driven in collapse mode.

In this thesis, we will develop an electrical equivalent circuit model that can be used to simulate the mechanical behavior of a transmitting CMUT under any electrical excitation. The model is dependent on membrane dimensions and mechanical properties and it can predict the membrane movement in the collapsed state as well as in the uncollapsed state. The model utilizes analytical expressions of a deflected CMUT membrane in uncollapsed and collapsed states, which were derived using the general differential equations of Timoshenko [79] for circular plates. Using the developed model we will clarify the dynamics of a CMUT membrane under any electrical excitation. Based on the physical understanding, we will propose a new operation mode, *the deep collapse mode*, in order to generate high power acoustic pulses with high bandwidth at a desired center frequency.

We will show that the output pressure of a CMUT can be increased considerably by using the deep collapse mode. We will verify the results of our analytical approach using FEM simulations. We will demonstrate the use of the deep collapse mode with experiments performed on fabricated CMUTs.

Chapter 2

Deflection of a Clamped Circular Membrane

CMUTs have two electrodes: a top electrode in the membrane and a bottom electrode in the substrate. When an electric potential is applied between the top electrode and the bottom electrode, the membrane deflects due to the electrostatic attraction force. The static deflection profile of a membrane as a function of applied voltage is central to understanding and modelling CMUT behavior. Initially such calculations were performed using FEM simulations for the uncollapsed and collapsed states of a CMUT membrane. More recently, other numerical and analytical methods were developed for CMUT deflection in the uncollapsed state. In this chapter, we will combine the previously developed methods for uncollapsed state with our approach for collapsed state membrane deflections. We will extend our calculations for the deflections due to an electric potential. Finally, we will assess the use of lumped parameters for representing the membrane state and forces.

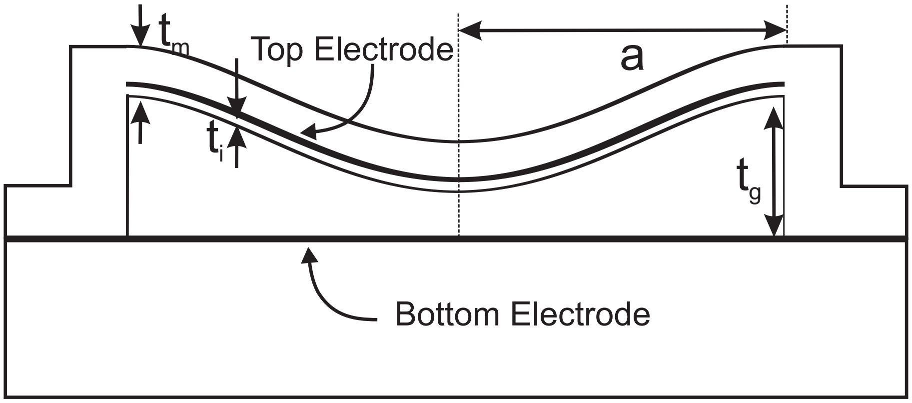

Figure 2.1: Cross sectional view of an uncollapsed clamped circular membrane with radius a, thickness t_m and gap height of t_g. The top electrode is at a distance t_i above from the gap. The bottom electrode is assumed to be at the top of the substrate.

2.1 Uncollapsed State of a Membrane

In the conventional operating regime of a CMUT, which was introduced in [1] and detailed in [5], the membrane vibrates without touching the substrate. A cross sectional view of an uncollapsed deflected membrane is shown in Fig. 2.1. The deflection of the membrane toward the substrate is the result of two forces: the atmospheric pressure on the membrane (since there is a vacuum in the cavity underneath the membrane) and the electrostatic attraction force generated by the applied electric potential between the electrodes. In this section, we will calculate the deflections caused by both sources.

The expression for the deflection, $x(r)$, of a clamped circular membrane, with radius, a and thickness, t_m as a function of radial distance, r, under uniform pressure, P, was derived by Timoshenko [79] (p. 55) as follows:

$$x(r) = \frac{P}{64D}(a^2 - r^2)^2 \tag{2.1}$$

where D, the flexural rigidity of the membrane, is defined as:

$$D \equiv \frac{Et_m^3}{12(1-\nu^2)} \tag{2.2}$$

and E is the Young's modulus and ν is the Poisson's ratio of the membrane material. The deflection of a membrane under atmospheric pressure is determined when P

in (2.1) is replaced with atmospheric pressure, P_0, which is approximately 100 kPa at sea level.

The average displacement, x_{avg} of a membrane with radius, a and a deflection profile $x(r)$ is defined as:

$$x_{avg} \equiv \frac{1}{\pi a^2} \int_0^{2\pi} \int_0^{a} x(r)\, r\, dr d\theta \tag{2.3}$$

When the definition in (2.3) is evaluated for the case of an uncollapsed membrane deflected by a uniform pressure, P, the average displacement can be expressed as follows as given in [78]:

$$x_{avg} = \frac{Pa^4}{192D} \tag{2.4}$$

However, average displacement measure is problematic in some cases [80]. For example, higher harmonic deflection profiles may generate zero average displacement, which will in return result infinite radiation impedance. In order to handle such cases, we define the root mean square (rms) displacement for the same membrane as follows:

$$x_{rms} \equiv \sqrt{\frac{1}{\pi a^2} \int_0^{2\pi} \int_0^{a} x^2(r)\, r\, dr d\theta} \tag{2.5}$$

We will discuss the choice of the lumped displacement measure later in this thesis. When the definition in (2.5) is evaluated for the uncollapsed state, the rms displacement can be expressed as follows:

$$x_{rms} = \frac{Pa^4}{64\sqrt{5}D} \tag{2.6}$$

Above expressions are valid when the load on the membrane is a uniformly distributed force. The electrostatic attraction force due to an applied electrical potential, however, is not uniform since the separation between the electrodes is not constant throughout the radial distance, r. An accurate method for calculating the deflection profile of an uncollapsed membrane deflected by an applied electric potential was developed by Nikoozadeh et.al. [81]. The method partitions the membrane into rings and calculates the deflection as a superposition of the displacements caused by the point loads at the corresponding rings. The deflection profile caused by the loads on the rings are calculated using the expressions derived by Timoshenko [79] (p.64):

$$x(r) = \sum_{i=1}^{N} \begin{cases} \frac{F_i}{8\pi D}\left[\frac{(a^2+r^2)(a^2-a_i^2)}{2a^2} + (a_i^2+r^2)ln\frac{a_i}{a}\right], & a_i < r; \\ \frac{F_i}{8\pi D}\left[\frac{(a^2-r^2)(a^2+a_i^2)}{2a^2} + (a_i^2+r^2)ln\frac{r}{a}\right], & a_i \geq r. \end{cases} \tag{2.7}$$

where F_i is the electrostatic attraction force between the electrodes at the i^{th} ring and a_i is the axial distance of force F_i to the center. The value of the force, F_i is calculated as the force between the electrodes of a parallel plate capacitor at i^{th} ring when an input voltage, V_{in} is applied. After finding the deflection using superposition, the calculation is continued iteratively updating the gap, t_g, —thus electrostatic forces, F_i— until the deflection converges. If the result of the iterations does not converge, the applied voltage is larger than the collapse voltage. This method cannot be used when the membrane is in contact with the substrate since in that case the deflection profile cannot be expressed as linear combination of the loads on the rings. In addition, the deflection profile cannot be expressed as a function of the applied electric potential, V_{in}, which makes the use of such a method in an equivalent circuit impossible.

2.2 Collapsed State of a Membrane

The deflection profile expression in (2.1) and (2.7) are valid as long as the membrane does not touch the substrate. A different general solution and set of boundary conditions must be utilized for the calculation of the profile when the center region of a membrane touches the substrate (Fig. 2.2). We will use the general solution for the deflection of a uniformly loaded collapsed circular plate derived by Timoshenko [79] (p. 309) as the starting point:

$$x(r) = C_1 + C_2 \ln r + C_3 r^2 + C_4 r^2 \ln r + \frac{r^4}{64D} P \quad \text{for} \quad b \leq r \leq a \tag{2.8}$$

where b is the contact radius. We applied boundary conditions to (2.8), which characterize the deflected shape of a collapsed and clamped membrane:

$$x(a) = 0 \quad x(b) = t_g \tag{2.9}$$

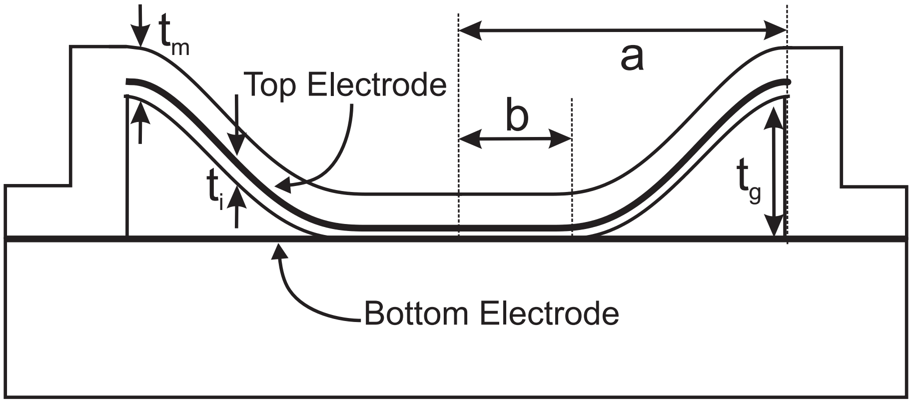

Figure 2.2: Cross sectional view of a collapsed clamped circular membrane with radius a, thickness t_m and gap height of t_g. The top electrode is at a distance t_i above from the gap. b is the contact radius. The bottom electrode is assumed to be at the top of the substrate.

$$\left.\frac{dx(r)}{dr}\right|_{r=a} = 0 \quad \left.\frac{dx(r)}{dr}\right|_{r=b} = 0 \tag{2.10}$$

$$M_r(b) = -D\left.\left(\frac{d^2x(r)}{dr^2} + \frac{\nu}{r}\frac{dx(r)}{dr}\right)\right|_{r=b} = 0 \tag{2.11}$$

where M_r is the radial bending moment on the membrane. b is determined by solving (2.11) in terms of the four unknown constants of (2.8) which in turn were determined using the four boundary conditions of (2.9) and (2.10). Since the boundary conditions are defined at radial distances a and b, solution to (2.8) is valid between b and a. The deflection of the membrane from 0 to b is equal to the gap height, tg.

The deflection profiles calculated using (2.1) and (2.8) are plotted in Fig. 2.3 (dashed) along with ANSYS simulation results (solid) for different applied uniform pressures. The deflection profile of a clamped membrane under the excitation of a uniform pressure can be well approximated using analytical solutions for both uncollapsed and collapsed states.

The average displacement of a collapsed membrane with the corresponding dimensions is calculated using the definition in (2.3) and the solution of (2.8) as:

$$x_{avg} = \frac{b^2}{a^2}t_g + \frac{2}{a^2}\int_b^a r\,x(r)\,dr \tag{2.12}$$

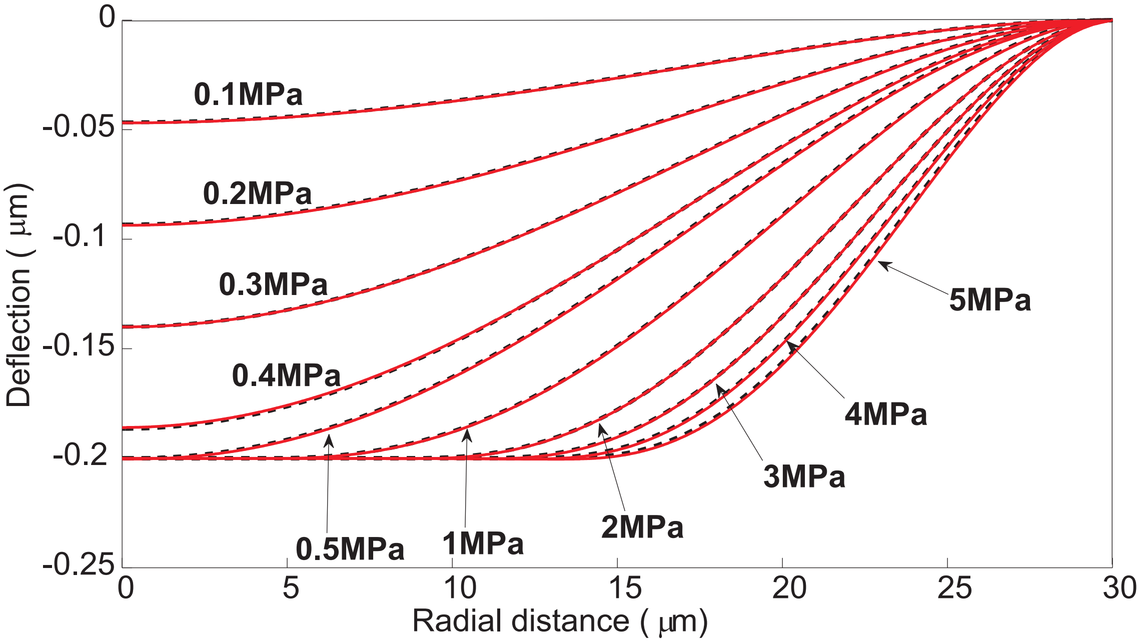

Figure 2.3: Comparison of deflection profiles obtained by (2.1) and (2.8) (dashed curves) with electrostatic FEM simulations (solid curves). Values of the uniform pressure applied on the membrane are indicated for each curve in the figure. The dimensions of silicon nitride membrane: a=30 μm, t_m=1.4 μm, t_i=0.4 μm and t_g=0.2 μm. Material parameters used for silicon nitride is given in Table A.1.

To simplify the expression in (2.12), we define

$$X_a(r) \equiv \frac{2}{a^2}\int_0^r \rho\, x(\rho)\, d\rho \tag{2.13}$$

We find using (2.8)

$$X_a(r) = \frac{r^2}{a^2}\left(C_1 + \frac{C_2}{2}(2\ln r - 1) + \frac{C_3 r^2}{2} + \frac{C_4 r^2}{2}(\ln r - 1/4) + \frac{r^4}{192D}P\right)$$

Hence from (2.12), we find the nonlinear relationship between the average displacement and the applied pressure as:

$$x_{avg} = \frac{b^2}{a^2}t_g + X_a(a) - \frac{b^2}{a^2}X_a(b) \tag{2.14}$$

Root mean square displacement of a collapsed membrane, on the other hand, is calculated numerically using the deflection profile and a numerical integration of the equation in (2.5).

Above expressions for the collapsed state are valid as long as the forces are uniformly distributed over the surface. Since the separation of the electrodes of a CMUT is not constant throughout the cavity, the electrostatic force on a CMUT membrane is not uniformly distributed, making the derivation of an analytical expression for membrane deflection very difficult, if not impossible. Expressing the deflection as the superposition of point loads on a membrane as in the case of uncollapsed state is not possible due to the nonlinear nature of the collapsed state.

2.3 Lumped Displacement of a Membrane

An equivalent circuit model of a distributed system such as a CMUT membrane, requires a consistent use of circuit parameters. The selection of the lumped parameters used in the circuit should not effect the kinetic and potential energies of the membrane. Here we will investigate the effect of the lumped displacement measure on the kinetic and potential energies of a deflected CMUT membrane. The kinetic energy, E_k, of a CMUT membrane is calculated as follows:

$$\begin{aligned} E_k(t) &= \int_0^{2\pi}\int_0^{a} \frac{1}{2}\, v^2(r,t)\,\rho\, t_m r\, dr\, d\theta \; = \\ &= \frac{1}{2}\rho t_m \pi a^2 \left[\frac{1}{\pi a^2} \int_0^{2\pi}\int_0^{a} v(r,t)^2\, r\, dr\, d\theta \right] = \\ &= \frac{1}{2}\, m\, v_{rms}^2(t) \end{aligned} \tag{2.15}$$

Above result indicates that choosing the rms value as the lumped variable gives the correct kinetic energy of a membrane. On the other hand, the stored potential energy, E_p in a deflected membrane by a force, F caused by a uniform pressure, P, is calculated by evaluating the following line integral:

$$E_p = \int_0^{x(r)} \overrightarrow{F_{net}} \cdot d\overrightarrow{x} \tag{2.16}$$

The force, F_{net} and the displacement, x are in the same direction so we get rid of the vector notation and the dot product. Since the displacement of the membrane is not uniform, we should evaluate this line integral over the surface of the CMUT membrane.

$$\begin{aligned} E_p(t) = & \int_0^{x(r)} \int_0^{2\pi} \int_0^{a} x(r,t)\, Prdr\, d\theta\, dx \; = \\ & = P\pi a^2 \left[\frac{1}{\pi a^2} \int_0^{2\pi} \int_0^{a} x(r,t)\, r\, dr\, d\theta \right] = \\ & = F x_{avg}(t) = \left(F \frac{x_{avg}(t)}{x_{rms}(t)} \right) x_{rms}(t) \end{aligned} \tag{2.17}$$

where the expression in the brackets is equal to the average displacement, x_{avg}. If the average value is chosen as the lumped measure, Fx product will represent the potential energy correctly. However, when the rms displacement measure is chosen, the force on the membrane msut be divided by a factor, κ for the correct potential energy.

$$\kappa = \frac{x_{rms}}{x_{avg}} \tag{2.18}$$

The factor κ is first defined here but, was calculated in [57] as $3/\sqrt{5}$ for the uncollapsed state. In the collapsed state, on the other hand, κ depends on the deflection profile and decreases as the displacement of the membrane increases. The limit for the lumped deflection of a membrane will be the case where all sufrace of the membrane is contacted to the substrate. In this hypothetical case, the average and rms displacements will be equal and t_g. Hence κ can be represented as follows as a function of the rms displacement:

$$\kappa(x_{rms}) = \frac{x_{rms}}{x_{avg}} = \begin{cases} \frac{3}{\sqrt{5}} & \text{for } x_{rms} \leq \frac{t_g}{\sqrt{5}} \\ \frac{3}{\sqrt{5}} - \gamma_0 \left(x_{rms} - \frac{t_g}{\sqrt{5}} \right) & \text{for } x_{rms} > \frac{t_g}{\sqrt{5}} \end{cases} \tag{2.19}$$

where γ_0 is a fitting factor, since the variation of κ is approximately linear as seen in Fig. 2.4. A membrane under uniform pressure touches the substrate when $x_{avg} = t_g/3$ or $x_{rms}{=}t_g/\sqrt{5}$. The value of γ_0 in the collapsed state is calculated using MATLAB[1]. The variation of κ as a function of the rms displacement is plotted in Fig. 2.4.

---

[1] MathWorks Inc., Natick, MA, USA.

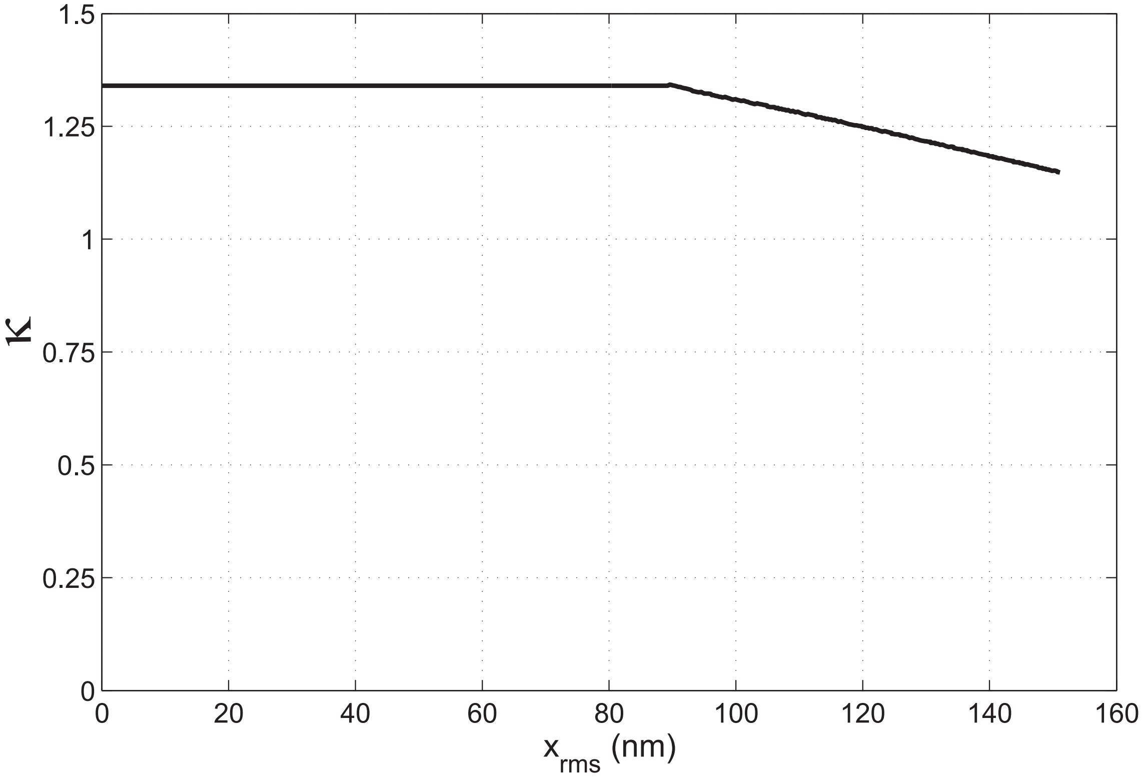

Figure 2.4: The correction factor, κ as a function of rms displacement for a CMUT membrane with dimensions: a=25 μm, t_m=1.5 μm, t_i=0.4 μm and t_g=0.2 μm. For this figure, γ_0 of equation (2.4) is 3.16.

2.4 Lumped Forces Acting on a Membrane

In order to understand the mechanics of a deflected membrane, we need to determine mechanical and electrical force functions with respect to the membrane displacement. At this point, we make the assumption that the deflection profile caused by the nonuniform attraction force of an applied voltage can be approximated by the deflection caused by a uniform pressure with the same total force. This is a good assumption when the membrane has an electrode covering its full surface. We will show the validity of the assumption even in the collapse mode when the attraction force is highly nonuniform. Since the force due to an applied pressure is balanced by the mechanical restoring force of the membrane, we can express the lumped restoring force F_r in terms of P as:

$$F_r = \frac{1}{\kappa} P \pi a^2 \tag{2.20}$$

Physical Quantity	rms	average
Displacement	x_{rms} (2.5)	x_{avg} (2.3)
Velocity	v_{rms}	v_{avg}
Mass	m	$\kappa^2 m$
Restoring Force	F_r (2.21)	κF_r
Electrical Force	F_e (2.26)	κF_e
Atmospheric Force	F_{atm} (2.27)	κF_{atm}
Kinetic Energy	$\frac{1}{2}\, m\, v_{rms}^2$	$\frac{1}{2}\, \kappa^2\, m\, v_{avg}^2$
Potential Energy	$\int \frac{1}{\kappa}\, F_{net}\, dx_{rms}$	$\int F_{net}\, dx_{avg}$

Table 2.1: The equivalence of physical properties of a CMUT membrane when average or rms lumped displacement is defined. The force expressions are given in corresponding equations in this chapter.

Note that the force, when defined as a function of x_{rms}, is divided by the correction factor κ. In this section, the expressions of the forces acting on a CMUT membrane, will be given as a function of x_{rms}. The equivalence of the physical quantities of a CMUT membrane are given in Table 2.1 for average and rms displacement measures.

For the uncollapsed state with a given applied pressure P, the deflection profile and hence x_{avg} and x_{rms} can be calculated using equations in (2.4) and (2.6), respectively. For the collapsed state, the deflection profile is calculated using (2.8). Average and rms displacement of the collapsed membrane, on the other hand, can be calculated using the equations in (2.3) and (2.5), respectively.

Because of the highly nonlinear nature of the restoring force in the collapsed region, a tenth order polynomial with coefficients β_0, β_1, β_2, … β_{10} is necessary for a good approximation. Hence, F_r can be expressed as:

$$F_r(x_{rms}) = \frac{1}{\kappa} \begin{cases} \frac{64\sqrt{5}\pi D}{a^2} x_{rms}, & x_{rms} \leq \frac{t_g}{\sqrt{5}} \\ \sum_{n=0}^{10} \beta_n x_{rms}^n, & x_{rms} > \frac{t_g}{\sqrt{5}} \end{cases} \tag{2.21}$$

F_r is plotted in Fig. 2.5 as a function of x_{rms}. It is a linear function in the uncollapsed region, while it becomes highly nonlinear in the collapsed region. The derivative of this curve with respect to x_{rms} is the nonlinear stiffness of the CMUT membrane.

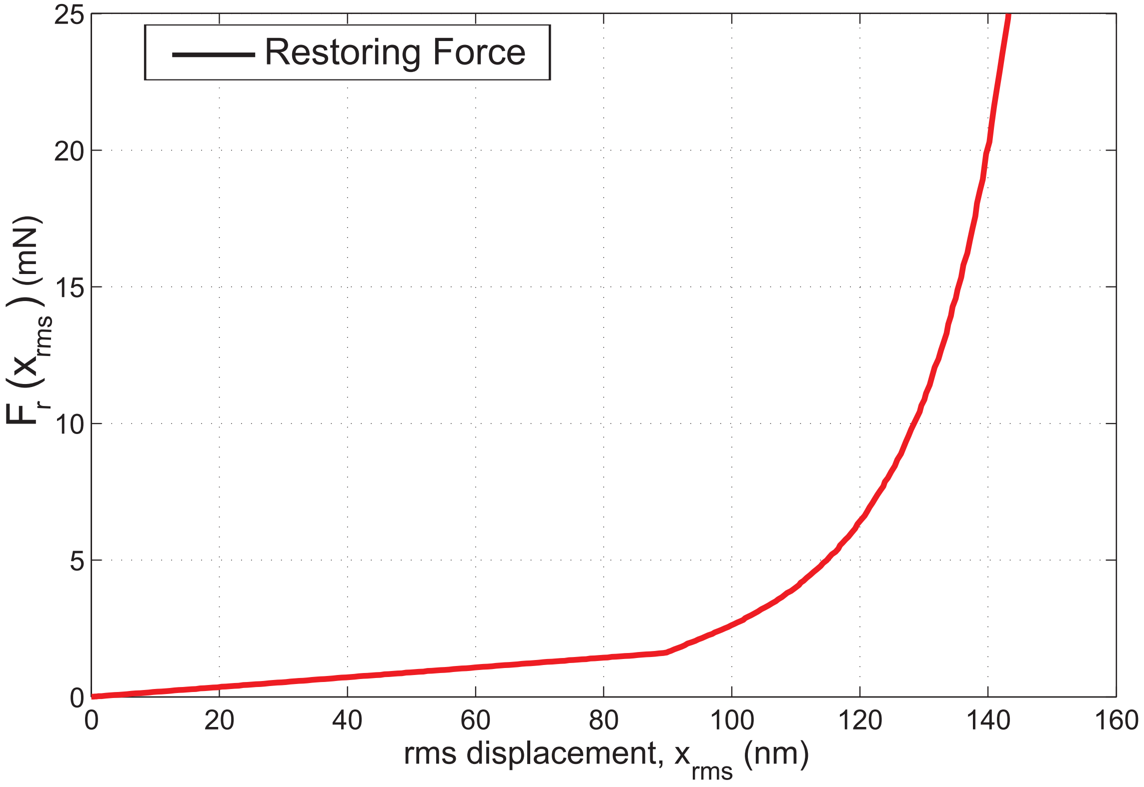

Figure 2.5: Mechanical restoring force (solid) as a function of x_{rms}. The dimensions of silicon nitride membrane: a=25 μm, t_m=1.5 μm, t_i=0.4 μm and t_g=0.2 μm.

The lumped electrical attraction force, F_e, generated by an applied voltage, V_{in}, is determined in terms of x_{rms} by using the expressions in [78] and [57] as follows:

$$F_e(V_{in}, x_{rms}) = \frac{1}{2\kappa}\frac{dC}{dx_{rms}}V_{in}^2 \tag{2.22}$$

where C is the capacitance between the two electrodes. The capacitance, C, between the electrodes of a CMUT is calculated as follows:

$$C = \int_0^{2\pi}\int_0^{a} \frac{\epsilon_0 r}{t'_g - x(r)}\, dr\, d\theta \tag{2.23}$$

where $t'_g = t_g + t_i/\epsilon_r$ with ϵ_r being the relative permittivity of the insulation material. For a deflected CMUT in the uncollapsed state, (2.23) is evaluated between 0 and a as a function of x_{rms} as follows:

$$C = \frac{\epsilon_0 \pi a^2 \operatorname{atanh}\left(\sqrt{\frac{\sqrt{5}x_{rms}}{t'_g}}\right)}{\sqrt{\sqrt{5}\, t'_g x_{rms}}} \tag{2.24}$$

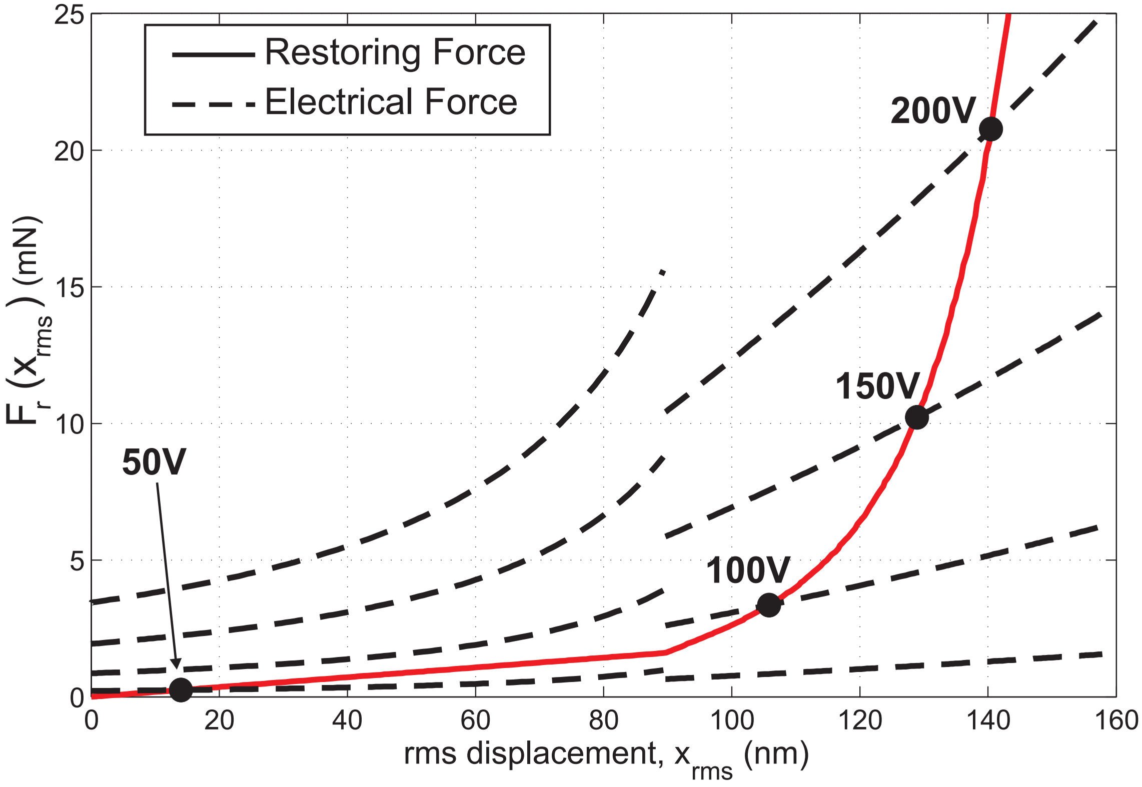

Figure 2.6: Mechanical restoring force (solid) and electrostatic attraction forces (dashed) when the bias is 50, 100, 150 and 200 Volts as a function of x_{rms}. The dimensions of silicon nitride membrane: a=25 μm, t_m=1.5 μm, t_i=0.4 μm and t_g=0.2 μm. The intersection point of the curves is the static equilibrium position, when the atmospheric pressure is neglected.

The derivative of the capacitance with respect to displacement is given in [78] as:

$$\frac{dC}{dx_{rms}} = \frac{\epsilon_0 \pi a^2}{2t'_g \frac{\sqrt{5}}{3} x_{rms} \left(1 - \frac{\sqrt{5} x_{rms}}{t'_g}\right)} - \frac{C}{\frac{2\sqrt{5}}{3} x_{rms}} \tag{2.25}$$

for the uncollapsed state. The capacitance of a collapsed membrane, on the other hand, can be determined numerically by dividing the profile into rings and using parallel plate approximation on each ring. The capacitance for the collapsed state is expressed by fitting a fourth order polynomial to the capacitance curve as a function of the displacement measure. The derivative is taken simply by taking the derivative of the polynomial approximation.

The electrostatic attraction force on a membrane is a function of the applied voltage as well as the position of the membrane. In the uncollapsed state, F_e is given

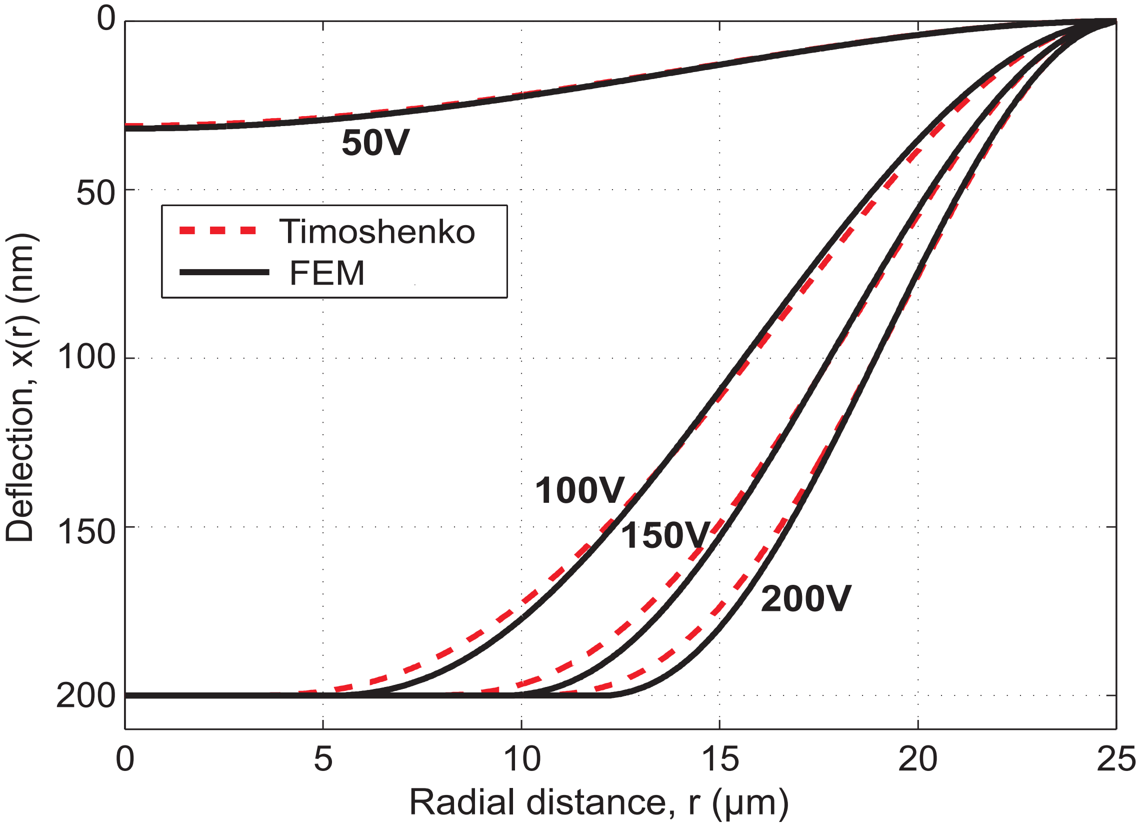

Figure 2.7: Displacement profiles calculated by electrostatic FEM simulations (solid) and by Timoshenko's plate deflection under uniform pressure (dashed) for a silicon nitride membrane with a=25 μm, t_m=1.5 μm, t_i=0.4 μm, t_g=0.2 μm for different values of bias. The atmospheric pressure is neglected.

in (2.22). In the collapsed region, we fit a third order polynomial to the nonlinear function and find corresponding coefficients α_0, α_1, α_2 and α_3 of the polynomial. Hence we express F_e as:

$$F_e(V_{in}, x_{rms}) = \frac{1}{2\kappa} V_{in}^2 \begin{cases} \text{Eq. 2.25}, & x_{rms} \le \frac{t_g}{\sqrt{5}} \\ \sum_{n=0}^{3} \alpha_n x_{rms}^n, & x_{rms} \ge \frac{t_g}{\sqrt{5}} \end{cases} \tag{2.26}$$

The electrostatic attraction force, F_e is not only nonlinear but also discontinuous at the point where the membrane touches the substrate, since there is a sudden change in the derivative of the capacitance at that point. The calculated $F_e(x_{rms})$ for different voltages are plotted in Fig. 2.6 as a function of rms displacement along with the restoring force curve which was also depicted in Fig. 2.5.

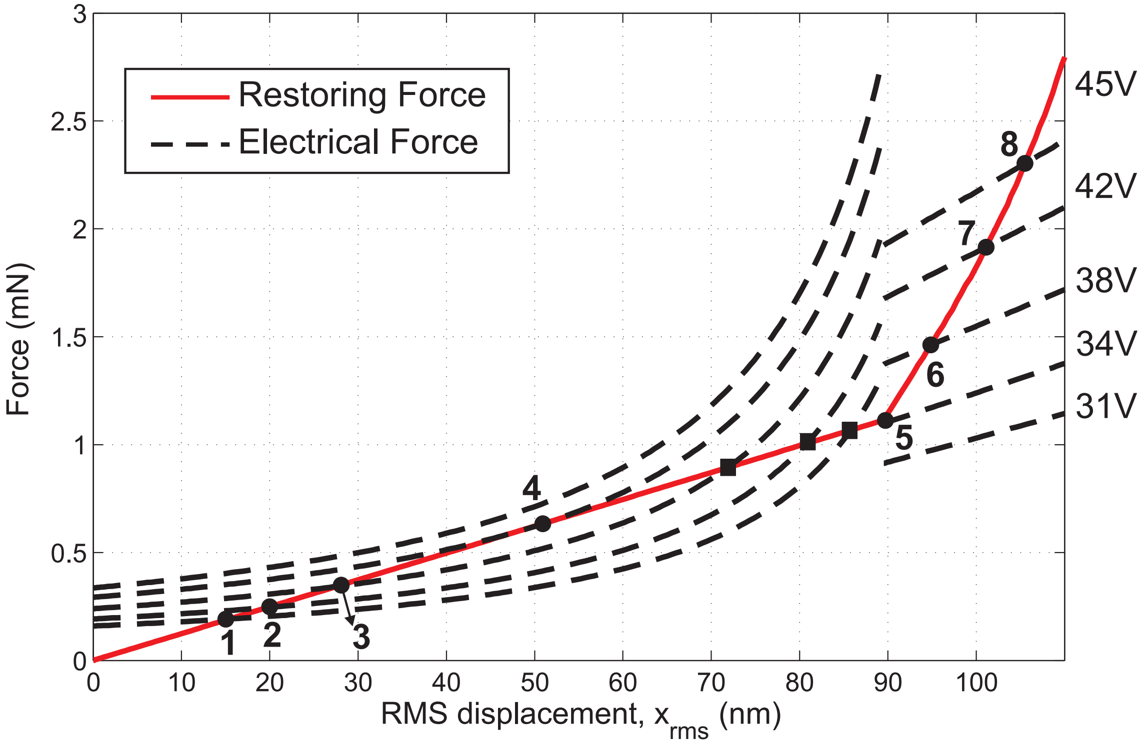

Figure 2.8: The electrostatic attraction and mechanical restoring forces of a silicon nitride membrane with a=30 μm, t_m=1.5 μm, t_i=0.2 μm, t_g=0.2 μm for different values of DC bias as a function of x_{rms}. The atmospheric pressure is neglected.

Although a closed form expression of deflection as a function of applied voltage cannot be determined, a numerical solution is possible by determining the intersection of the nonlinear electrostatic attraction and mechanical restoring force curves. The intersection points in Fig. 2.6 give the static equilibrium displacement points. Therefore the deflection profile caused by the applied voltage is approximated by a deflection caused by a uniform pressure. In Fig. 2.7, the profiles calculated by the proposed method are compared to the profiles obtained by electrostatic FEM simulations for the same bias values of Fig. 2.6. The good agreement justifies the assumption we made above.

We depicted the restoring and attraction forces around the collapse point in more detail in Fig. 2.8 for a CMUT with different dimensions. As seen in this figure, for voltages less than collapse voltage, the electrical force curve intersects with the linear portion of the restoring force curve. As the applied voltage is increased from 31 to 45 V, the static displacement follows the intersection points, 1, 2, 3, 4 and

8. We note that at 42 V, the electrical and restoring force curves are tangential to each other. Increasing the voltage further will result in a new intersection point in the nonlinear region of the restoring force curve in the collapsed region. At 45 V, for example, the new static equilibrium point is the point 8. Therefore, as the voltage is increased from 31 to 45 V, the static displacement follows the points 1, 2, 3, 4 and 8. The intersection points signified by squares are the unstable solutions of the membrane displacement. On the other hand, if we reduce the voltage starting from 45 towards 31 V, the static equilibrium displacement will follow the intersections in the nonlinear collapsed region of the restoring force curve, i.e., the points, 8, 7, 6 and 5. For voltages less than 34 V, the electrostatic force curve does not intersect with the nonlinear region of the restoring force curve. At 31 V, the static equilibrium displacement is the point 1. Therefore, as the voltage is decreased from 45 to 31 V, the static displacement follows the points 8, 7, 6, 5 and 1, demonstrating the well known hysteretic behavior of CMUTs.

While our model predicts the collapse and snap-back voltages as 42 and 33 V, FEM simulations calculates the same voltages as 42 and 29 V, respectively. The difference in the value of the snap-back voltage is attributed to the variation in the membrane profile around the snap-back point, because we always use the profiles generated by a uniformly distributed load. The smallest rms displacement of a collapsed membrane is achieved when the membrane barely touches the substrate. At this state the rms displacement is equal to ~ 89.5 nm for this example. As seen in Fig. 2.9, FEM can handle smaller displacements just before snap-back, which indicates different profiles from that is generated by a uniformly distributed load are calculated by FEM.

In Fig. 2.9, x_{rms} as a function of applied voltage is shown in comparison to FEM simulation results. The error between the rms deflections and the electrostatic FEM simulation results is within 1% of each other except for voltages in the close vicinity of the snap-back. While previously developed models in the literature are valid for voltages less than the collapse voltage only, our method can predict the deflections before and after the collapse of the membrane. In addition, the model is capable of predicting the hysteretic behavior of snap back as well.

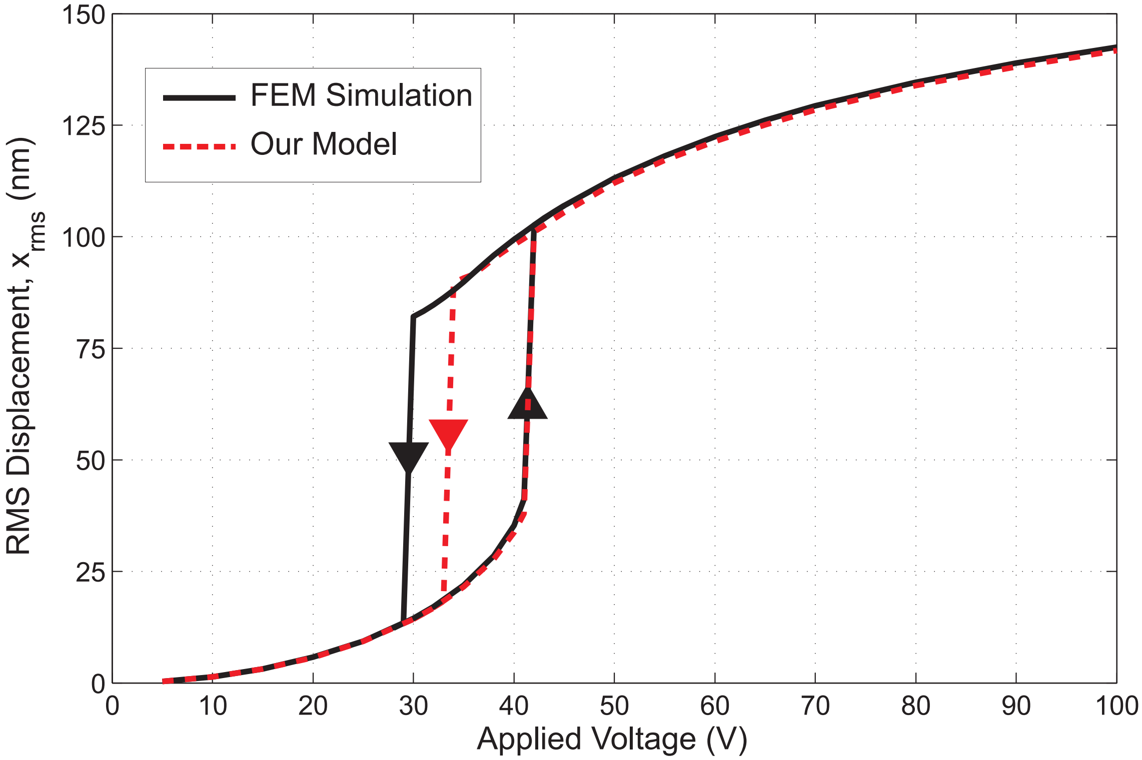

Figure 2.9: RMS displacement of a silicon nitride membrane with a=30 μm, t_m=1.5 μm, t_i=0.2 μm, t_g=0.2 μm as a function of applied voltage. The displacements calculated by our method (dashed) are compared to FEM simulation results (solid). The effect of the atmospheric pressure is neglected.

In the previous analysis, whose results are depicted in Fig. 2.6 — 2.9, atmospheric pressure on the membrane was neglected. In order to include the effect of the atmospheric pressure, a constant force should be added to the electrostatic force. Both the electrostatic force and the atmospheric pressure act against the restoring force of the membrane. The force generated by the atmospheric pressure, F_{atm} is:

$$F_{atm}(x_{rms}) = \frac{1}{\kappa} P_0 \pi a^2 \tag{2.27}$$

where P_0 is the atmospheric pressure.

The displacement of an uncollapsed or collapsed CMUT membrane under uniform pressure excitation, and coefficients of the polynomials in (2.19), (2.21) and (2.26) were calculated by parametric MATLAB codes.

Chapter 3

Nonlinear Equivalent Circuit Model

Using the force and deflection expressions acquired in Chapter 2, we will develop an equivalent circuit models for transmit mode of operation of CMUTs. The circuit model will handle the nonlinear operation of a CMUT in the collapsed state while successfully modeling the CMUT in uncollapsed state.

3.1 Through Variable: Velocity

Most of the equivalent circuit modelling efforts since Mason, used average velocity of the membrane (v_{avg}) as the through variable in the circuit. The choice of average velocity as the through variable is problematic with some higher mode CMUT velocity profiles, because it may give zero lumped velocity resulting in an infinite radiation impedance. In addition, the kinetic energy expression given in (2.15) shows that when average velocity is chosen to be the through variable, the mass of the vibrating plate should be increased by a factor of κ^2. An increased mass, in order to calculate the kinetic energy correctly is not physical. Choosing rms velocity as the through variable, on the other hand, predicts the kinetic energy correctly when the exact mass of the vibrating structure is used. Such approach provides a more physical understanding to the equivalent mass-spring model. Use of rms velocity, however, requires the forces to be scaled by $1/\kappa$ as shown in (2.17) in order to

Mechanical (rms)	Mechanical (avg)	Equiv. circ.
v_{rms}	$v_{avg} = \frac{1}{\kappa} v_{rms}$	i_v
x_{rms}	$x_{avg} = \frac{1}{\kappa} x_{rms}$	q_x
$F_{atm}(x_{rms})$	κF_{atm}	$V_{atm}(q_x)$
$F_e(V_{in}, x_{rms})$	$\kappa F_e(V_{in}, x_{avg})$	$V_e(V_{in}, q_x)$
$F_r(x_{rms})$	$\kappa F_r(x_{avg})$	$V_r(q_x)$
m	$\kappa^2 m$	L_m
Z_r	$\kappa^2 Z_r$	Z_r
$\frac{1}{2}\, m\, v_{rms}^2$	$\frac{1}{2}\, \kappa^2\, m\, v_{avg}^2$	$\frac{1}{2}\, L_m\, i_v^2$
$\int (F_{atm}+F_e\text{-}F_r)\, dx_{rms}$	$\int \kappa (F_{atm}+F_e\text{-}F_r)\, dx_{avg}$	$\int (V_{atm}+V_e\text{-}V_r)\, dq_x$

Table 3.1: Equivalence between mechanical and electrical quantities.

calculate the potential energy stored in the membrane correctly.

The circuit simulations in this thesis were performed by using the rms velocity as the through variable. Therefore, in the previous chapter, forces were defined including the division by κ. For completeness, circuit parameters for both convention will be calculated in this chapter and are given in Table 3.1. The rms displacement was defined in (2.5), where the integration limits were chosen from 0 to a even if the membrane is collapsed with a contact radius of b. Therefore during the calculation of the circuit parameters the same integration limits will be employed.

3.2 Modelling Transmitting CMUT

In the equivalent circuit, v_{rms} will be represented by the current, i_v, and x_{rms} will be represented by the charge, q_x. The forces acting on the membrane are functions of the displacement, as discussed in the previous chapter. In order to calculate the rms displacement or charge q_x, the current passing through the circuit, should be integrated over time. A current controlled current source connected in parallel with a capacitor integrates the current on the capacitor. The voltage on the capacitor gives the rms displacement of the membrane when the current of the controlled current source is equal to the current passing through the equivalent circuit and the value of the capacitor is 1 Farad.

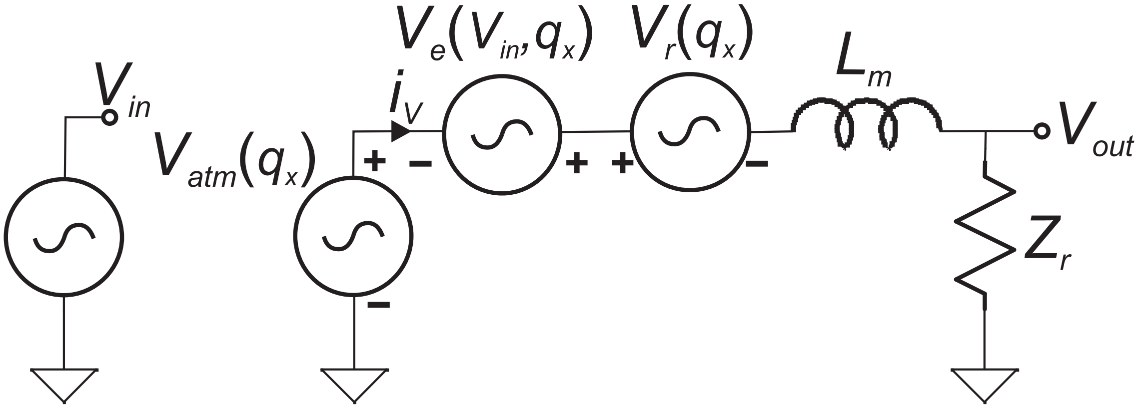

Figure 3.1: Equivalent circuit model for simulating the transmitting behavior of CMUTs under any excitation. $V_r(q_x)$ stands for the series mechanical capacitance in Mason's equivalent circuit model. $V_e(V_{in}, q_x)$ represents the force generated at the mechanical side of the Mason's model. The shunt input capacitance of Mason's model is ignored, since we assume that CMUTs are driven by a voltage source. The controlling variable, q_x is calculated by integrating the state variable, i_v on a 1F capacitor, which is not depicted in this figure.

3.2.1 Static Deflection

The forces acting on a CMUT membrane, mechanical restoring, electrostatic attraction and atmospheric forces are modelled in the electrical equivalent circuit as controlled voltage sources connected in series as illustrated in Fig. 3.1.

The electrical excitation is represented by a time-varying voltage source, $V_{in}(t)$. The electrical force acting on the membrane is a function of the input voltage and membrane position. Therefore, $F_e(V_{in}, x_{rms})$ is modelled by a voltage and charge controlled nonlinear voltage source, $V_e(V_{in}, q_x)$. Using the definition of the electrical force in (2.26), we define the controlled voltage source by replacing rms through variables with charge, q_x.

The forces, $F_r(x_{rms})$ and F_{atm} are represented by charge controlled nonlinear voltage sources, $V_r(q_x)$ and $V_{atm}(q_x)$, respectively. Similar to V_e, the displacement measure, x_{avg} or x_{rms} is replaced by charge, q_x.

The controlled sources representing atmospheric and electrostatic attraction forces should reinforce each other. Restoring force, on the other hand, should be connected with a reversed polarity acting against the previous two.

Our model replaces the linear circuit components of Mason's equivalent circuit in order to handle the collapsed state of the CMUT membrane. The mechanical capacitance in the Mason's model is inherently represented by the charge controlled nonlinear voltage source, $V_{res}(q_x)$. The use of the electro-mechanical transformer of Mason's model is performed by the charge and voltage controlled nonlinear voltage source, $V_{el}(V_{in}, q_x)$. The remaining components, L_m and Z_r, are identical to that of Mason's model and will be discussed next.

3.2.2 Membrane mass

Similar to the Mason's equivalent circuit model, we will represent the mass, m of the membrane by a series inductor, L_m. When the rms through variable is used, the value of the inductor is equal to the mass of the membrane, since the kinetic energy of a membrane is modelled correctly by the rms velocity convention.

$$L_m = m = \rho\, t_m \pi a^2 \quad \text{For rms convention.} \tag{3.1}$$

where ρ is the density of the membrane material.

When the average velocity is chosen as the through variable in the circuit, the value of the inductor is the mass multiplied by κ^2 in order to model the kinetic energy of the membrane correctly:

$$L_m = \kappa^2 m = \kappa^2 \rho\, t_m \pi a^2 \quad \text{For average convention.} \tag{3.2}$$

3.2.3 Radiation resistance

The loading of the immersion medium will be modelled with the radiation impedance, Z_r, whose value is equal to the lumped across variable, force at the surface of the membrane divided by the through variable, v_{rms}. Z_r of a circular CMUT membrane for the uncollapsed mode was calculated earlier [67]. It was shown that when $a > \lambda$, the imaginary part of the radiation impedance vanishes and the real part of the impedance approaches to $\pi a^2 \rho_0 c_0$ where λ is the wavelength in the immersion medium, ρ_0 and c_0 are the density and the speed of sound in that medium, respectively. This is a good approximation for membranes that are at the center of a large array.

We do not have the Z_r expression for the collapse mode CMUTs. In this thesis, we assume that the radiation impedance of a collapsed membrane with radius, a and contact radius, b (as in Fig. 2.2) can be approximated by the radiation impedance of a piston ring transducer with outer radius, a and inner radius, b. The radiation impedance of such a ring transducer was computed by Stepanishen [82]. It was shown that the radiation impedance of such a transducer approaches to $\rho_0 c_0$ product times the area of the ring for large ka values.

$$Z_r\{b, a\} = \pi(a^2 - b^2)\rho_0 c_0 \qquad \text{for} \quad a > \lambda. \tag{3.3}$$

In (3.3), the notation $\{b, a\}$ denotes the boundary where the computation of the radiation impedance is conducted. In this thesis, however, we defined the circuit parameters over the entire circular membrane, not only the vibrating ring segment between radii b and a. Hence, the circuit variables, lumped force, F and lumped velocity, v_{rms} must be identically defined for every component of the equivalent circuit model.

The radiation impedance of a piston ring transducer with outer radius, a and inner radius, b was calculated as follows [82]:

$$Z_{ring}\{b, a\} = \frac{F\{b, a\}}{v_{rms}\{b, a\}} \tag{3.4}$$

Since the deflections are defined as a result of a uniform force throughout the membrane surface, lumped force, F between b and a and 0 to a are equal:

$$F\{b, a\} = F\{0, a\} \tag{3.5}$$

The through variable of the equivalent circuit, rms velocity, is calculated as follows:

$$v_{rms}\{0, a\} = \omega \sqrt{\frac{1}{\pi a^2} \int_0^{2\pi} \int_0^{a} r\, x^2(r)\, dr\, d\theta}$$

since $x(r) = 0$ for $0 < r < b$,

$$\begin{aligned}
v_{rms}^2\{0,a\} &= \frac{1}{\pi a^2} \int_b^a 2\pi\omega r x^2(r) dr \\
&= \frac{\pi(a^2-b^2)}{\pi(a^2-b^2)} \frac{1}{\pi a^2} \int_b^a 2\pi\omega r x^2(r) dr \\
v_{rms}^2\{0,a\} &= \frac{\pi(a^2-b^2)}{\pi a^2} v_{rms}^2\{b,a\} \qquad (3.6)
\end{aligned}$$

where $v_{rms}\{b,a\}$ is the through variable in (3.4). Evaluating (3.3), (3.5) and (3.6) in (3.4), the radiation impedance of a piston ring transducer in terms of the equivalent circuit variables is,

$$\begin{aligned}
Z_{ring}\{0,a\} &= Z_{ring}\{b,a\} \frac{a^2}{(a^2-b^2)} \\
Z_{ring}\{0,a\} &= \rho_0 c_0 \pi a^2 \qquad \text{for } a > \lambda \qquad (3.7)
\end{aligned}$$

Therefore the radiation impedance of a CMUT membrane for large ka is real and equal to $\rho_0 c_0 \pi a^2$ for both uncollapsed and collapsed cases when the through variable is rms velocity and defined from 0 to a:

$$Z_r = \rho_0 c_0 \pi a^2 \qquad \text{for } a > \lambda \qquad (3.8)$$

The radiation impedance expression in (3.8) is valid when the membranes are fully loaded by the medium. This condition is true for the membranes at the center of a large array. The condition is also true for a membrane in a rigid baffle as in the case of FEM simulations, which model the coupling medium by a fluid column with rigid boundaries. This is a suitable model for a membrane at the center of an infinite CMUT array, when there is no lateral displacement of the fluid.

The condition of validity above is not easily satisfied for typical CMUT cells. For a fabricated CMUT array the membrane dimensions are much smaller than the wavelength and not all the membranes are at the center part of the array. Therefore, the equivalent radiation impedance is somewhat lower. The radiation impedance for such an array of CMUT membranes was calculated by Senlik et.al. [67] for the uncollapsed state. It was shown that for an array of cells with a total array radius,

A, between $\lambda/3$ and λ, the equivalent radiation impedance for the whole array is approximately half of the value given in (3.8):

$$Z_r = \frac{1}{2}\pi a^2 \rho_0 c \qquad \text{for } \lambda/3 < A < \lambda \tag{3.9}$$

When the average velocity is used as the through variable in the equivalent circuit, the radiation impedance calculated above must be multiplied by κ^2, similar to the inductor representing the mass of the membrane.

3.2.4 Results

We tested the results of our equivalent circuit model by comparing them to FEM simulations and experimental results. A description of the utilized FEM model can be found in Appendix A. The material parameters used in the FEM and circuit model were chosen to be identical to the material parameters of the silicon nitride film we will use during the fabrication. These parameters are given in Table A.1 of Chapter 4. The equivalent circuit was simulated using LTSpice[1] circuit simulator. LTSpice is a public domain software and can be downloaded from http://www.linear.com/designtools/software.

The effect of any electrical excitation between the CMUT electrodes, can be simulated by defining the excitation at the controlling voltage source, V_{in} of the circuit in Fig. 3.1. The acoustical force output of the CMUT is the voltage across the radiation resistance, V_{out}. The average acoustical pressure at the surface of a CMUT, P_{out} can be calculated by converting the rms force output to average force by using the correction factor, κ in (2.19) and dividing the force by the membrane area:

$$P_{out} = \kappa \frac{V_{out}}{\pi a^2} \tag{3.10}$$

---

[1] Linear Technology Inc., CA, USA.

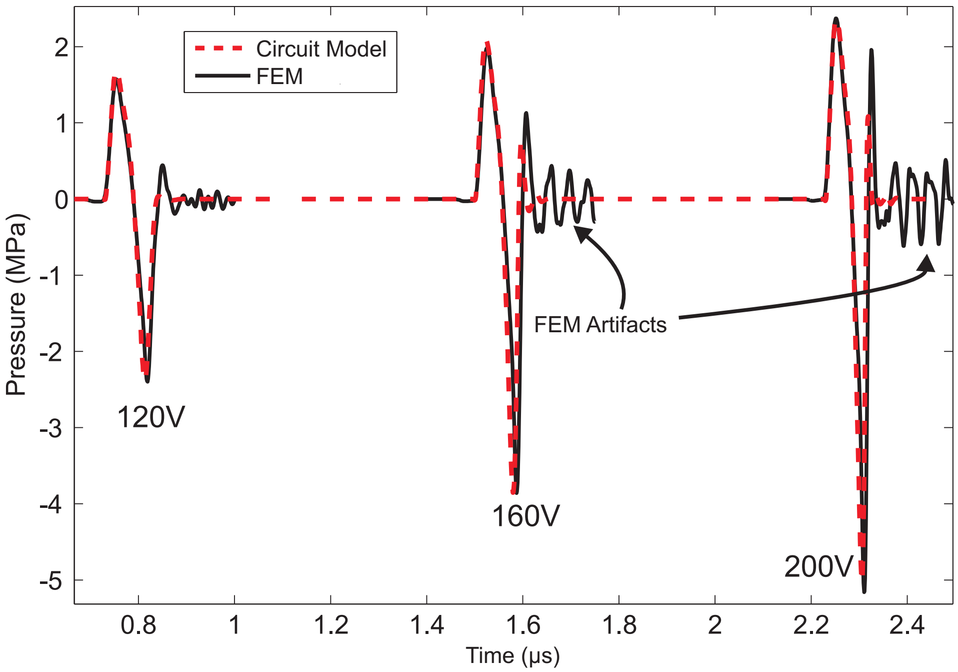

Figure 3.2: Comparison of the calculated average pressure output using FEM (solid) and equivalent circuit (dashed) simulation results, when CMUTs are excited by 120, 160 and 200 V negative pulse on equal amplitude bias. The rise and fall times of the pulses are 20 ns and the pulse width is 40 ns. The simulated CMUT has a silicon nitride membrane with a=30 μm, t_m=1.4 μm, t_i=0.4 μm, t_g=0.2 μm resulting in a collapse voltage of ~35V.

3.2.5 Comparison of the Equivalent Circuit Model to FEM

For a demonstration of the large signal capability of the circuit model, we applied electrical pulses to a CMUT with amplitudes much greater than its collapse voltage. The resulting pressure amplitudes calculated by the equivalent circuit simulations are plotted in Fig. 3.2 along with the FEM simulation results. In the equivalent circuit, we used the radiation impedance expression given in (3.8), since in the FEM simulations we modelled the coupling medium by a fluid column with rigid boundaries.

The peak-to-peak amplitudes of the transmitted pressure waves were predicted within 3% and the pulse width of the prominent cycle was estimated within 5%

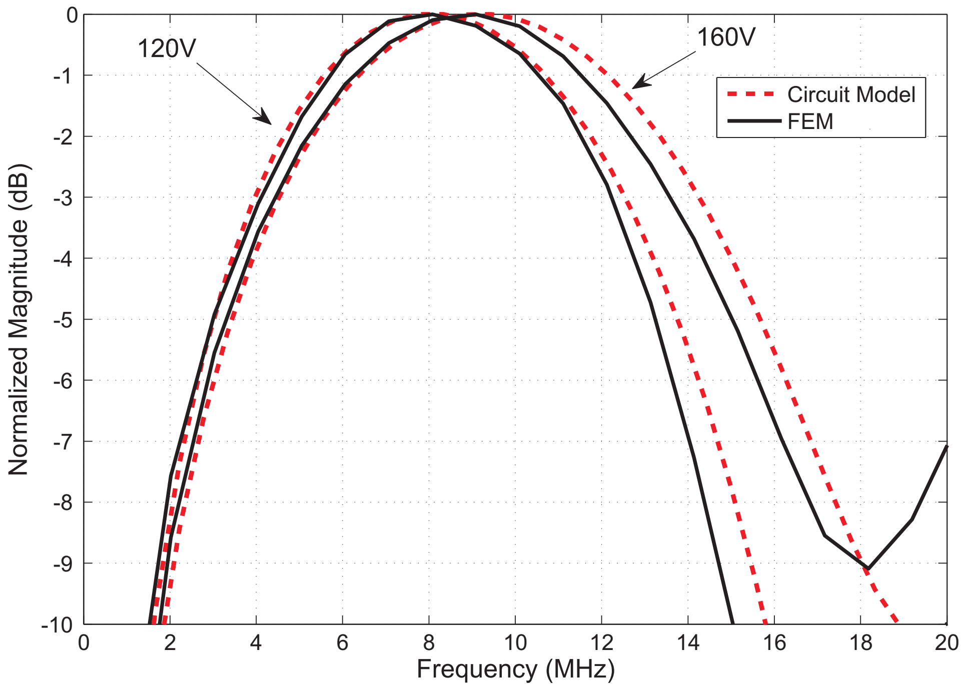

Figure 3.3: Normalized spectra of the calculated acoustic pulses in Fig. 3.2.

accuracy in the worst case. During the pulse cycle, the membrane was first released and then collapsed back to its initial position. Since the membrane has a non-zero kinetic energy at the time it reaches its initial position, it oscillates at a high frequency for a while before it stabilizes. This behavior was predicted by the equivalent circuit model. The low frequency oscillation seen in the FEM results, however, is a spurious oscillation as a result of rigidly defined stand regions and the lossless nature of the simulation.

The normalized transmission spectra of the CMUT, for two different excitations are shown in Fig. 3.3. The frequency spectra of the pressure waveforms calculated by the circuit model (dashed) and the FEM (solid) are in good agreement especially at the low frequency end. The deviation at the higher end is less than 6% in frequency.

Developed equivalent circuit model gives information about the membrane movement as well. We can extract information such as the contact radius, b, of a collapsed

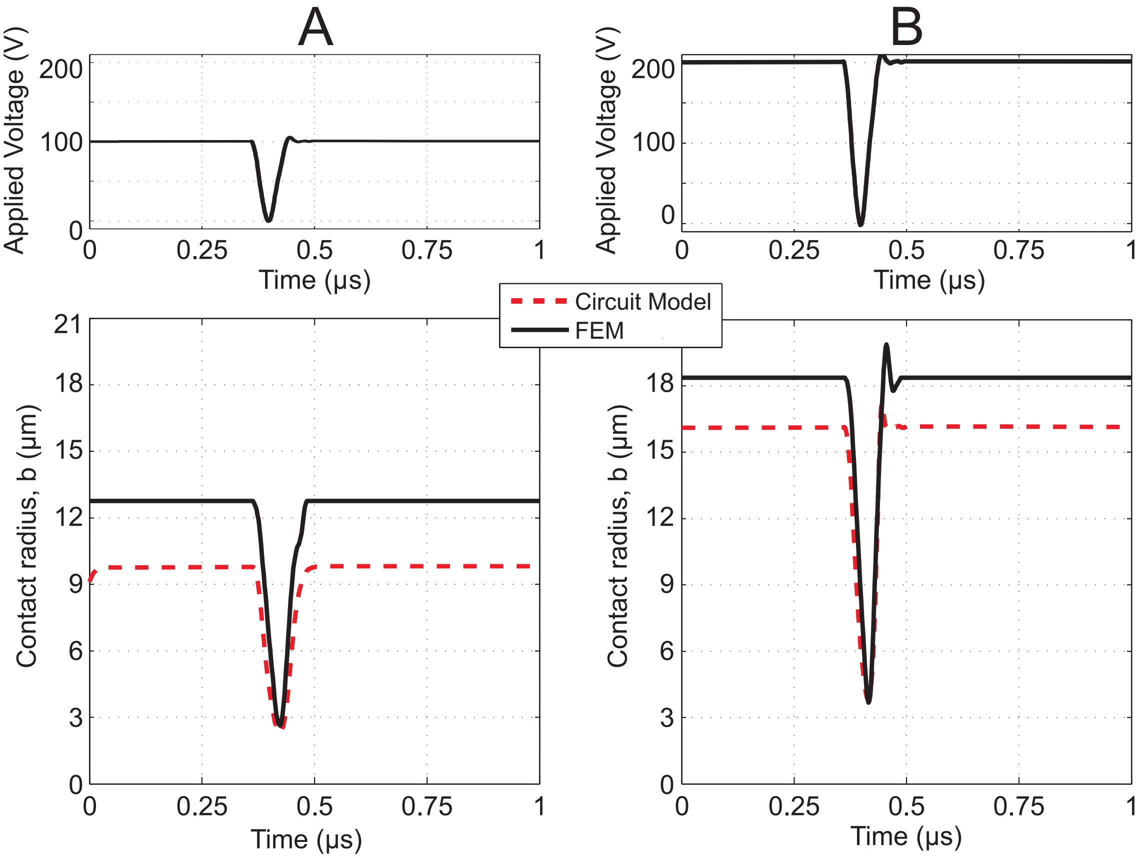

Figure 3.4: Variation of the contact radius, b, as calculated by FEM (solid) and equivalent circuit simulation (dashed) as a function of time, when a CMUT is excited by negative 100 V (A) and 200 V (B) pulses on a bias with equal amplitude. The applied signals are depicted at the top. The simulated CMUT has a silicon nitride membrane with a=30 μm, t_m=1.4 μm, t_i=0.4 μm, t_g=0.2 μm.

membrane during a pulse cycle. The variation of b as a function of time is plotted in Fig. 3.4, when the membrane was excited with large electrical signals. As seen in the figure, the membrane does not lose contact with the substrate during the short pulse cycles, even though the input voltage was decreased to 0 V. Even so, more than 7 MPa peak-to-peak radiated pressure at the surface of the CMUT is possible using a 200 V pulse. If the duration of the pulse is increased, eventually the membrane is released from the contact. The variation of the contact radius for pulses with different widths are depicted in Fig. 3.5.

In Fig. 3.5, variation of the contact radius during different pulse cycles are depicted when the electrical pulses are applied to the CMUTs with same membrane

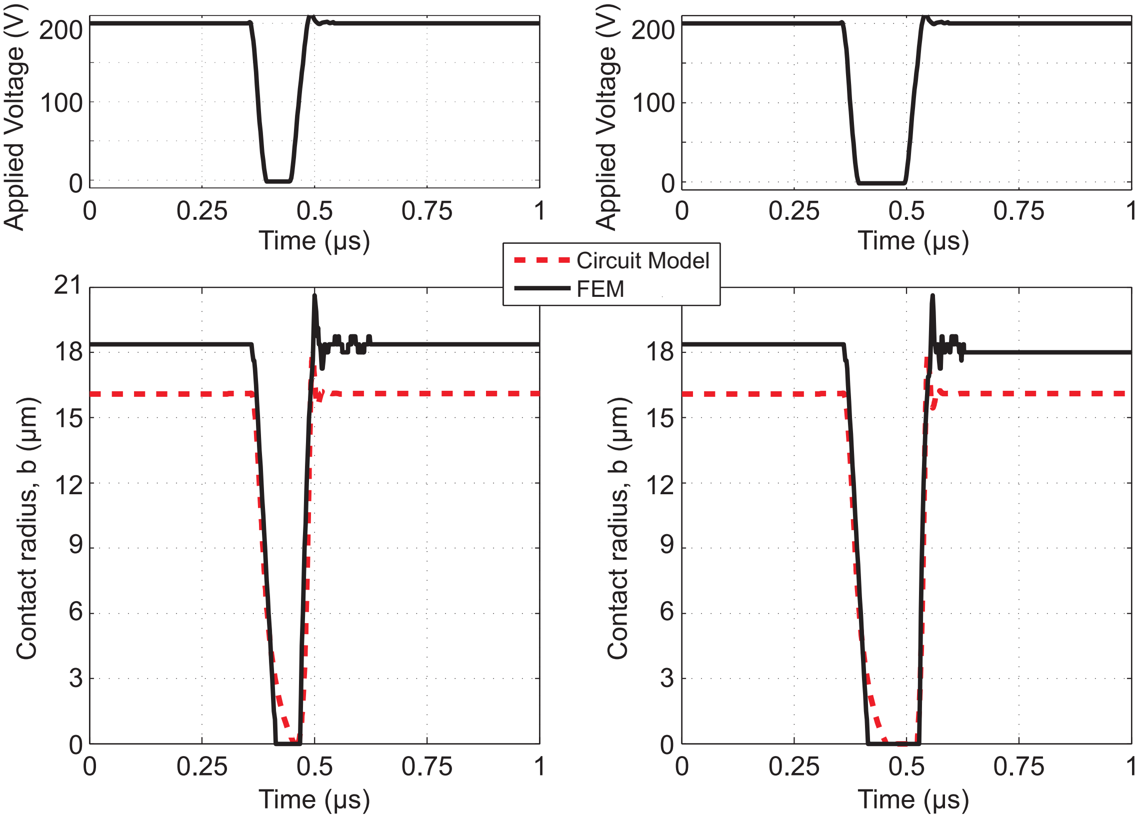

Figure 3.5: Variation of the contact radius, b, as calculated by FEM (solid) and equivalent circuit simulation (dashed) as a function of time, when a CMUT is excited by 200 Volts pulses with different widths on a bias with equal amplitude. The applied signals are depicted at the top. The simulated CMUT has a silicon nitride membrane with a=30 μm, t_m=1.4 μm, t_i=0.4 μm, t_g=0.2 μm.

dimensions used in Fig. 3.4. The difference seen in the contact radii calculated by FEM and circuit model can be attributed to the approximation of voltage generated deflection profiles by uniform pressure generated profiles. The circuit model is a lumped parameter simulator, whereas contact radius, b is a distributed parameter dependent heavily on the deflection profile of a collapsed membrane. Nevertheless, the results of the simulation tool are useful, for understanding CMUT behavior.

As a further demonstration of the electrical model we calculated the instantaneous displacement of a membrane collapsed due to the atmospheric pressure. Pulses of different amplitudes were applied to the CMUT. A rising voltage step collapses the membrane further to the substrate increasing x_{rms}. The falling voltage step

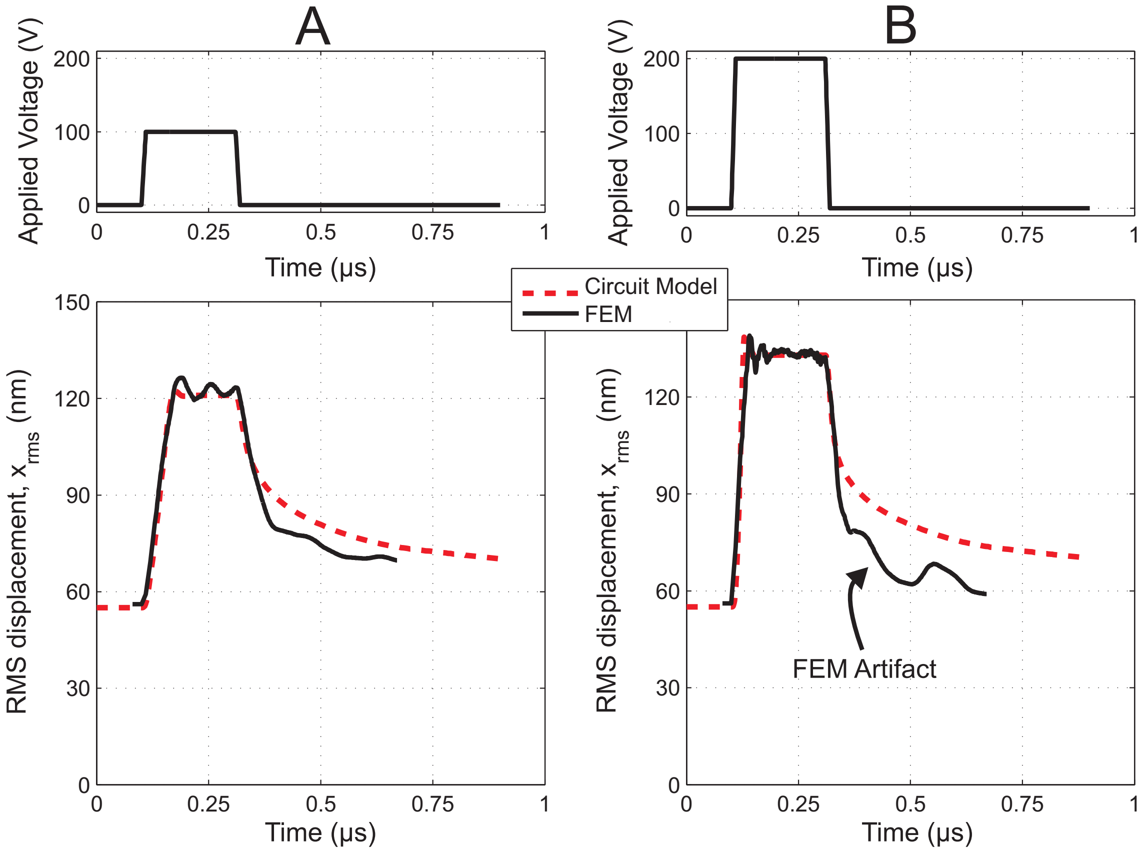

Figure 3.6: Variation of x_{rms} as calculated by FEM (solid) and equivalent circuit simulation (dashed) as a function of time, when the CMUT is excited by 10 ns rise or fall time pulses with 100 V (A) and 200 V (B) amplitudes. The simulated CMUT has a silicon nitride membrane with a=30 μm, t_m=2 μm, t_i=0.4 μm, t_g=0.16 μm resulting in a collapsed state under atmospheric pressure.

releases the membrane to its initial position. The variation of the membrane displacement was calculated by FEM simulations under the same electrical excitations and the results are depicted together in Fig. 3.6 for comparison.

In Fig. 3.7 we plotted the generated pressure under a fixed voltage step as a function of gap height. For gap heights larger than 420 nm, the membrane does not go into the collapsed state and a pressure of 0.25 MPa is obtained. On the other hand, for a gap height of about 60 nm, a collapsing membrane generates a pressure output of 4 MPa. Note that with such a small gap height CMUTs have a collapse voltage less than 10 Volts.

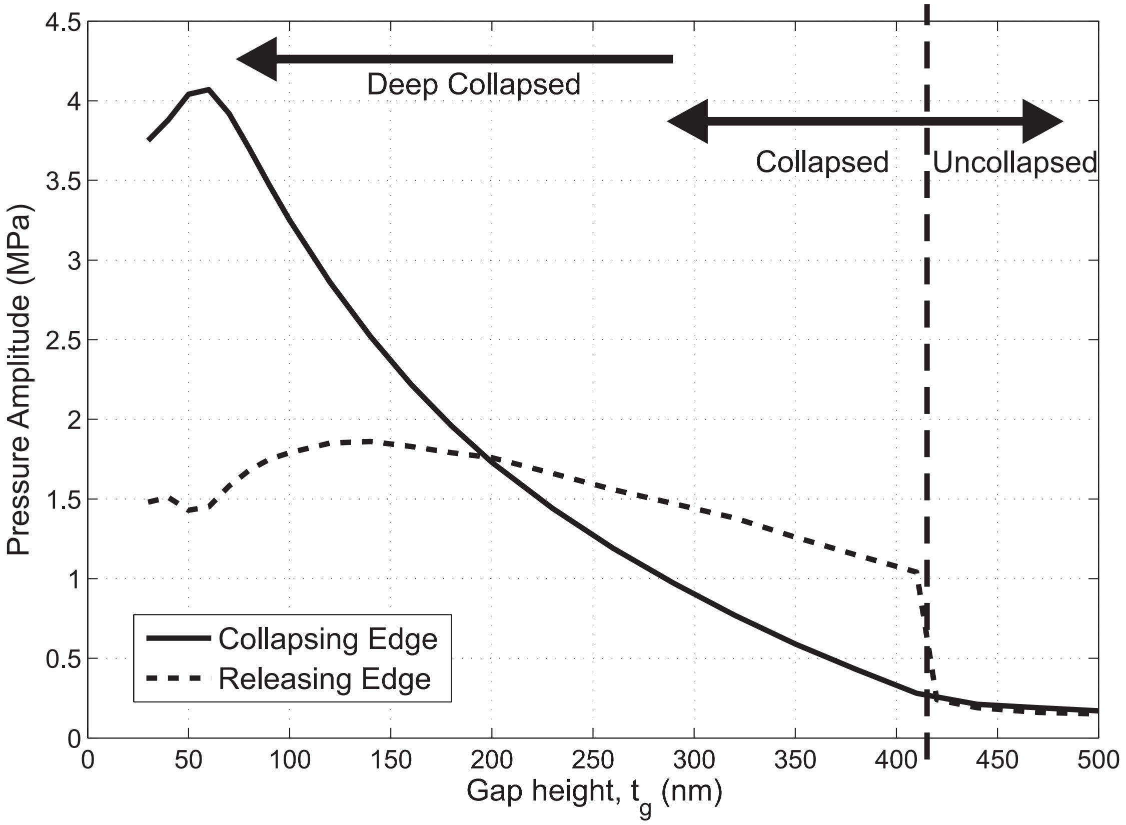

Figure 3.7: Peak pressure output of a CMUT array with a step excitation as a function of the gap height as found from the electrical equivalent circuit. The input step has an amplitude of 100 V and 10 ns rise and fall times. Considered membranes has a=30μm, t_m=1.4μm and t_i=0.4μm with varying t_g.

3.2.6 Comparison of the Model to Experiment

We compared the results of the equivalent circuit simulations to experimental results obtained from fabricated devices. Tested array has 11 by 11 cells with 5 μm spacing with a grid distribution resulting with a 67% fill factor. The aperture size is 0.71 mm by 0.71 mm. The fabrication process of the array is discussed in Chapter 4. During the curcuit simulations, we used the radiation resistance expression in (3.9), since $a \ll \lambda$ and $A \approx \lambda$ at 5 MHz. Although, the positive cycles of the output pressure waves are well predicted by the equivalent circuit simulations, the negative cycles are not. The difference may be attributed to frequency independent radiation resistance assumption.

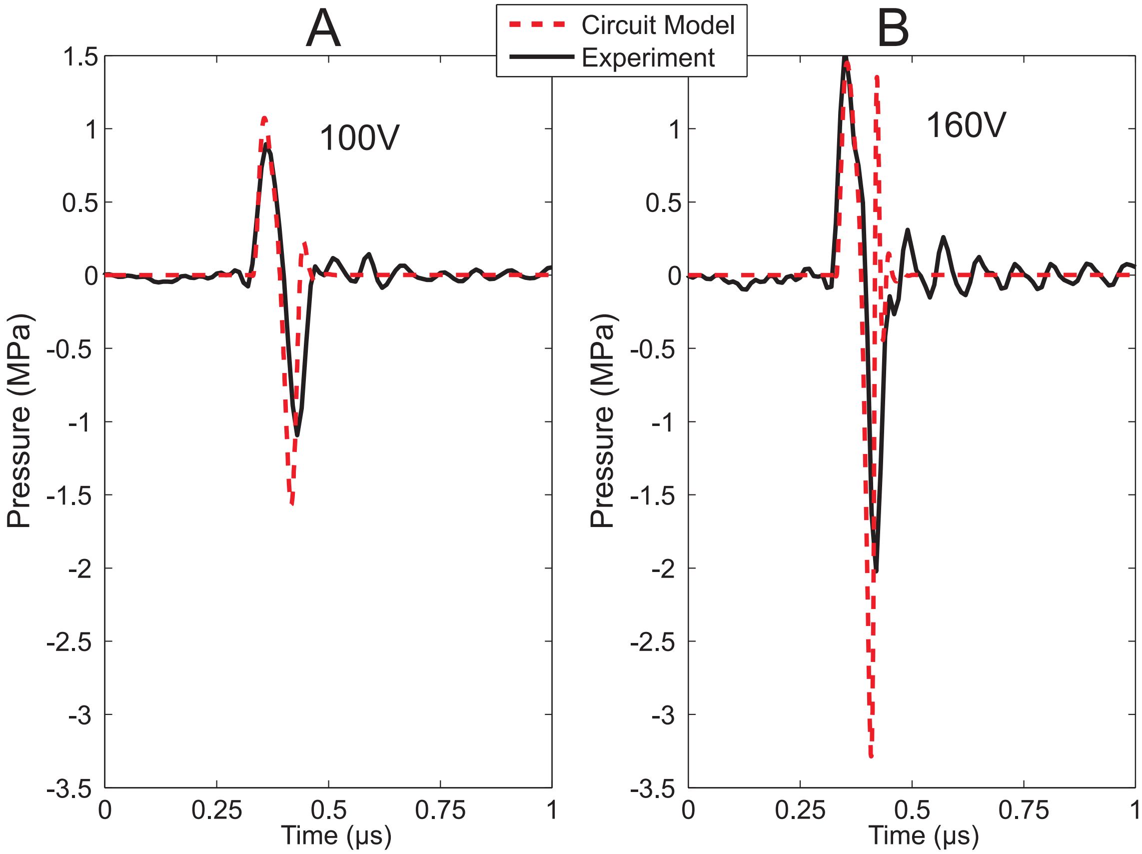

Figure 3.8: Comparison of the equivalent circuit simulations (dashed) to experimental results (solid). The CMUTs used in the experiments have a=30 μm, t_m=1.4 μm, t_g=0.2 μm and t_i=0.4 μm. They are excited with signals of 120 and 160V negative amplitudes on equal amplitude DC biases.

In order to achieve a higher accuracy for predicting the response of a complete array, a more accurate radiation impedance model is needed. First, the radiation impedance of a single ring transducer as a function of the contact radius or lumped displacement should be determined. Here the deflection profile of a collapsed membrane should be used. The resulting radiation impedance should be utilized for the calculation of the mutual impedances between two collapsed membranes. Finally, the radiation impedance of a single membrane and the mutual radiation impedances should be combined to achieve the radiation impedance of a complete array of CMUT membranes. This procedure is applied to uncollapse mode CMUTs in [67] and can be used to calculate the radiation impedance seen by CMUT arrays of any size.

Chapter 4

Fabrication of CMUTs

Several micro-fabrication methodologies were utilized in the past for the production of CMUTs. The first CMUTs [1] utilized a silicon dioxide sacrificial layer process. Later, other sacrificial layer processes [4,17,18] were developed for creating the cavity structure. More recently, an alternative method, wafer bonding technology [10, 25], has been utilized for producing suspended membrane structures. The assessment of the advantages and disadvantages of CMUT microfabrication technologies is not on the scope of this thesis. Nevertheless, here in this chapter of this thesis, we will detail the fabrication process we developed and used at Bilkent University, for future reference.

We used a surface micromachining technology similar to that in [17] utilizing a chromium sacrificial layer and silicon nitride dielectric deposited by a Plasma Enhanced Chemical Vapor Deposition (PECVD) system[1]. A flowchart of the fabrication process is depicted in Fig. 4.1. Film characteristics deposited by this PECVD reactor is given in Table 4.1. We performed a 3" wafer process on highly doped ($< 0.005\ \Omega$-cm) n-type silicon wafers[2]. The thickness of the membranes is constant for the CMUTs on the same wafer. CMUT cells with radii from 20 μm to 50 μm were fabricated on arrays sized 700 μm by 700 μm and 1 mm by 1 mm.

---

[1] VAKSIS Ltd. Sti., Ankara, TURKEY.

[2] Silicon Quest International Inc., CA, USA.

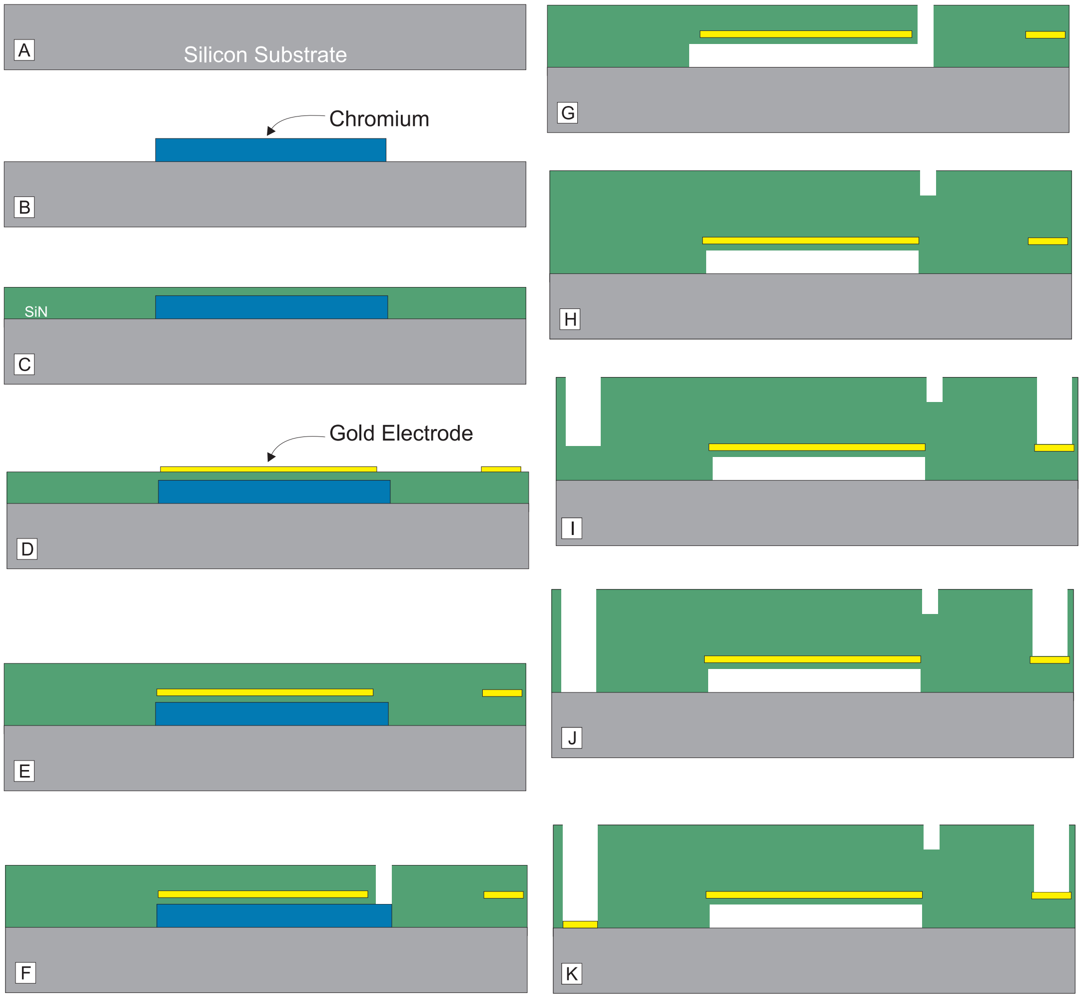

Figure 4.1: Fabrication flow of CMUTs performed at Bilkent University, using a low temperature (250°C maximum) surface micromachining technology.

4.1 Bottom Electrode

We chose to utilize no ground electrode metal and fabricated the devices on top of a highly doped silicon substrate. This choice increases the parasitic capacitances, especially on the pad regions; however, it is the simplest way and increases the yield immensely. The fabrication process was started with a ∼330 μm thick, low resistivity (<0.005 Ω-cm), n-type 3" prime silicon wafer. This low resistivity wafer is the ground electrode for the whole wafer and provides one of the electrical terminals for the CMUTs. Thinner wafers with similar electrical properties could be used in

Material Parameters of SiN_x	
Young's modulus, E	110 GPa
Poisson's ratio, ν	0.27
Dielectric permittivity, ϵ_r	5.4
Density, ρ	3.1 g/cm^3
Intrinsic Stress, T	$\sim$ 20 MPa Tensile

Table 4.1: Silicon nitride properties used in fabrication process.

order to shift the acoustical resonance of the substrate to higher frequencies. The wafers were cleaned thoroughly using a standard RCA[3] clean for 10 minutes before the process.

4.2 Sacrificial Layer

No isolation layer was used between the silicon wafer and the sacrificial layer. Therefore sacrificial layer deposition for defining the cavity is the first operation performed on the cleaned wafer. A chromium layer was used as the sacrificial layer. Chromium was chosen because of its low surface roughness and good etch selectivity to silicon nitride membrane layer in chromium etchant solution. Therefore during the long release step, the membrane is not damaged because of the chemicals.

The thickness of the chromium layer determines the gap height, therefore affects the collapse voltage of the device. For defining the cavity t_g nm thick chromium was sputtered[4] and photolithographically patterned as the sacrificial layer. For patterning the sacrificial layer, we used a commercially available chromium etchant, CR-7S[5].

---

[3] RCA Solution: (1:1:5) NH_4OH:H_2O_2:H_2O at 80°C.

[4] Sputtering is performed on Chromium target with 125 Watts RF power and 250 sccm Argon flow. With this process parameters, the deposition speed is ~ 3/s.

[5] Cyantek Inc.,Freemont, CA, USA.

SiN_x Deposition	
Temperature	250°C
Power	9 Watts
Pressure	1000 mTorr
%2 SiH_4 in H_2	200 sccm
NH_3	4 sccm
He	50 sccm
N_2	75 sccm
Deposition speed	$\sim 10\ /s$

Table 4.2: Low stress (∼20 MPa tensile) silicon nitride deposition conditions in VAKSIS PECVD reactor.

4.3 Insulation Layer

To prevent any defects or contamination in the membrane, a cleaning step in Piranha[6] solution for 10 minutes was performed on the wafer before deposition of the silicon nitride. The chromium sacrificial layer is chemically resistant to Piranha solution.

A silicon nitride film with a thickness of t_i was deposited as the insulation layer using the PECVD system. The thickness of the insulation layer is determined considering the largest voltage to be used on CMUTs as discussed in Section 5.3.

Since the insulation layer is deposited after the sacrificial layer formation, it is a part of the suspended membrane. Therefore, the internal stress of the silicon nitride film must be minimum to prevent deformation and cracking on the released membrane. A film with approximately 20 MPa tensile intrinsic stress was deposited using the process conditions given in Table 4.2.

4.4 Top Electrode

The top electrode can be fabricated anywhere on top of the cavity. It can be either at the bottom or at the top of the membrane; or sandwiched between silicon nitride

---

[6] Piranha Solution: (1:3:2) H_2SO_4:H_2O_2:H_2O at 100 – 120°C.

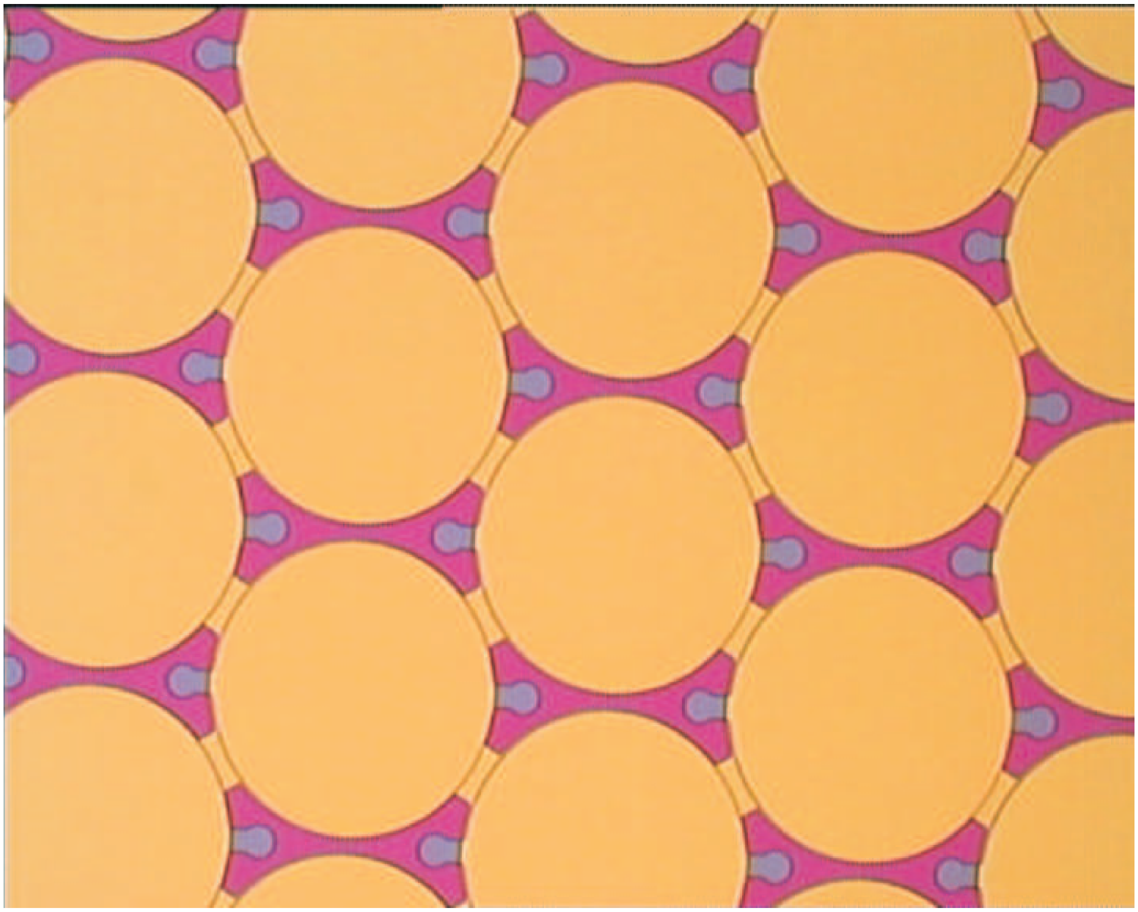

Figure 4.2: A micrograph of a CMUT cell during fabrication after top electrode deposition. The CMUT cell in the micrograph has 40 μm radius. Two smaller circles connected to the cell are the regions for the etch holes, where the chromium etchant enters the cavity during release step.

layers forming the membrane. We chose to deposit the top electrode before the membrane is released, in order to perform the patterning on a rigid surface for increasing the yield of the process.

The material for the top electrode was chosen to be gold. Gold has good electrical conductivity and is resistant to oxidation and chemicals used during the long release step. The only drawback of gold is its poor adhesion to silicon nitride. In order to improve the adhesion, a thin layer of titanium was used at the top and at the bottom of the electrode. A stacked layer of Ti/Au/Ti (15 nm/150 nm/15 nm) was thermally evaporated on the previously patterned wafer. For patterning the

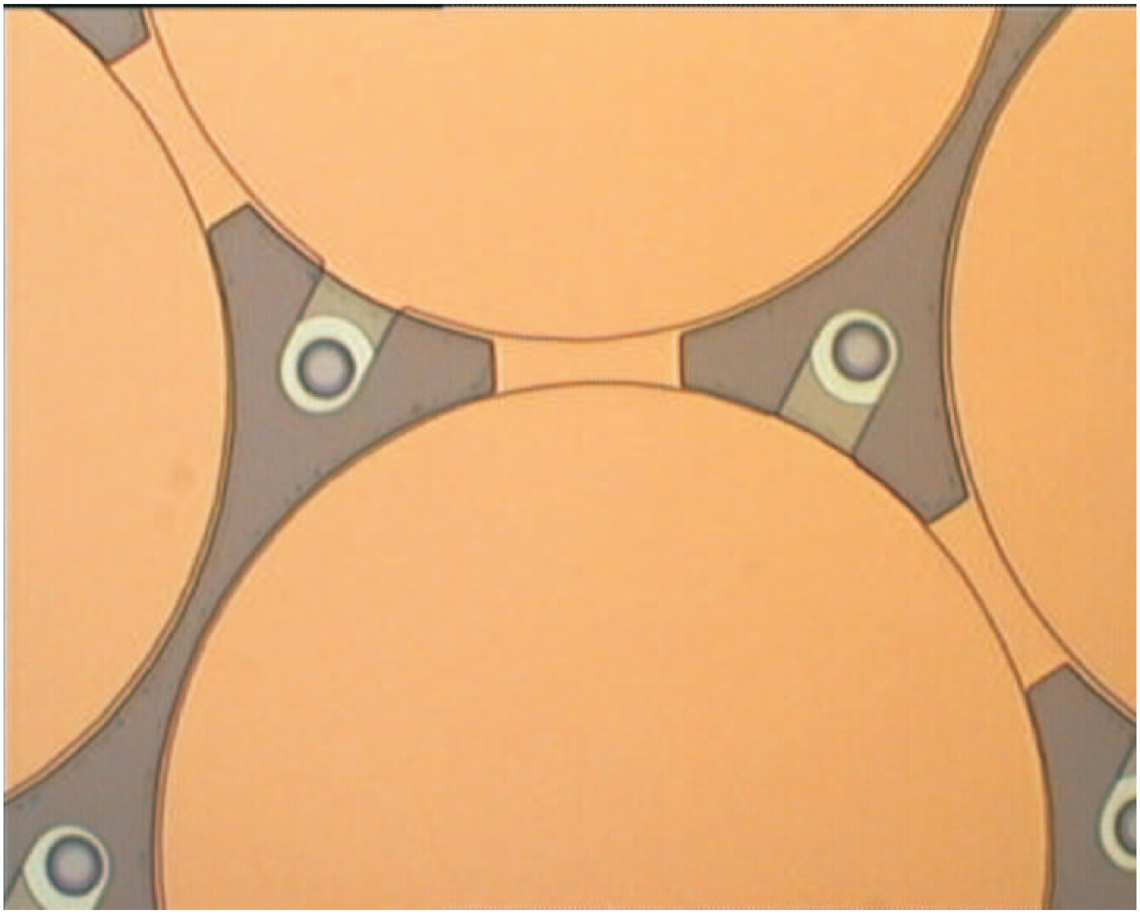

Figure 4.3: A micrograph of a CMUT cell during the release step. The CMUT cell in the micrograph has 30 μm radius. Two smaller circles connected to the cell are the etch holes, where the chromium etchant enters the cavity during release step. Notice that etched and remaining parts of the chromium layer are clearly seen around the etch holes.

wafer, AZ5214E image reversal photoresist of Microchemicals[7] was used. After the thermal evaporation step, the top electrodes were patterned by lifting-off the residual metallization in acetone. For removing any residual metal or photoresist, the sample was immersed in acetone and vibrated in an ultrasonic bath for 5 minutes and thoroughly rinsed. A micrograph of a lifted off top electrode layer is depicted in Fig. 4.2. In this particular example a full coverage top electrode is depicted.

---

[7] Microchemicals GmbH, Ulm, Germany

SiN_x Etching	
Power	150 Watts
Pressure	33 μbar
SF_6	27 sccm
O_2	3 sccm
Etch speed	$\sim 30\ /s$

Table 4.3: Process conditions in RIE for etching silicon nitride.

4.5 Membrane

Approximately 1 μm of silicon nitride on top of the sacrificial layer was deposited before the release step in order to ensure a successful release step. Therefore, we deposited a second layer of silicon nitride after top electrode formation. During the second deposition step, approximately 400-600 nm of silicon nitride was deposited using the same low stress process conditions given in Table 4.2. This additional layer of silicon nitride protects the top electrode from the chemicals used in the release step and provides ease of release without stiction.

4.6 Release

The membrane is suspended by etching the chromium underneath the silicon nitride layer. To allow the chromium etchant to reach the sacrificial layer, small holes were drilled on silicon nitride using a reactive ion etching (RIE) reactor as seen in Fig. 4.3. We designed our photomasks such that each CMUT cell has its individual etch holes and etch channels in order to speed up the release process and increase the yield during the sealing step. The size of etch holes were $2-5$ μm in diameter. The process conditions of the RIE for silicon nitride etching is given in Table 4.3. The chromium sacrificial layer acts as an etch stop for the RIE process. We used the image reversal photoresist, AZ5214E for patterning the etch hole structures, in order to use a light field mask and provide easier and better alignment.

The release process was performed using the chromium etchant solution, CR-7S, which has very good etch selectivity to silicon nitride [17]. After 3-12 hours, when

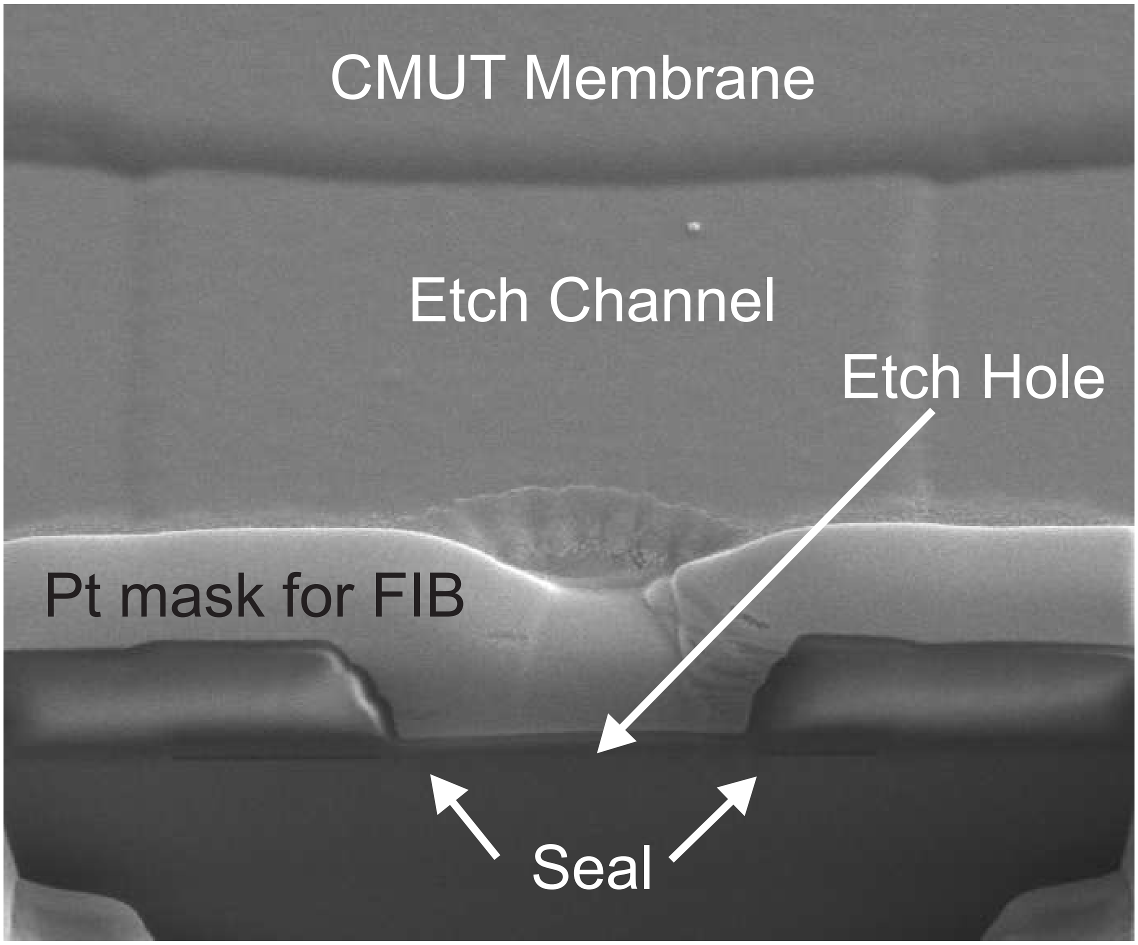

Figure 4.4: An SEM image of the cross section of an etch hole. The platinum mask is deposited by FIB while cross-sectioning the etch hole and it is not a part of CMUT.

all the chromium in the cavity was etched away, the wafers were rinsed in deionized wafer for an extra hour in order to get all the chromium etchant out of the cavities. The release duration depends on the cavity and etch hole size. The micrograph in Fig. 4.3 is a snapshot of the release process after a few minutes, where the etched and remaining parts of the chromium layer are clearly seen around the etch holes.

In the release process, it is expected that each membrane is released from the substrate and suspended. However depending on the size of the membrane, the thickness of the cavity and the intrinsic stress of the membrane nitride, we faced problems suspending the membranes after the wafer was dried off. Some of the membranes were not released and were stuck to the substrate, which is a well known phenomena

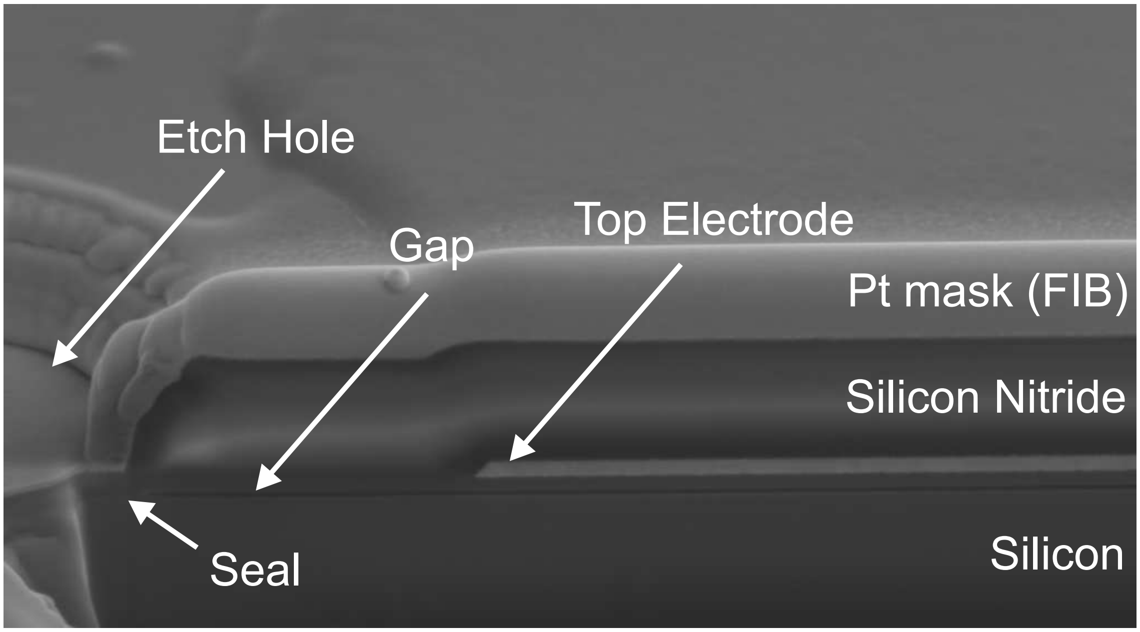

Figure 4.5: An SEM image of the cross section of a fabricated CMUT cell with a radius of a=30 μm and a thickness of 1.8 μm. The gap height is 80 nm.

called stiction for surface micromachined suspended MEMS structures [83, 84]. The problem for CMUTs is due to the adhesion of membrane surface to the substrate when the restoring force of the membrane is unable to overcome the capillary and van der Waals forces during the dry-off process. In the case where a methanol bath was used for an extra hour before drying, this problem was less since the adhesion force is smaller in the case of methanol. The best way to deal with this problem, however, is using a critical point dryer. We used a critical point dryer system[8] (Autosamdri-815B) after the release etch step, if the gap height is small ($t_g < 150\ nm$) and the membranes are large ($a > 30$ μm).

4.7 Sealing

In order to prepare the CMUTs for immersion experiments, the etch holes were sealed by depositing a final layer of silicon nitride, using the same deposition conditions in Table 4.2. After this last deposition, the membranes reach their final thickness of

---

[8] Tousimis Inc, Rockville, MD, USA.

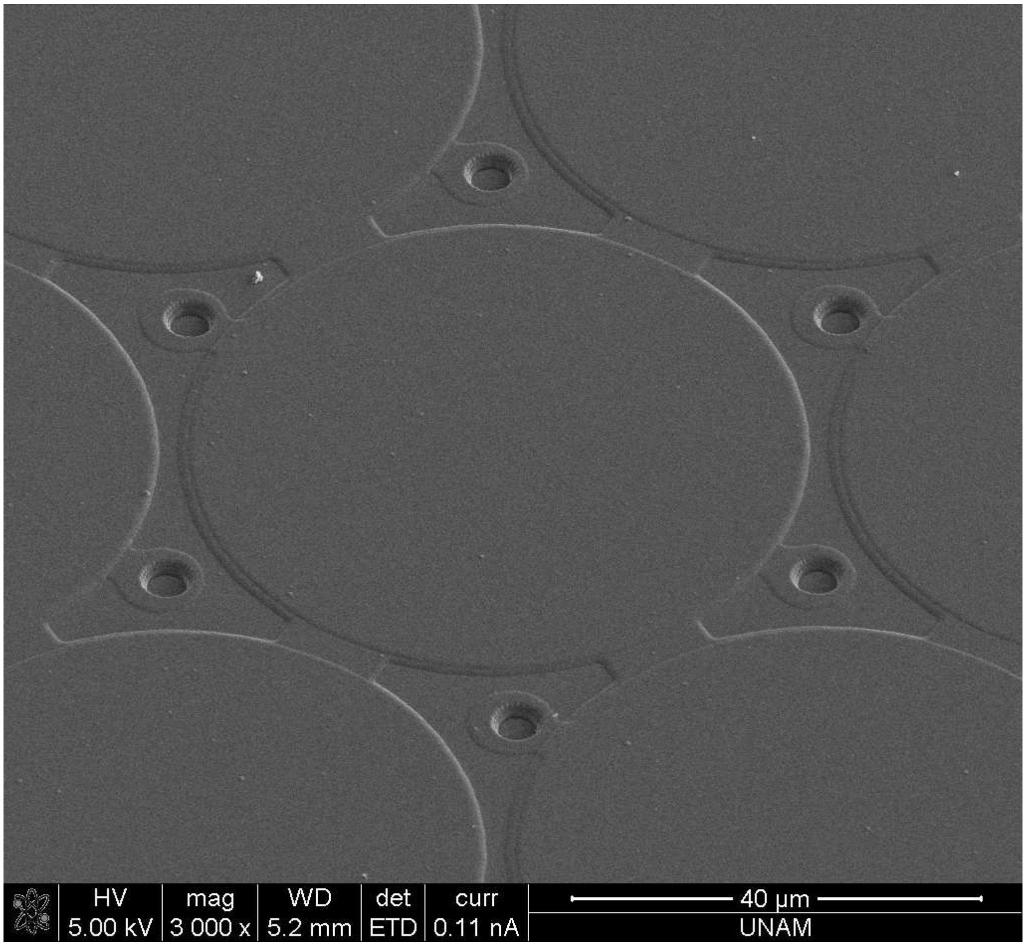

Figure 4.6: A SEM image of a fabricated CMUT array with full electrode coverage top electrodes. Sealed etch holes are seen at the corners of a CMUT cell.

t_m. The thickness of this last silicon nitride film should be at least twice the gap height in order to ensure a successful sealing. A successful sealing can be seen in Fig. 4.4, where a cross section of an etch hole is depicted by a focussed ion beam.

4.8 Contact Pads

Finally, for removing the silicon nitride layer over the bond pads, an RIE process was performed using the process conditions listed in 4.3 and a thick photoresist as the etch mask. The process was stopped, when silicon and Ti/Au/Ti layers were reached. As the final step, a stacked layer of Ti/Au/Ti (15nm/150nm/15nm) was thermally evaporated on the previously patterned wafer and lifted-off in acetone for achieving more reliable bonds. This final deposition does not require an additional mask or photolithography step, since the photoresist previously laid for etching can be used for metal evaporation.

The electrical connections to the electrodes are achieved using contact pads connected to arrays. The size of the pads was chosen to be 200 μm by 200 μm. The separation of the pads are 200 μm in order to comply with the probe station requirement. Fig. 4.5 depicts a scanning electron microscope (SEM) image of the cross section of a fabricated CMUT cell with full top electrode coverage. The thickness of the membranes is 1.8 μm over a 80 nm of gap. Other preparation steps for immersion experiments are discussed in Appendix B. The scanning electron microscopy image of the cell as a part of an array is seen in Fig. 4.6.

Chapter 5

Deep Collapse Mode

The radiated pressure output from a CMUT when it is excited by an electrical pulse is related to the forces acting on the membrane during the pulse cycle. During any unipolar pulse excitation, the membrane movement can be investigated in two parts: collapse and release. In the following analysis we investigate the electrical and mechanical forces acting on a CMUT membrane during the collapse and release parts of a pulse cycle. The membrane deflection profile and the forces acting on the membrane, which were investigated in Chapter 2, are used for understanding the energy transfer of a CMUT to the medium.

5.1 Energy Delivered from a Transmitting CMUT

In the following analysis, we use the average displacement, x_{avg} as the lumped displacement measure in order to calculate the stored energy, E_p in a deflected CMUT membrane correctly without a correction term as seen in equation (2.17). The mechanical energy stored by a deflected membrane is released to the immersion medium when the voltage across the membrane becomes zero. The stored energy can be calculated by integrating the restoring force of the membrane with respect to average displacement to find the area of the dark shaded region in Fig. 5.1. For this example, the area is calculated as 0.63 nJ . The displacement and the mechanical

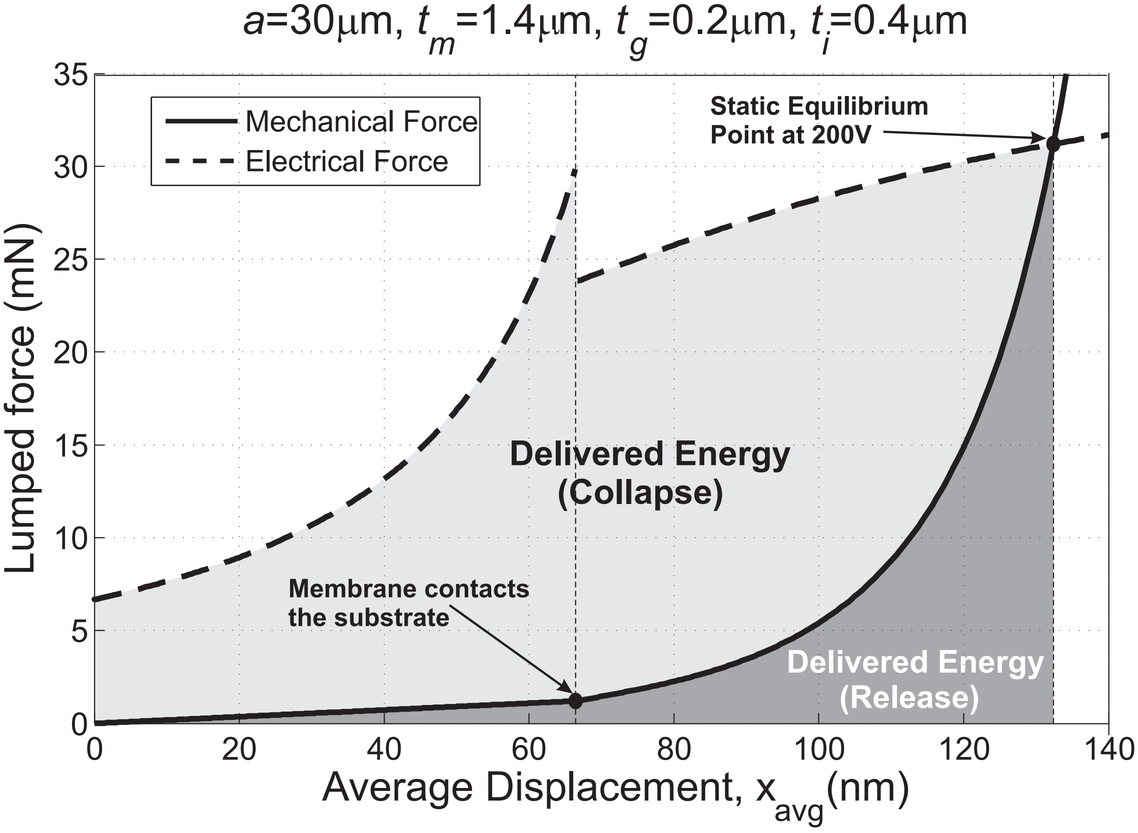

Figure 5.1: The electrical attraction force (dashed) at a bias of 200 V and the mechanical restoring force (solid) as a function of average displacement, x_{avg}. The membrane has a radius of 30 μm and a thickness of 1.4 μm. The buried electrode covering the full surface is 0.4 μm away from 0.2 μm thick gap.

restoring force have a linear relation in the uncollapsed region. When the membrane touches the substrate, the relation becomes highly nonlinear and the amount of energy stored in the membrane increases faster compared to the uncollapsed region.

When a high voltage is applied across the electrodes of a membrane, a part of the input electrical energy is stored as the mechanical energy while another part is delivered to the immersion medium due to the membrane motion. Since the net force applied to the medium is the difference between the electrical and restoring force curves, the energy transferred to the medium can be found using the integral in (2.16), which is equal to the area between the two curves. This area corresponding to an energy of 2 nJ is shown as the light shaded region in Fig. 5.1.

Using the analytical expressions, we calculate the total energy released from a

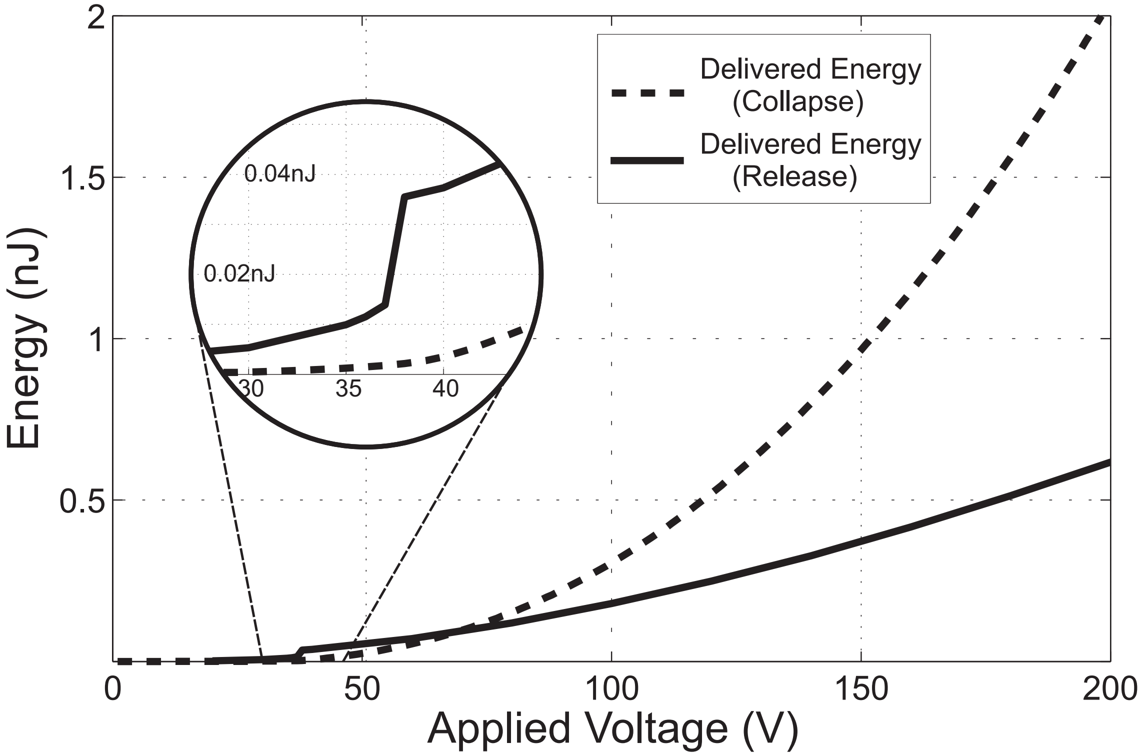

Figure 5.2: Delivered energy during the release (solid) and collapse (dashed) parts of a unipolar pulse cycle. CMUT parameters: $a = 30\mu$m, $t_m = 1.4\mu$m, $t_g = 0.2\mu$m, $t_i = 0.4\mu$m.

membrane during a pulse cycle for different bias voltages. The energies delivered to the medium during the collapse and the release parts are shown in Fig. 5.2 as two separate curves as a function of applied voltage. Clearly, more energy is delivered during the collapse part as compared to the release part of the pulse cycle. The difference increases as the pulse amplitude is increased further. We note this asymmetry does not exist for the uncollapsed operation when the membrane acts like a linear spring.

The effect of the collapse mode on the output pressure is striking as pointed out in the previous studies [52–54]. Moreover, increasing the voltage beyond the collapse voltage increases the radiated energy considerably in both collapse and release parts of a pulse cycle. We call this operation the *deep collapse mode*, where the nonlinear forces are utilized during the transmission cycle, well beyond the collapse point. We should note that this mode is effective if we have a full-coverage top electrode. For

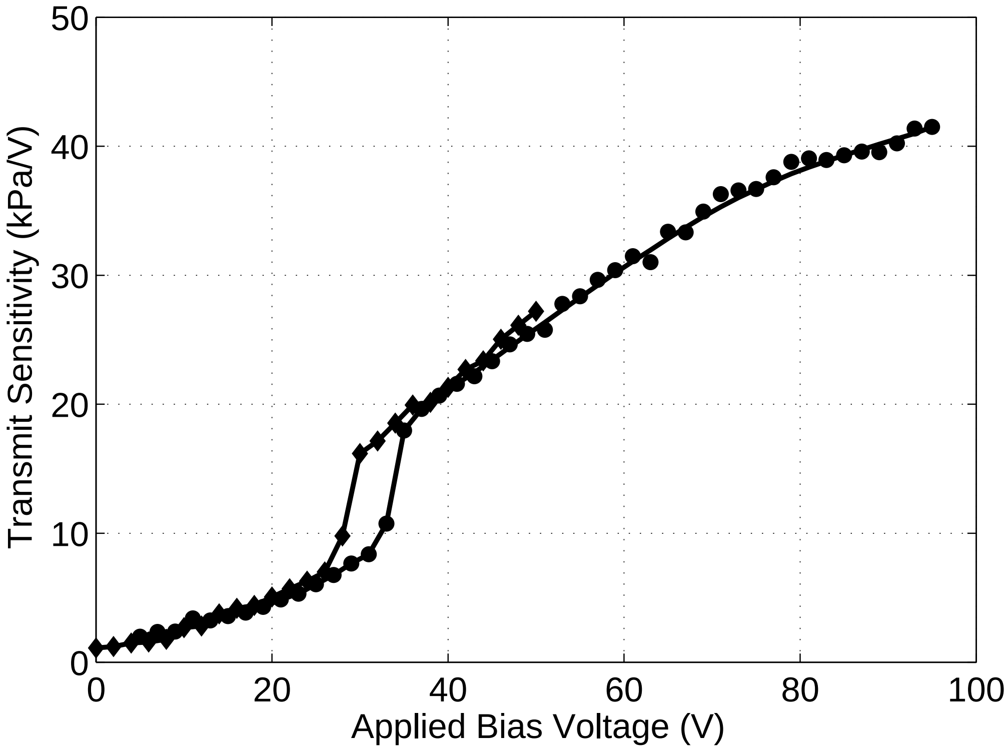

Figure 5.3: Measured peak-to-peak pressure at the surface of the CMUTs when excited by a 40 ns long, 5-V pulse while the bias is being monotonically increased (circles) and monotonically decreased (diamonds). CMUT parameters: $a = 30\mu$m, $t_m = 1.4\mu$m, $t_g = 0.2\mu$m, $t_i = 0.4\mu$m.

the case of a partial electrode, the membrane cannot store any more energy once the contact radius (b in Fig. 2.2) is equal to the electrode radius.

For the demonstration of the use of deep collapse mode for high transmit efficiency, we use fabricated CMUTs on a transmission experiment setup with a calibrated hydrophone. The details of the fabrication process is discussed in Chapter 4 and the experimental setup is demonstrated in Appendix B. A 40 ns pulse with 5 Volts amplitude is applied to the CMUT array while the DC bias is varied. The measured peak-to-peak pressures are plotted in Fig. 5.3. The circles are the measured peak-to-peak pressure values while the DC bias voltage is monotonically increased and the diamonds are the pressure values when the bias is monotonously decreased. The hysteretic snap-back behavior of the CMUT can be clearly seen in this figure. A transmit sensitivity of more than 40 kPa/V is measured when a

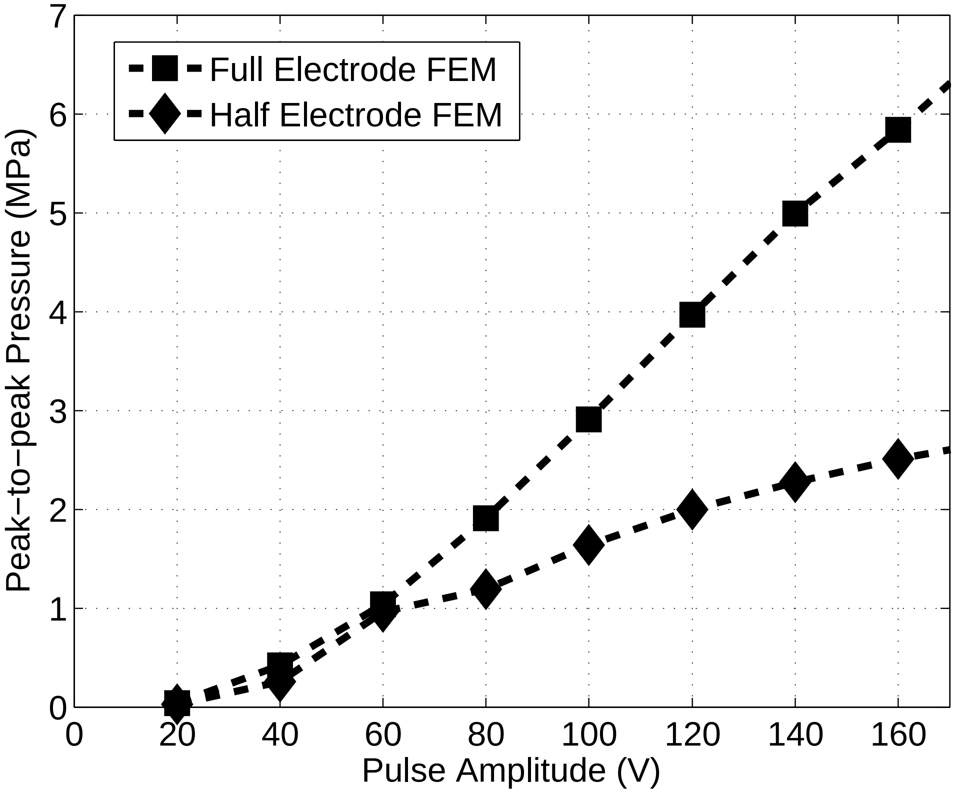

Figure 5.4: Simulated peak-to-peak pressures at the surface of a CMUT when excited by a 40 ns long negative pulses while the pulse amplitude is monotonically increased for half electrode and full electrode coverage. The pulse is applied on top of an equal amplitude DC bias. CMUT parameters: $a = 30\mu$m, $t_m = 1.4\mu$m, $t_g = 0.2\mu$m, $t_i = 0.4\mu$m.

95 Volts bias is used as compared to 20 kPa/V at the edge of snap-back. With a partial electrode coverage, e.g., 50% coverage [53], the transmitted pressure amplitude saturates for bias voltages higher than a certain value, since the electrode region of the membrane fully collapses when that voltage is reached and increasing the voltage does not provide more force. The effect of the electrode coverage is investigated in the following section.

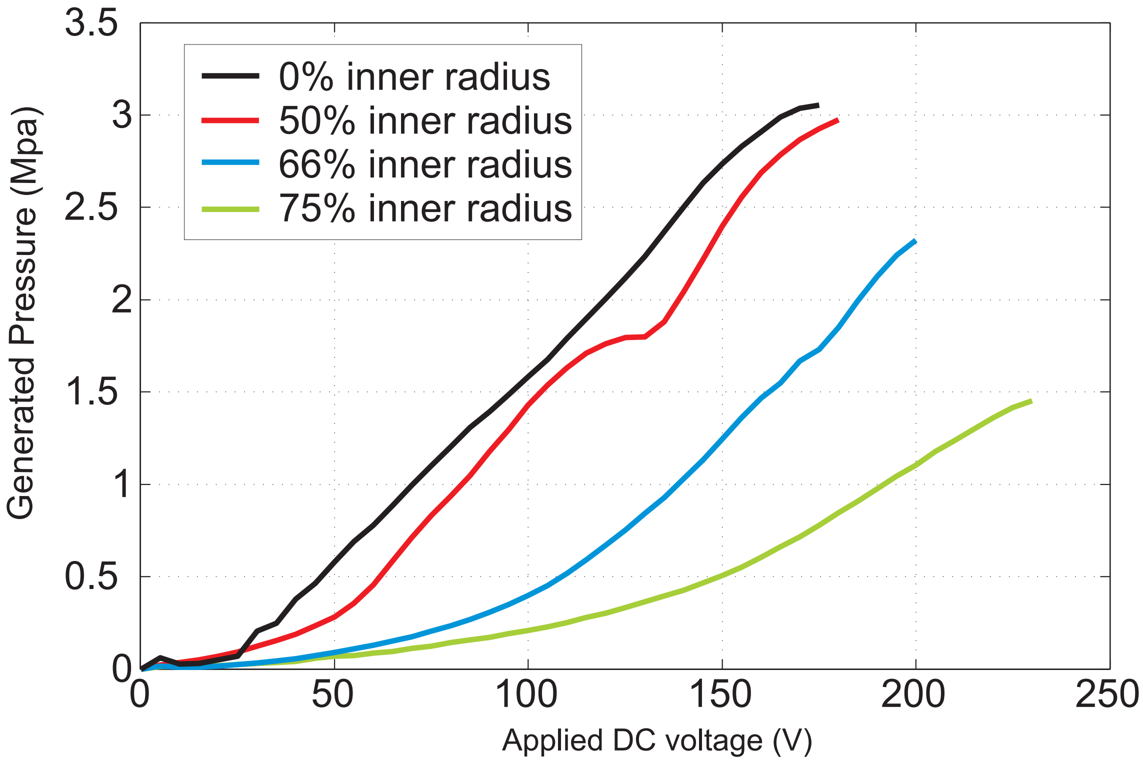

Figure 5.5: Experimental results of the transmission experiments performed on fabricated CMUT arrays. Different curves indicate the pressure output of different arrays with different ring shaped electrode coverage. CMUTs are excited by 40 ns long negative pulses while the pulse amplitude is monotonically increased. The pulse is applied on top of an equal amplitude DC bias. CMUT cell dimensions: $a = 30\mu$m, $t_m = 1.4\mu$m, $t_g = 0.2\mu$m, $t_i = 0.4\mu$m.

5.2 Electrode Coverage

The effect of the electrode coverage on the output pressure is tested using the FEM simulations and experiments. In Fig. 5.4, the results of the FEM simulations show that maximum pressure from a CMUT cell can be achieved using full top and bottom electrode coverage. The superiority of full electrode coverage over partial coverage can be seen in the figure. The pressure generated by CMUTs with half electrodes saturate, however CMUTs with full electrode coverage can still respond to increased pulse amplitude. Electrode coverage can be smaller than 100% of the active membrane region and the output pressures can still be high enough if the electrodes cover the center region and the remaining uncovered parts are at the edges, where there

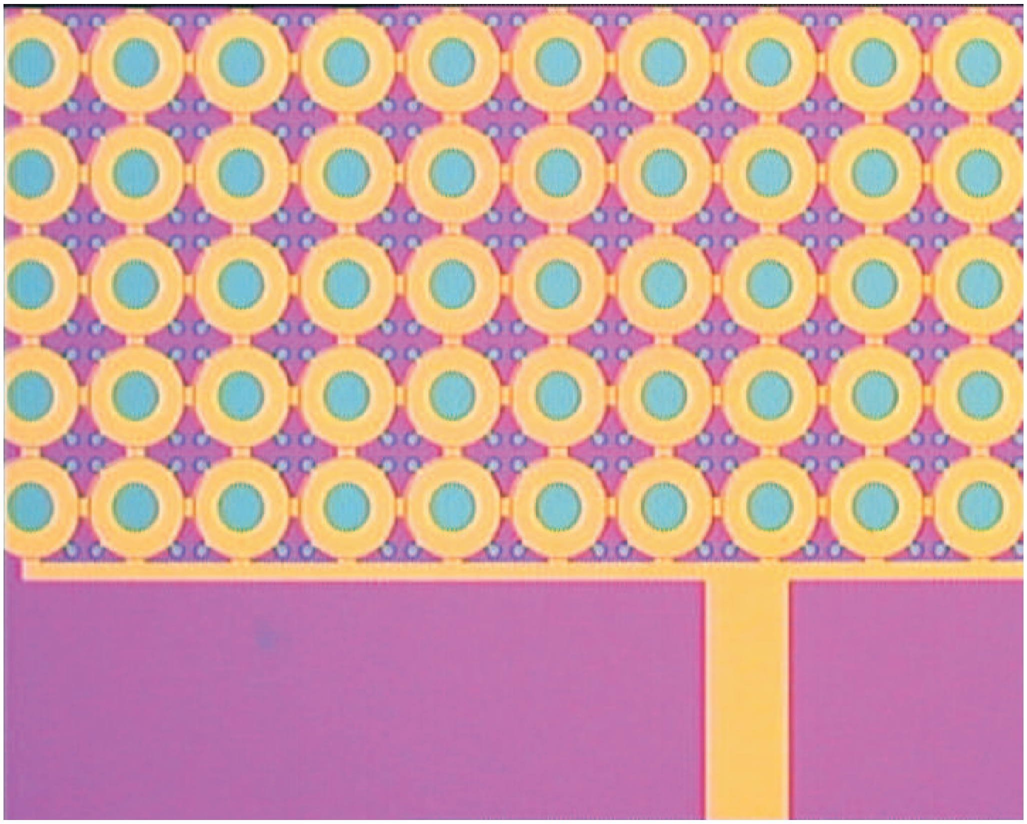

Figure 5.6: An optical micrograph of a fabricated CMUT array. The ring shaped top electrode has 50% inner radius. at 121 cells (11 by 11) each with a radius of a=30 μm and a cell to cell separation of 5 μm. The aperture size is 0.71 mm by 0.71 mm and the fill factor is 67%.

is little contribution to electrostatic forces. Nevertheless, it is best to fabricate the top electrode covering the full surface of the moving membrane.

One may argue that, the efficiency of a CMUT can be increased by utilizing a ring shaped top electrode covering the sides of the CMUT membrane, in order to reduce the capacitance at the center portion of the CMUT since, during the collapse mode of operation the center portion of the membrane stays in contact with the substrate. We have fabricated CMUT structures with different electrode coverage at the sides of a CMUT membrane. A micrograph of a fabricated CMUT array with ring shaped top electrodes is seen in Fig 5.6. For the same membrane dimensions, the transmitted pressure waveforms from different arrays are recorded using a calibrated hydrophone as described in Appendix B. The results are depicted in Fig. 5.5, which indicate the most efficient transmission is achieved using a full electrode coverage. The electrode coverage in the figure is defined using the inner radius of the ring shaped top electrode. The membrane can be collapsed using a smaller electric potential when a full electrode coverage is utilized, therefore a larger portion of the available voltage is used to deflect the membrane in the collapsed state. A half electrode coverage, which is optimal [21] for the non-collapsed operation, is not preferable for the collapse and deep collapse modes.

At the remaining part of this chapter, full electrode coverage is used on the fabricated devices, or full electrode coverage is assumed at the FEM and equivalent circuit simulations, unless otherwise is explicitly indicated.

5.3 Insulation Layer Thickness

One critical parameter for a CMUT cell is the insulation layer between the electrodes, which should be thick enough to withstand the high electric fields, and should be thin enough to maintain most of the field in the vacuum gap. In this thesis, the insulation layer is chosen to be silicon nitride, which has a typical dielectric breakdown field, E_{brk} of 1000 V/μm [85]. The transmitting circuitry in a typical application of CMUT, has a fixed maximum available voltage, V_{max}. The thickness of the insulation layer should be chosen with a safety margin in order to withstand V_{max}.

In Fig. 5.7 and Fig. 5.8, negative and positive pressure pulses calculated by the equivalent circuit simulations as a function of pulse amplitudes are depicted, respectively. Different curves in the figures represent insulation layers with different thicknesses. For a thicker insulation layer, higher maximum voltage amplitude is used. For a fixed maximum voltage, the pressure generated by a collapsing or releasing voltage step increases as the insulation layer thickness is decreased as seen in Fig. 5.7 and Fig. 5.8. In order to keep a safety margin, we choose the thickness of the insulation layer to have a dielectric breakdown voltage, V_{brk} of $2V_{max}$. In other words, the electric field across the insulation layer does not exceed 500 V/μm.

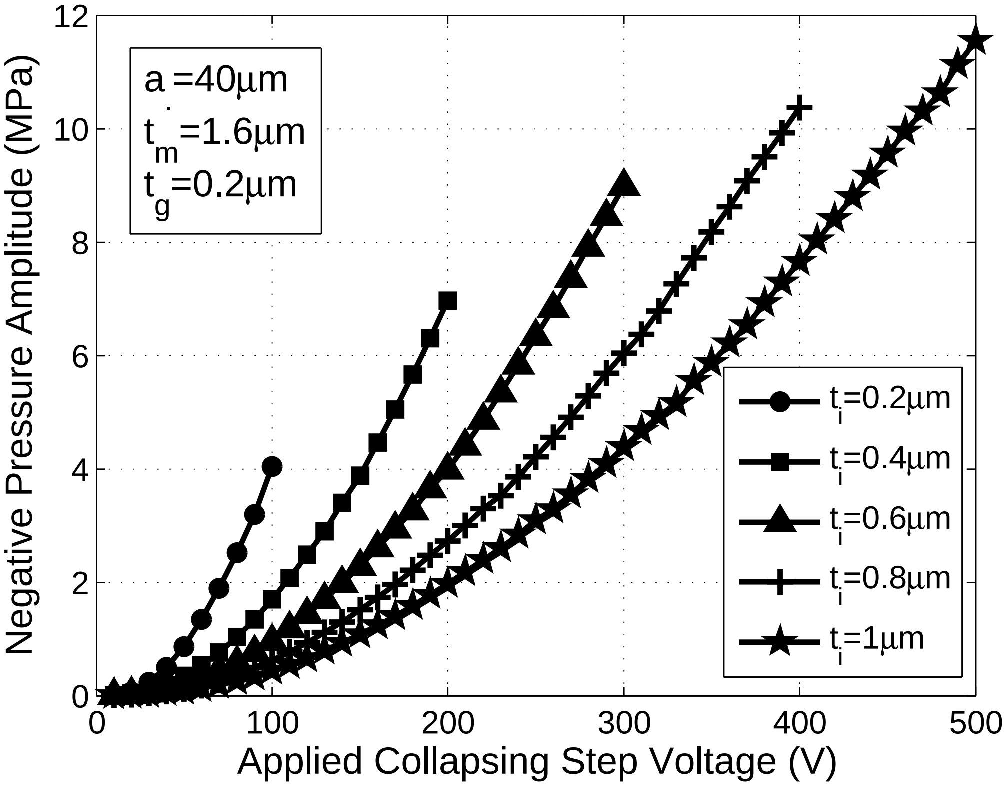

Figure 5.7: Equivalent circuit simulation results of the negative pressure amplitude of the transmitted acoustic signal when the CMUT cells are excited by a collapsing voltage step, with respect to the amplitude of the step for different insulation layer thicknesses.

Above results show that, if there is a voltage limit, 200V for example, the insulation layer thickness, t_i must be at most 0.4 μm for maximum pressure output. The value of the insulation layer thickness should be chosen during the design stage and according to the maximum available voltage and maximum allowable electric field. For this example, 0.4 μm thickness can be easily calculated using the maximum voltage of 200V divided by the half the dielectric strength value which is 500 V/μm. The results are also valid when different insulation materials or maximum operating fields are chosen.

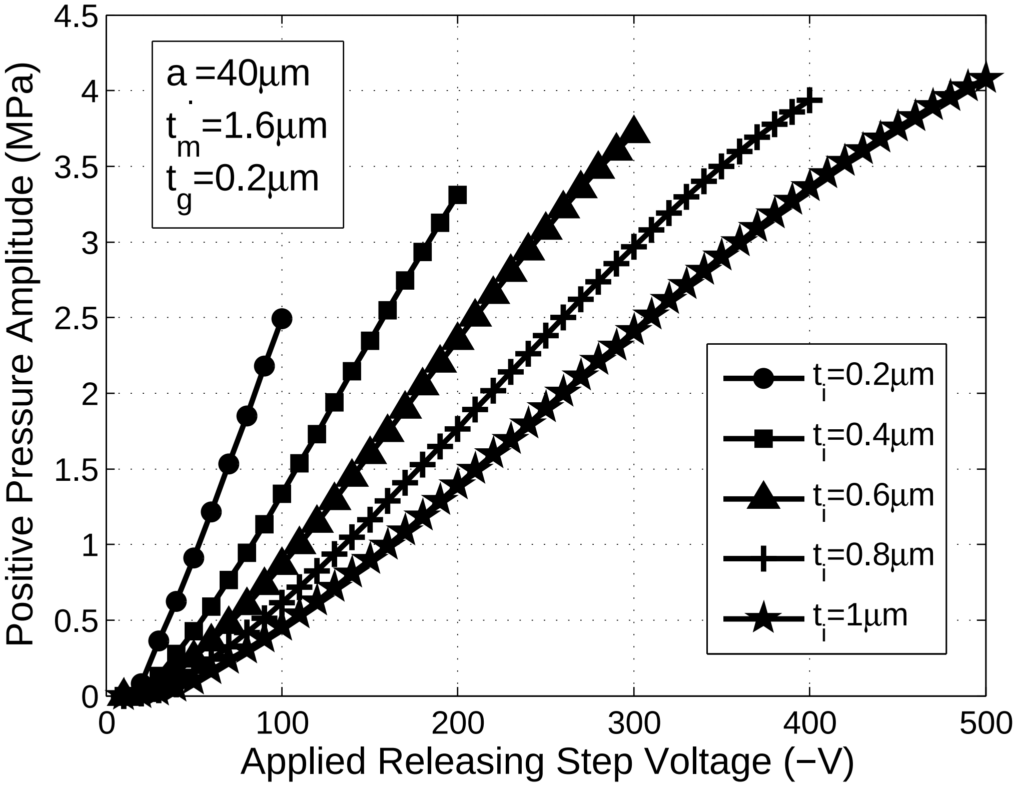

Figure 5.8: Equivalent circuit simulation results of the positive pressure amplitude of the transmitted acoustic signal when the CMUT cells are excited by a releasing voltage step, with respect to the amplitude of the step for different insulation layer thicknesses.

5.4 Rise and Fall Times

Effect of the rise and fall times of a pulse excitation have been determined by using equivalent circuit simulations. The results of the simulations are depicted in Fig. 5.9. +200 V and −200 V collapsing and releasing parts of a pulse are applied to a CMUT, respectively with varying rise and fall times. A +200 V causes the membrane to collapse and it is called as the collapsing voltage step. The rise time of the collapsing edge is not critical up to 40 ns in this example. A reasonable rise time for the collapsing edge can be chosen for high pressure output, such as 25 ns. A −200 V causes the membrane to be released and it is called as the releasing voltage step. The fall time of the releasing step is very prominent and should be chosen

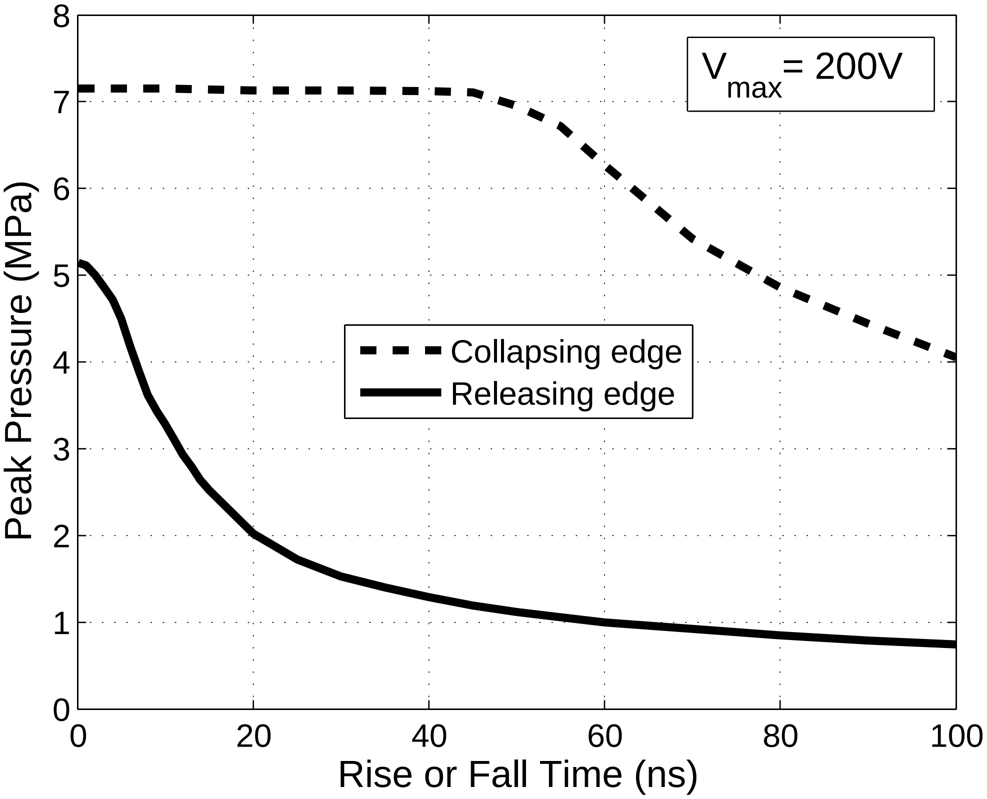

Figure 5.9: Peak pressure of the transmitted acoustic signal when the CMUT cells are excited by a collapsing (dashed) and releasing (solid) voltage steps, with respect to the rise (dashed) and fall (solid) times of the applied step. CMUT cell dimensions: $a = 30\mu\text{m}$, $t_m = 1\mu\text{m}$, $t_g = 0.2\mu\text{m}$, $t_i = 0.4\mu\text{m}$.

very short regardless of the operating frequency of the membrane.

In the remaining part of this chapter, the rise and fall times of the pulses are chosen as 10 ns, for the sake of simplicity. It should be noted here that faster fall times for a pulse excitation would result higher pressures.

5.5 Pulse Width

Usually an acoustic pulse is generated using and electrical pulse comprised of the collapsing and releasing voltage steps as defined in the previous section. The pulse

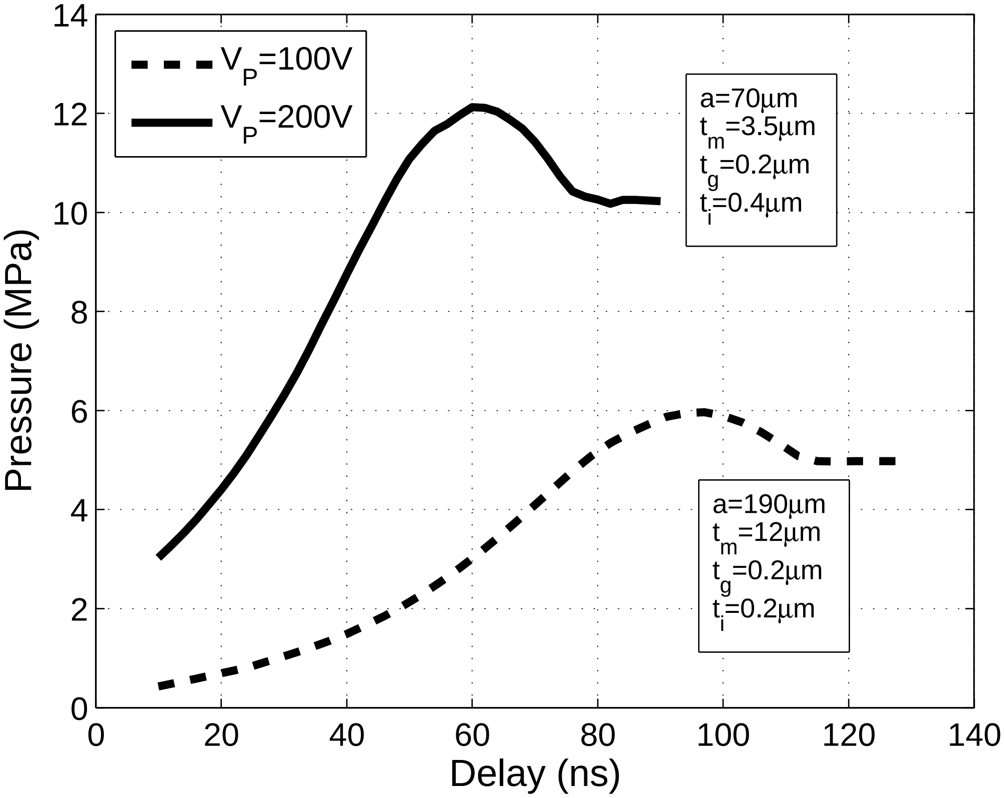

Figure 5.10: Peak-to-peak pressure amplitude of the transmitted acoustic signal when the CMUT cells are excited by a collapsing/releasing voltage steps with respect to the pulse width for voltage amplitudes of 100 V (dashed) and 200 V (solid).

width is the delay between the collapsing and releasing voltage steps. In Fig. 5.10, extracted peak-to-peak pressure values from two different CMUT cells using equivalent circuit simulations are depicted as a function of the pulse width. It is seen from the figure that an optimal pulse width should be utilized in order to achieve a pressure waveform with maximum amplitude. In the remaining part of this chapter, the optimum amount of pulse width is determined and used in all the simulations.

5.6 Pulse Polarity

The order of the collapsing and releasing voltage steps is critical for the acoustical pulse shape. In Fig. 5.11, two different pressure waveforms are depicted, which are

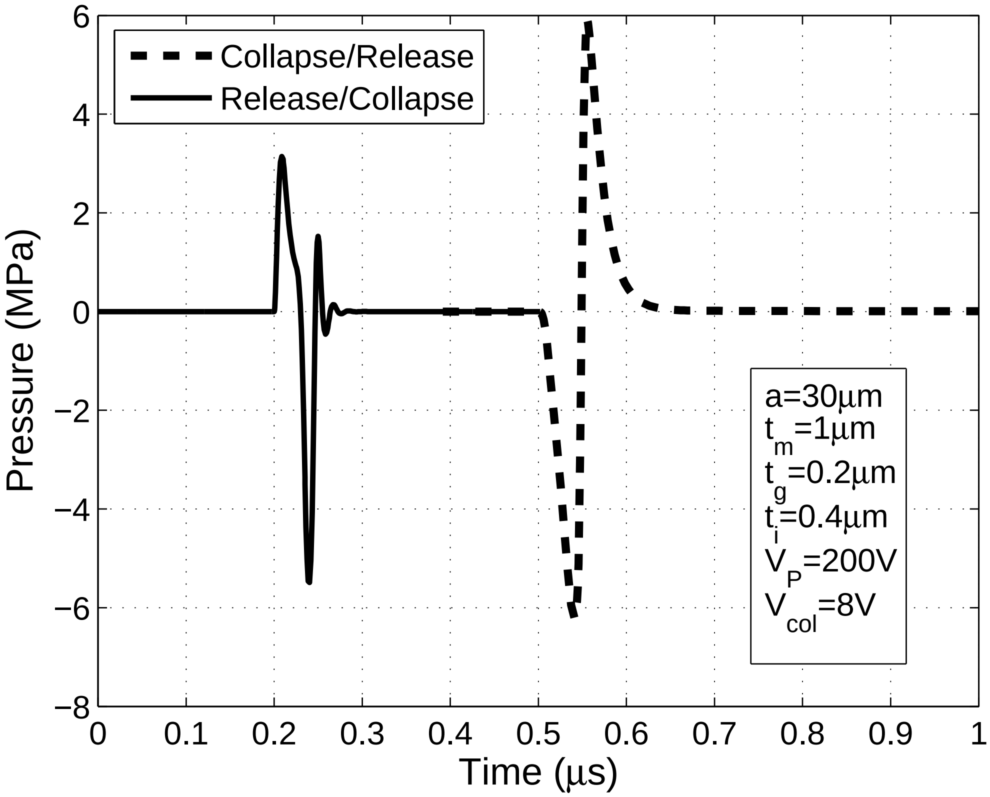

Figure 5.11: Average pressure as a function of time emitted from a CMUT cell for collapsing and releasing voltage steps in opposite orders. The amplitude of the voltage steps is 200V and the pulse width is chosen to be optimum for maximum pressure transmission. CMUT cell dimensions: $a = 30\mu$m, $t_m = 1\mu$m, $t_g = 0.2\mu$m, $t_i = 0.4\mu$m.

obtained by driving the CMUT cell with the same pulse amplitude, but in opposite collapse/release order. For the releasing voltage step, the stored mechanical energy is radiated into the medium as a positive pressure waveform. The membrane is accelerated by high restoring forces and the force acting on the membrane decreases as the membrane is released. Once the membrane transfers its energy to the medium its velocity drops. Therefore a damped waveform is transmitted into the medium. However, in the collapsing voltage step, the electrical forces are low at first and increases with the increasing displacement. Therefore, at the DC stable point the membrane still has high velocity and kinetic energy, which result in an underdamped waveform and ringing. Therefore a collapse/release cycle would result in a better behaving waveform as seen in Fig. 5.11. In addition, the excess energy at the end of the collapsing step can be used advantageously for the releasing step, if the width of the electrical pulse is chosen optimally as discussed in the previous section. This extra energy would result in higher acoustic pressure levels for the collapse/release cycle. A release/collapse cycle, on the other hand, results in shorter acoustical pulses due to high electrical attraction forces at the end of the pulse cycle. In the following sections of this chapter, collapse/release cycle is utilized in the simulations; however, we should note that a release/collapse cycle would result in similar pressure levels and center frequencies.

5.7 Radius and Thickness

In this section, the effect of the membrane dimensions, i.e. radius, a and thickness, t_m, on the pressure output of a CMUT is explored. In order to make a fair comparison, a parameter, γ is defined that will represent the depth of collapse operation. γ is simply the ratio of the peak amplitude of the input excitation pulse, V_{max}, to the collapse voltage of the membrane, V_{col}:

$$\gamma = \frac{V_{max}}{V_{col}} \tag{5.1}$$

A higher γ generates a higher contact radius and a higher lumped displacement during the collapsed state. In Figs. 5.12 and 5.13, the effect of the parameter γ on the average peak-to-peak output pressure for different CMUT cells is depicted using the results of the equivalent circuit simulations. The applied electrical signals to the CMUT cells in the simulations are 100 V and 200 V pulses with optimum pulse widths as discussed in Section 5.5. The rise and fall times of the pulses are chosen to be constant and 10ns. The insulation layer's thickness, t_i is chosen to be 200 nm and 400 nm respectively, using the value of V_{max} and E_{brk} as discussed in Section 5.3. For different curves in the figures, different values of γ are used.

The pressure output that is generated by CMUTs is a strong function of membrane dimensions. Highest peak-to-peak pressure amplitudes are achieved using higher γ values. On the other hand, output pressure amplitudes do not change

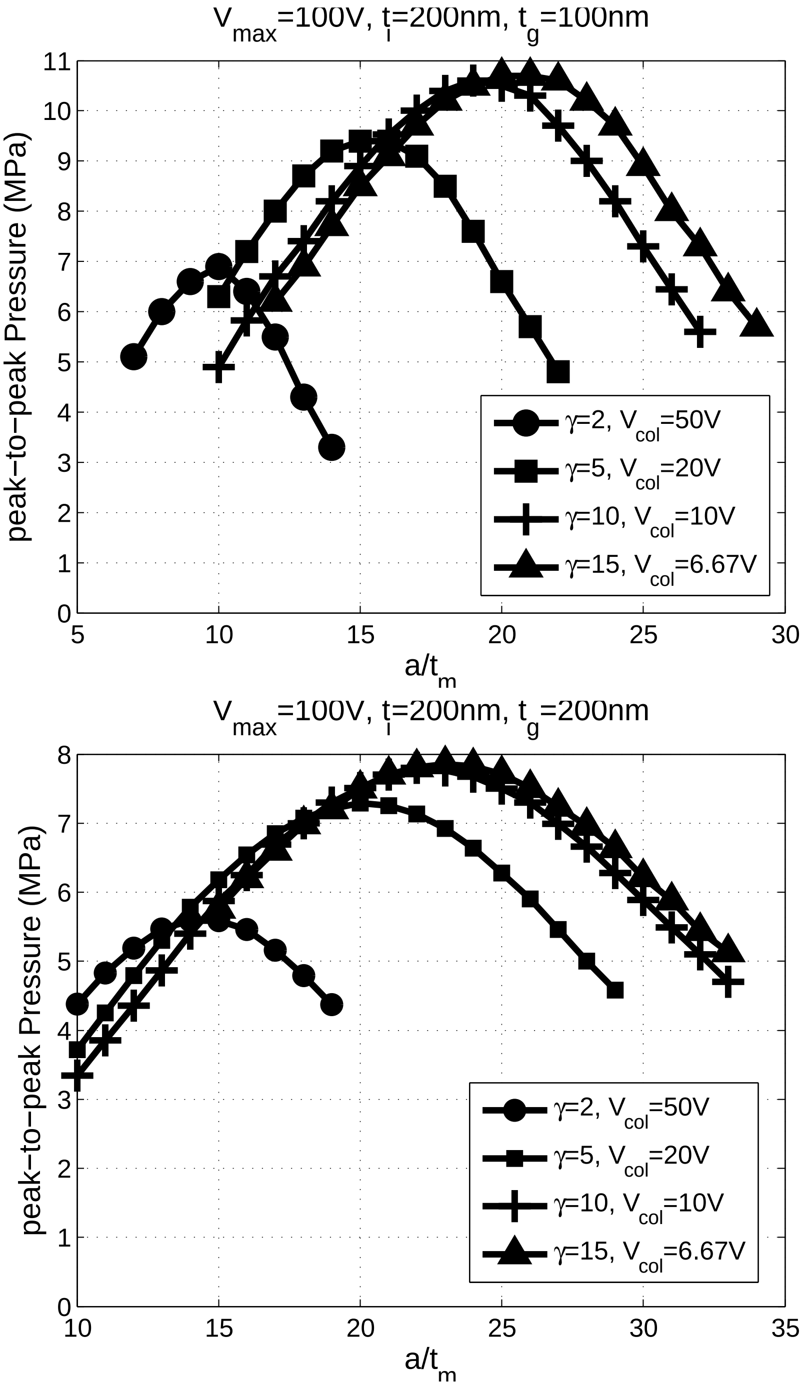

Figure 5.12: Calculated peak-to-peak pressure amplitude of the transmitted acoustic signal when the CMUT cells are excited by a positive pulse of 100V in amplitude, with the optimum pulse width using the equivalent circuit simulations. The pressure levels are depicted for different values of collapse voltages. In the simulations the gap height is chosen to be 100nm (top) and 200nm (bottom).

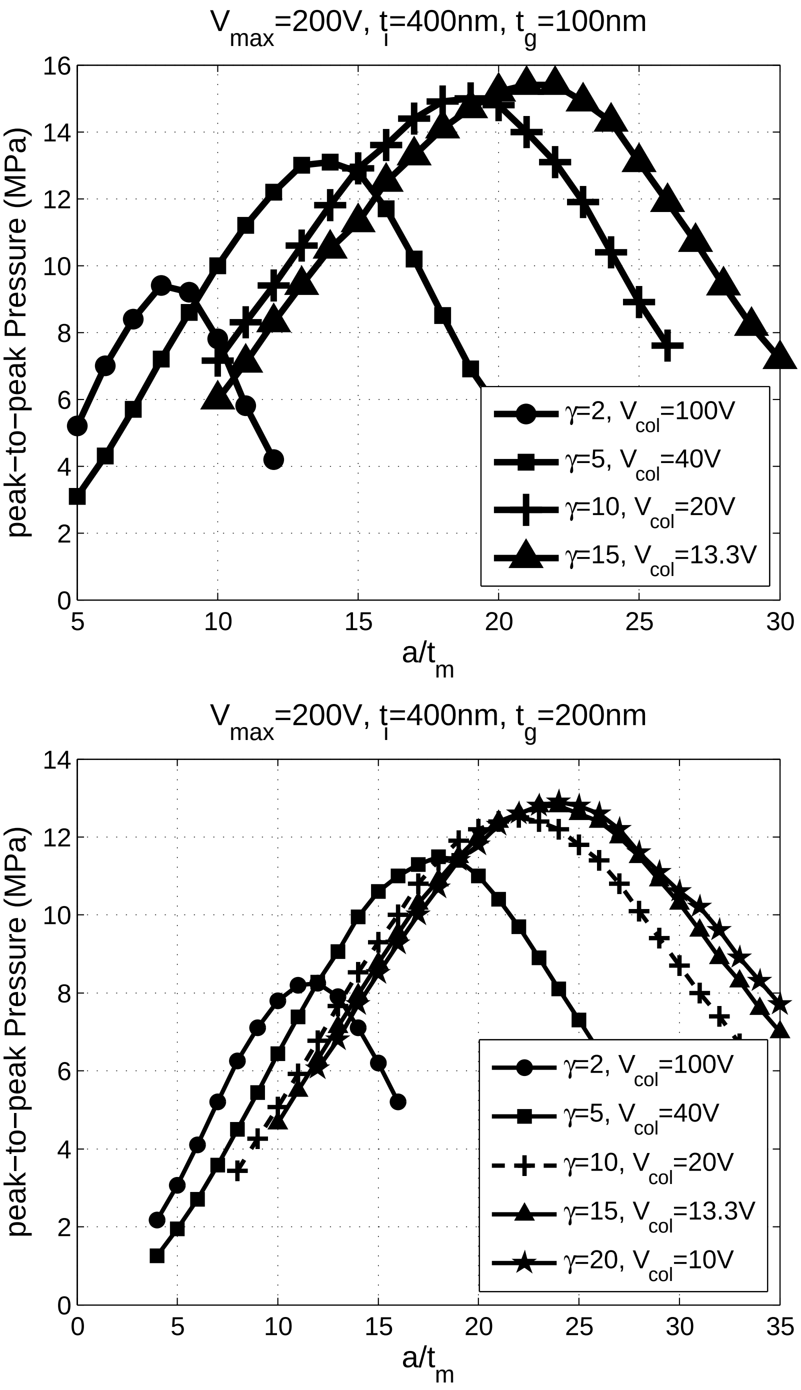

Figure 5.13: Calculated peak-to-peak pressure amplitude of the transmitted acoustic signal when the CMUT cells are excited by a positive pulse of 200V in amplitude, with the optimum pulse width using the equivalent circuit simulations. The pressure levels are depicted for different values of collapse voltages. In the simulations the gap height is chosen to be 100nm (top) and 200nm (bottom).

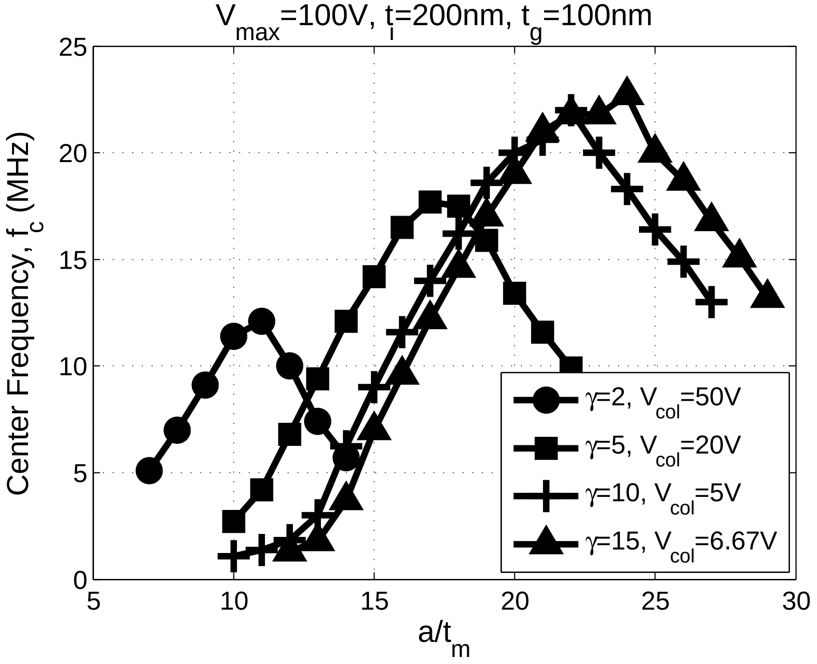

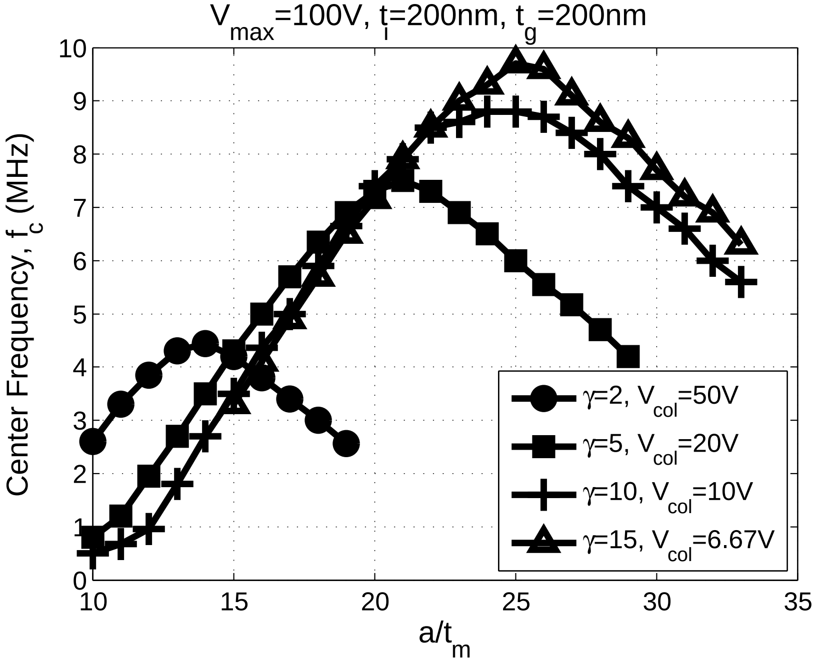

Figure 5.14: Calculated center frequency of the pulses used for depicting Fig. 5.12 using equivalent circuit simulations.

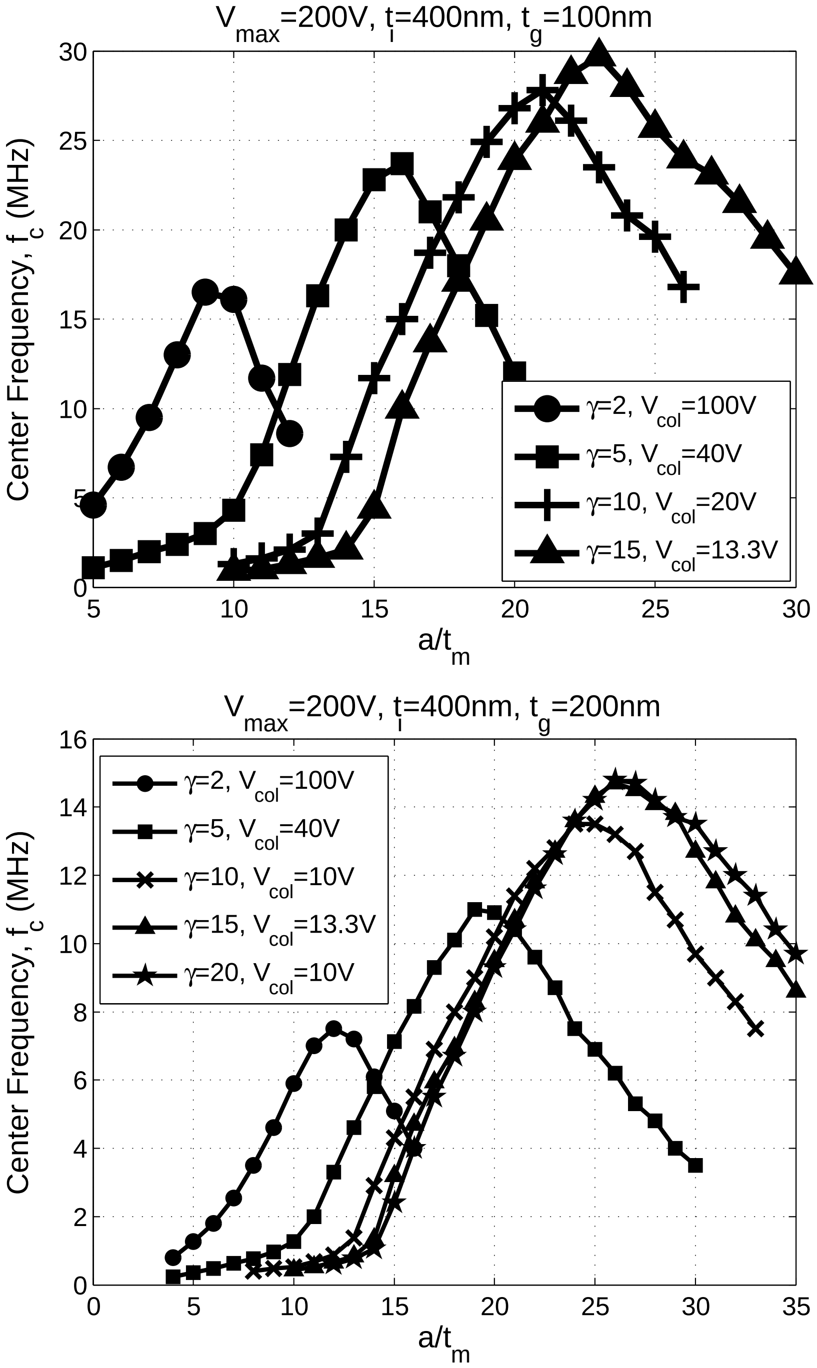

Figure 5.15: Calculated center frequency of the pulses used for depicting Fig. 5.13.

much after the γ value of 5. For values less than 5, output pressure of a CMUT cell decreases quickly. Therefore, the pulse amplitude should be greater than 5 times the collapse voltage in order to achieve high output pressures, which we call *the deep collapse mode* of CMUTs. In addition, the dimensions of the membrane should be chosen such that maximum pressure output can be achieved.

In most cases, high pressure output is not enough to satisfy application specific requirements. The center frequency of the generated pulse is also an important parameter that should be considered. In Figs. 5.14 and 5.15, center frequency of the generated pulses for plotting Figs. 5.12 and 5.13 respectively, is depicted as a function of the membrane dimensions and for different γ values. As expected, the center frequency of the pressure pulse increases with the increasing pressure output. However, the center frequency changes faster than the pressure output, which is a useful property for designing CMUT cells generating high pressure pulses at a desired center frequency. The use of these figures will be demonstrated using design examples in Section 5.9.

5.8 Gap Height

Figures 5.14 and 5.15 show that the effect of the gap height is very prominent on the adjustment of center frequency of the generated pulse. The change of the peak-to-peak pressure and the center frequency of a pressure pulse generated by electrical pulses with 100V and 200V amplitudes are depicted in Figs. 5.18 and 5.17 as a function of membrane dimensions and for different gap heights. The thickness of the insulation layer is calculated using V_{max} and E_{brk} as 200 nm and 400 nm, respectively. A low collapse voltage value is chosen for all simulations in order to achieve high γ values and therefore high amplitude acoustic pulses. As expected, the center frequency of the pulse decreases with increasing gap height. Therefore, gap height is a parameter that would determine the speed of the membrane during the deep collapse mode of operation. Unfortunately, the pressure generated by a CMUT also decreases with the increasing gap height. Nevertheless, the dependency is weaker when compared to the center frequency case.

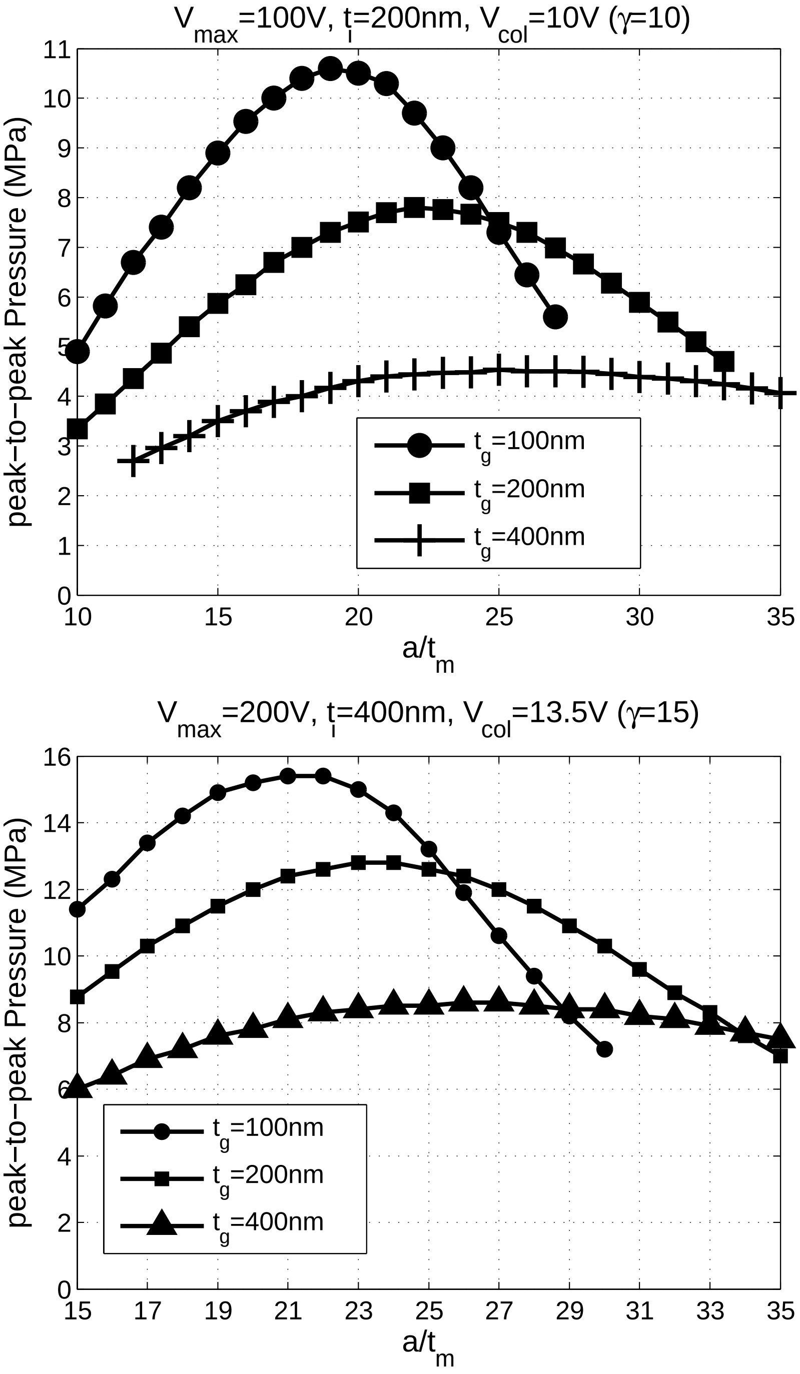

Figure 5.16: Effect of the gap height on peak-to-peak pressure generated by CMUTs when they are excited by 100V (top) and 200V (bottom) pulses with the optimum pulse width. The results are calculated using the equivalent circuit simulations for different membrane dimensions. A fixed collapse voltage is chosen for maintaining a high γ value, 10 and 13.5, respectively.

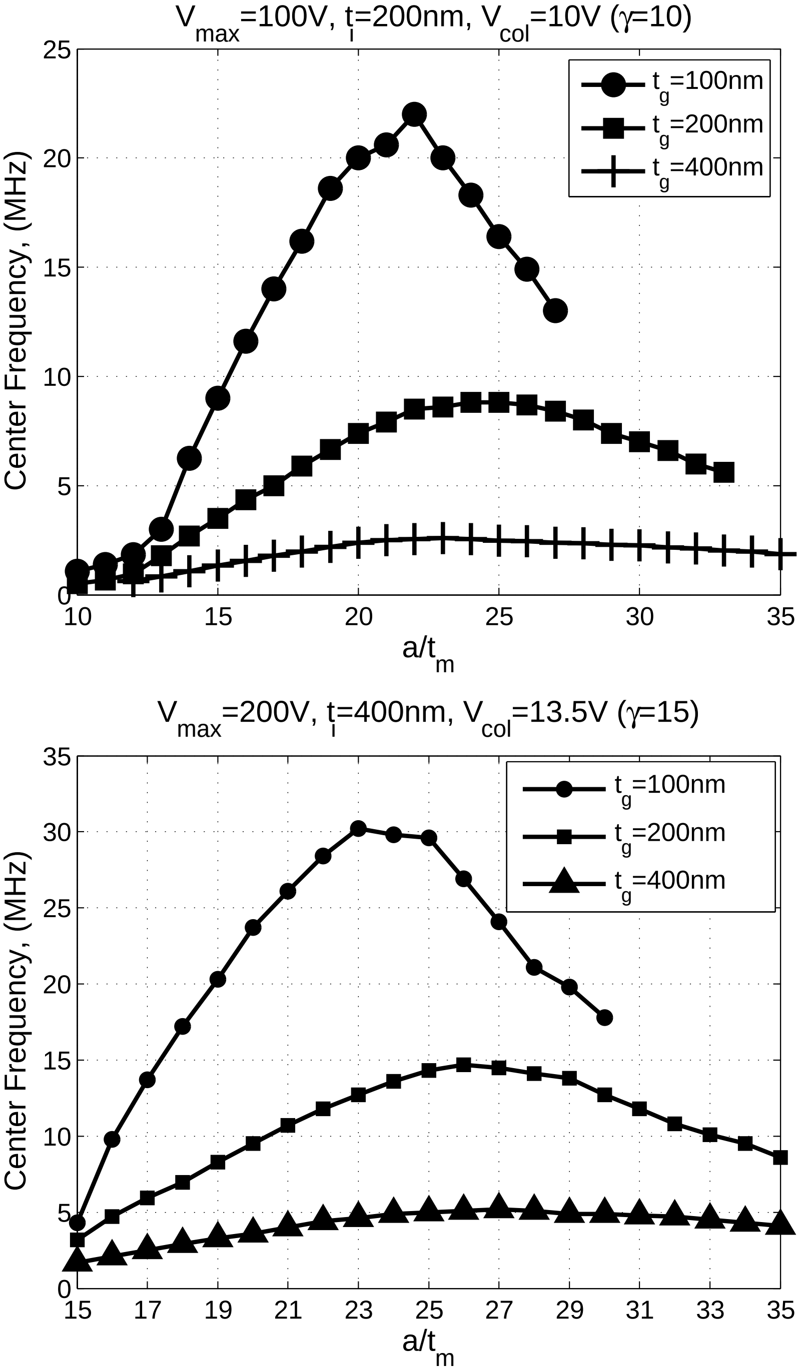

Figure 5.17: Calculated center frequency of the pulses used for depicting Fig. 5.18.

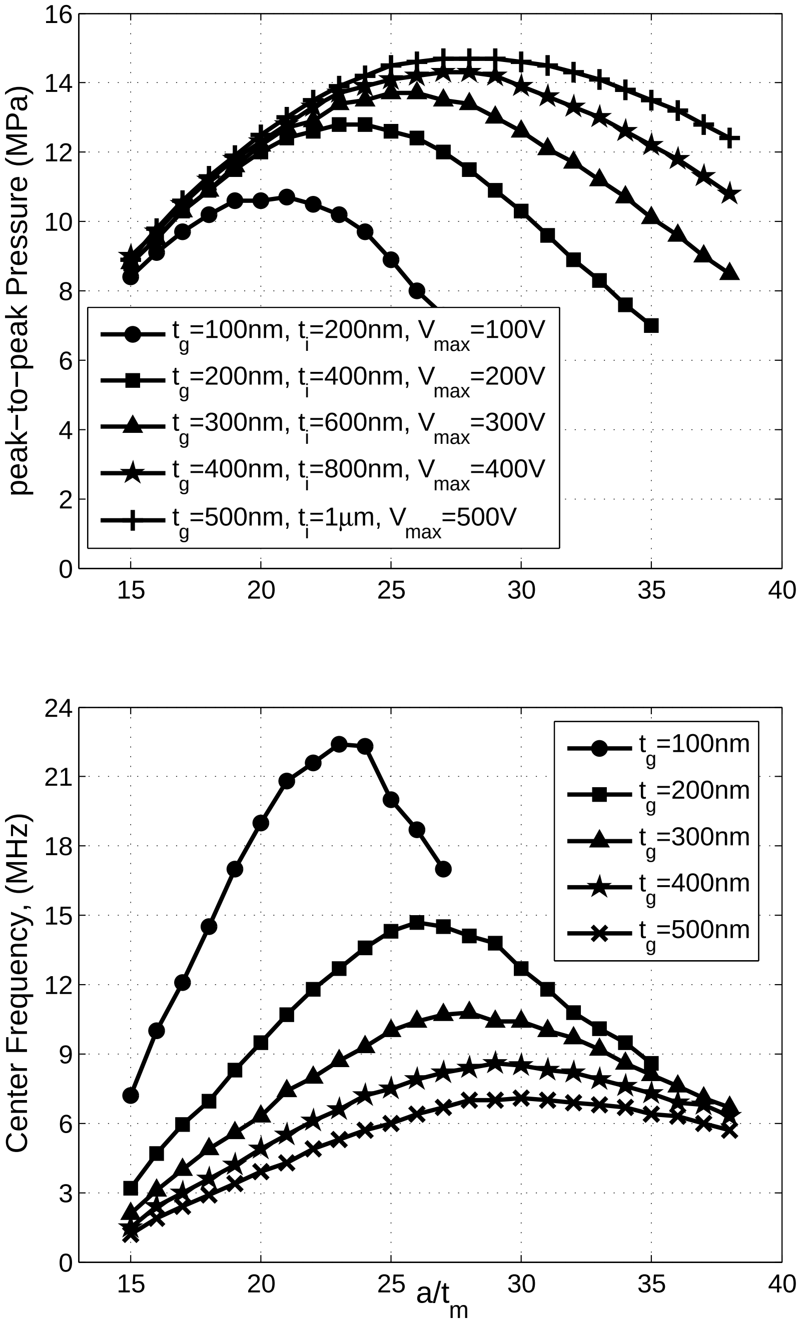

Figure 5.18: Peak-to-peak amplitude (top) and center frequency (bottom) of the generated pressure pulses by CMUTs when they are excited by different electrical pulses with the optimum pulse width as a function of membrane dimensions. The γ value is kept constant and 10 for all CMUT membranes.

A similar trade off between the pressure amplitude and the center frequency can be achieved by changing the maximum available voltage, V_{max}. Acoustic pulses with lower center frequencies are achieved by decreasing the voltage, however the pressure amplitude drops dramatically in this case. Increasing the gap height for decreasing the center frequency of the pulse is a better approach. Therefore it is best to use higher voltages for high pressure outputs and larger gaps for lower frequency pulses.

One may require high amplitude acoustic pulses with low center frequencies. Then maximum available voltage and the gap height should be increased at the same time. In Fig. 5.18, pressure amplitude and center frequency of the generated pulses are depicted when gap height and pulse amplitudes are increased together. This way it is possible to maintain high acoustic pressures for lower frequencies at the expense of high voltages. These designs, however, would require thick insulation layers or materials with higher dielectric breakdown.

5.9 Design Examples

The parameters discussed in this chapter for achieving a high pressure output from CMUT cells with a specified frequency band can be best understood by the use of design examples. This way a method is carried out for designing the dimensions and electrical signals to be applied for specific electrical and acoustical requirements.

As a first example, suppose that there is a need of a pressure pulse signal with as high as possible amplitude with a spectrum around 10 MHz using an electrical excitation with a maximum amplitude of 100V. The rise and fall times of applied electrical pulse should be as fast as possible for higher output pressures as discussed in Section 5.4. For this specific example, rise and fall times of the electrical pulse are selected as 10 ns. We chose to use a positive polarity electrical pulse in order to generate a collapse-release cycle. A full electrode coverage for both top and bottom electrodes is needed for maximum pressure output.

The maximum voltage to be applied across the electrodes is limited by the requirements and is equal to 100V. So, the insulation layer's thickness is determined

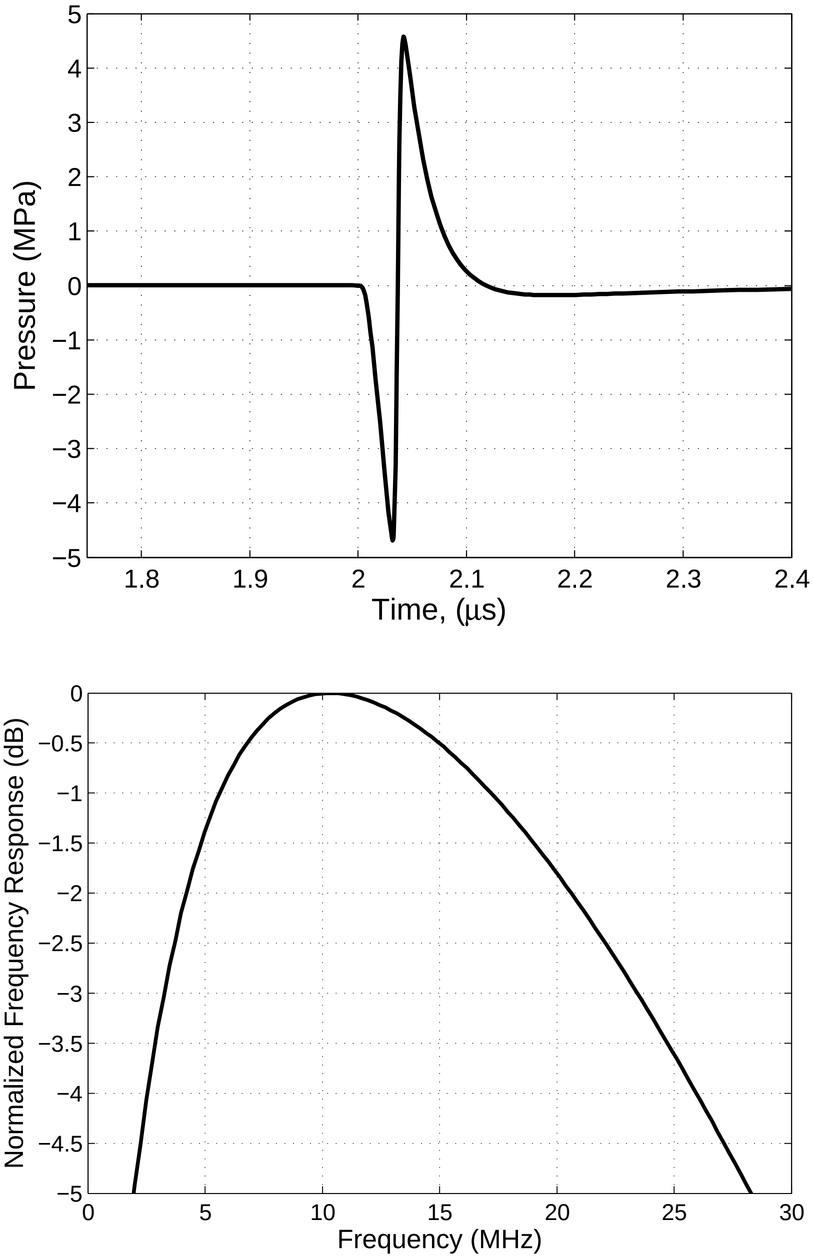

Figure 5.19: Simulated acoustic pulse (top) and its spectrum (bottom) by the designed CMUT with dimensions: $a = 81\mu$m, $t_m = 5\mu$m, $t_g = 0.1\mu$m, $t_i = 0.2\mu$m. The electrical excitation is a 100V pulse with 22 ns pulse width; and 10ns rise and fall times.

to be 200 nm. This thickness would be enough to withstand 100V electric potential.

After determining the insulation layer's thickness, the gap height of the membrane for achieving the high pressure output at the desired frequency spectrum should be chosen. Using Fig. 5.14 it is seen that 200 nm of gap is too large for achieving 10 MHz center frequency. Choosing smaller gaps increases the electrical forces acting on the membrane and in return increases the pressure output. Therefore for this specific example the gap height is chosen to be 100 nm.

Using the top plot in Figs. 5.12 and 5.14 the a/tm ratio is chosen to be equal to 16. Using the same plots, it is seen that; in order to achieve a center frequency of 10 MHz and maintain high pressure amplitude; the γ parameter should be 13. Therefore, the collapse voltage of the membrane should be 7.6V since V_{max} is 100V. A membrane with the a/tm ratio of 15 and the collapse voltage of 7.6V must be 5 μm thick and have a 81 μm microns radius.

Finally, the optimum pulse width is determined using the equivalent circuit simulation. For this particular example, the optimum pulse width is found to be 22 ns. In Fig. 5.19 simulated acoustic pulse (top) and its frequency response (bottom) are depicted. It is seen that the designed CMUT transducer is capable of transmitting acoustic pulses with a peak-to-peak amplitude close to 10 MPa, and a spectrum around 10 MHz as required using an electrical pulse with 100 V amplitude.

As a second example, suppose that there is a need of a pressure pulse signal with an amplitude as high as possible and a spectrum around 25 MHz, using an electrical excitation with a maximum amplitude of 100V. Similar to the previous design example, rise and fall times of the pulse are chosen to be 10 ns for the 100 V pulse. V_{max} of 100 V and the breakdown field determines the insulation layer thickness to be 200 nm.

The gap height of the membrane should be chosen next, for achieving the desired frequency spectrum. Using Fig. 5.14 it is seen that 100 nm of gap is too large for achieving 25 MHz center frequency at 100V. Choosing a smaller gap, increases the electrical forces acting on the membrane and in return increases the center frequency and the pressure output. For this example, the gap height is chosen to be 70nm.

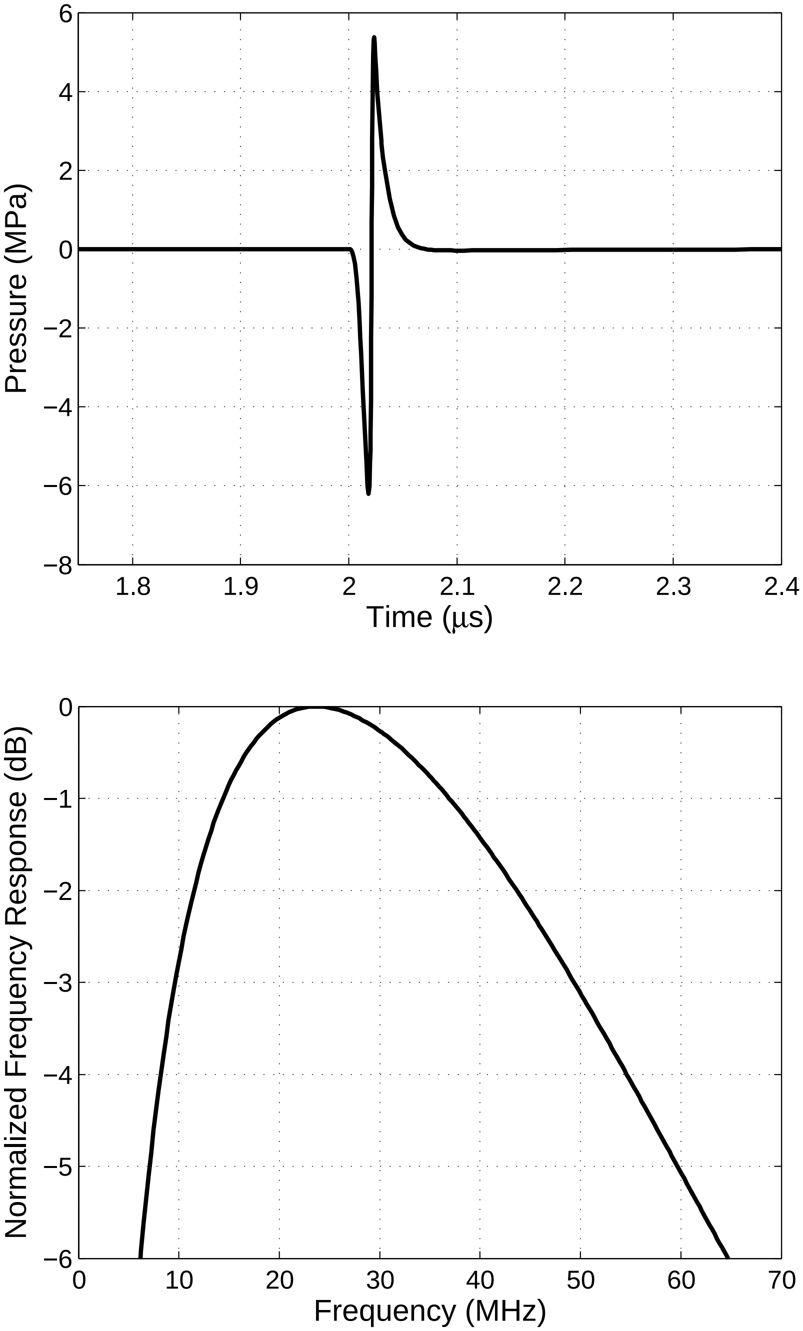

Figure 5.20: Simulated acoustic pulse (top) and its spectrum (bottom) by the designed CMUT with dimensions: $a = 42\mu$m, $t_m = 2.3\mu$m, $t_g = 70$nm, $t_i = 0.2\mu$m. The electrical excitation is a 100V pulse with 10 ns pulse width; and 10ns rise and fall times.

Using Figs. 5.12 and 5.14, a/tm ratio is chosen approximately 18. Using the same figures, it is seen that; in order to achieve a center frequency of 25 MHz and maintain high pressure amplitude; γ should be around 15. Therefore the collapse voltage of the membrane should be 6.7 V. For achieving this collapse voltage and a/tm to be 18, the membrane must be 2.3 μm thick and has 42 μm radius.

Finally, the optimum pulse width is determined using the equivalent circuit simulation. For this particular example, the optimum pulse width is found to be 10 ns. In Fig. 5.20 simulated acoustic pulse (top) and its frequency response (bottom) are depicted. It is seen that the designed CMUT transducer is capable of transmitting acoustic pulses with a peak-to-peak amplitude close to 11 MPa, and a spectrum around 24 MHz as required.

5.10 Experiments

For testing the deep collapse operation, 40 ns pulses with different negative amplitudes are applied to the CMUTs. The applied bias voltage is changed and the negative pulse amplitude is always kept equal to the DC bias. For example, in the case of 160 Volts of bias, a pulse with negative amplitude pulls the bias to 0 for 40 ns and brings back to 160 Volts. Transmitted peak-to-peak pressure values are measured and plotted as a function of the applied pulse amplitude in Fig. 5.21.

Increasing the delivered energy may improve the power delivered to the medium, but there is no simple relation between them. To determine the pressure output theoretically, we need to solve the dynamic problem involving the membrane mass, the radiation impedance of the immersion medium, and the nonlinear spring constant of the membrane excited by a position dependant force as in the case of equivalent circuit simulations. In this chapter we use FEM simulations to handle this nonlinear problem in the time domain. The results of the simulations are depicted in Fig. 5.21. In FEM simulations the loading medium is defined as a water column on a rigid baffle. This would model the medium correctly for a CMUT in the center region of a large array. Since the CMUT array in the experiments has a finite size,

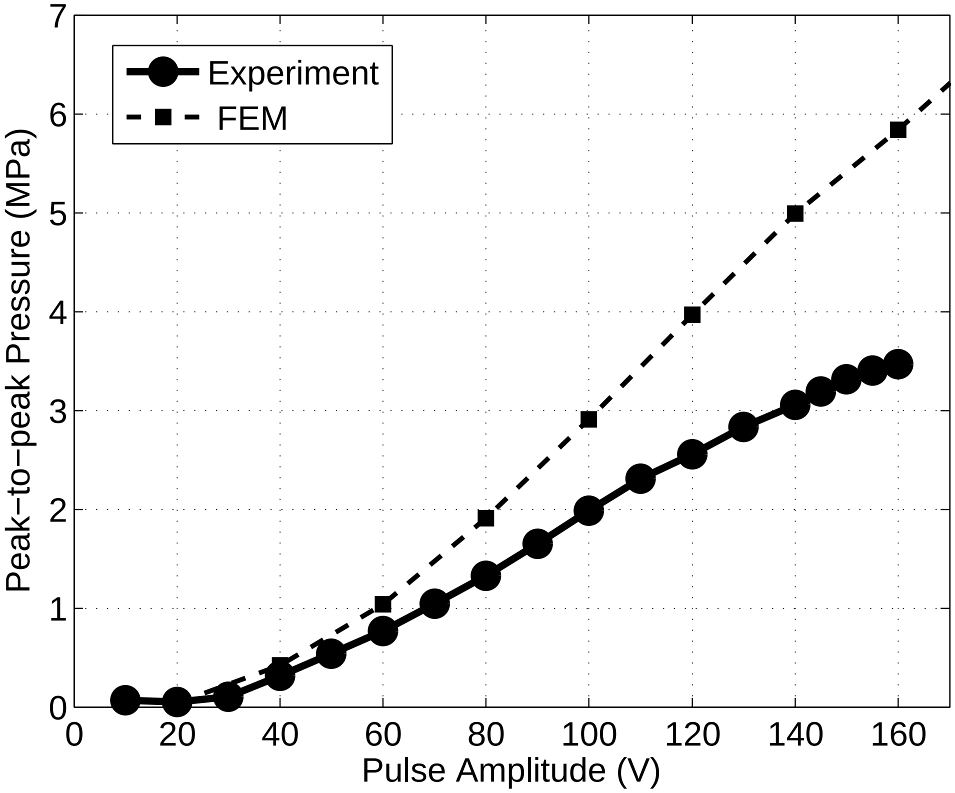

Figure 5.21: Measured peak-to-peak pressure output at the surface of full-electrode CMUTs (solid line) when excited with a pulse of varying negative amplitude on top of an equal amplitude bias. FEM simulation results (dashed lines) are shown for comparison.

the difference between the FEM simulations and the experimental results can be attributed to the inaccurate modeling of the loading effects.

The measured pressure waveform when the CMUTs are excited by negative 160 V pulse on top of 160 V bias is depicted in Fig. 5.22 along with the waveform obtained with FEM simulations. During experiments a peak-to-peak pressure more than 3.5 MPa is measured at the surface of the CMUTs using this excitation. When the membrane is in contact with the substrate, a charge build-up occurs in the insulation layer. The charging phenomenon is a known issue and studied for CMUTs earlier [25, 86–89]. The amount of charge in the insulation layer is determined by applying a bias voltage until the small signal output pressure becomes minimum.

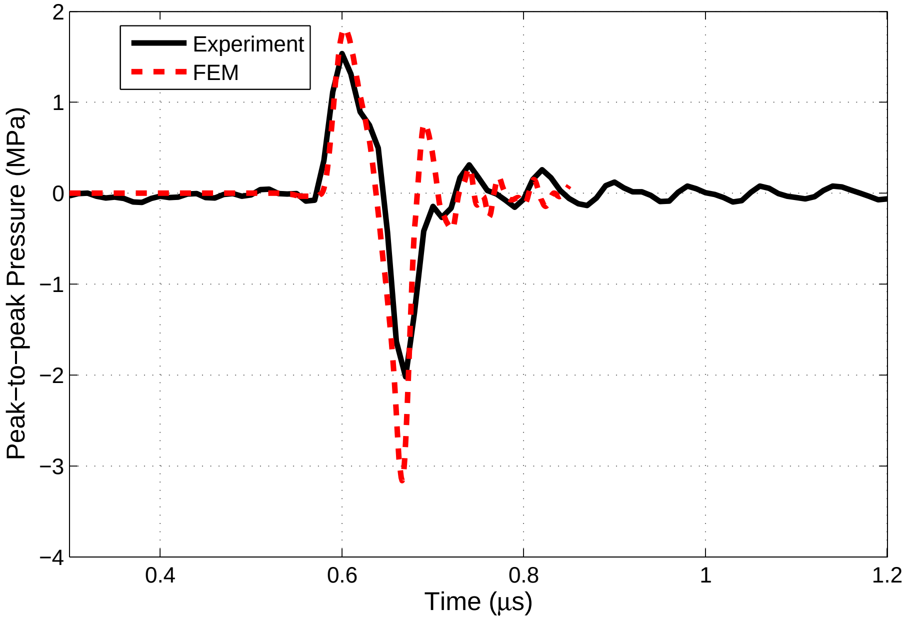

Figure 5.22: Measured (solid) and simulated (dashed) pressure waveforms at the surface of the CMUTs when the transducers are excited with a 40 ns long, negative 160 V pulse on top of 160 V bias. The experiments and simulations are performed on the CMUT with cell dimensions: $a = 30\mu\text{m}$, $t_m = 1.4\mu\text{m}$, $t_g = 0.2\mu\text{m}$, $t_i = 0.4\mu\text{m}$.

This bias voltage is then used as a correction value for the DC bias voltages reported. Pulses with larger amplitudes have not been applied to the CMUTs due to charging and dielectric breakdown considerations. The measured waveform compares well with the FEM and equivalent circuit model simulations.

The positive cycle of the pressure waveform has a smaller amplitude and lasts longer, while the negative cycle is larger in amplitude and faster in the time axis. Transmitted pressure waveform obtained experimentally in Fig. 5.22 has a fractional bandwidth of 106% between 3.2 MHz and 10.4 MHz, which is depicted in Fig. 5.23. Note that the silicon substrate mode at 12.5 MHz is out of the transmission band since the silicon wafer is approximately 330 μm in thickness.

The calculated electrical and restoring force curves indicate that higher voltages maintain higher forces acting on the membrane for both the collapse and release parts of a unipolar pulse cycle (see Fig. 5.1). During a release/collapse pulse cycle, first the stored mechanical energy is radiated into the medium as a positive pressure

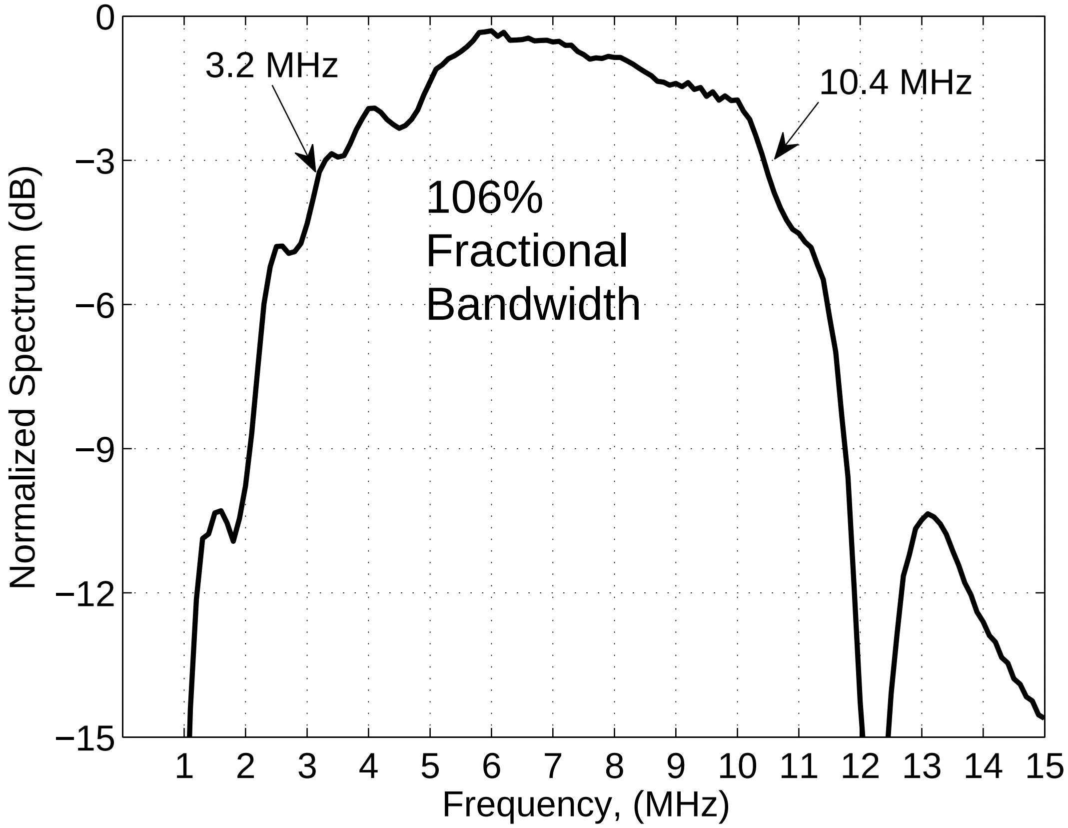

Figure 5.23: Normalized transmission spectrum of the waveform in Fig. 5.22 generated en excited with 40 ns long, -160 V pulse on top of 160 V bias.

waveform followed by a negative pressure. The dynamics of a membrane during such an excitation is discussed in Section 5.6. As discussed, the ringing following the pressure waveform is observed in the circuit simulations and FEM simulations as seen in Figs. 3.2 and 5.22, respectively. In the experimental results, the ringing of the membrane is harder to identify because of the substrate ringing. But with careful examination two harmonics in the first couple of rings can be identified. The lower frequency oscillation, which lasts longer, is the substrate ringing with ∼80 ns period. The higher frequency oscillation is the membrane ringing, which has ∼40 ns period. Approximately 40 ns ringing period of the membrane measured in the transmitted pressure waveform in Fig. 5.22 is consistent with the FEM result.

Chapter 6

Capacitive Micromachined Underwater Transducers

Applications such as medical imaging, high intensity focussed ultrasound, intravascular ultrasound, airborne acoustics, microphones and nondestructive evaluation attracted attention for possible use of CMUTs. The operational frequency range in focus has been mainly between 1 MHz to 30 MHz. Recently, potential of achieving a large bandwidth and high efficiency from CMUTs attracted more applications at lower frequency bands. Recent studies show that airborne CMUTs can achieve a high transduction efficiency and bandwidth around 50 KHz [48].

Acoustical energy has been used underwater for commercial, scientific and military applications. In lower frequency range (1 kHz – 100 kHz), acoustical systems are utilized underwater and on surface platform applications, i.e., navigation systems, active and passive sonar transducers, seismic and environmental observation systems. In the higher frequency range the applications are more limited due to the higher attenuation underwater, which makes such applications are restricted in short ranges. Most common practices are purse seining, Doppler Sonars and underwater imaging systems.

In underwater acoustic applications, achieving a high acoustical power during the transmit cycle and a high sensitivity during the receive cycle in a large bandwidth is

	t_m (μm)	f_r (kHz)	a (mm)	t_g (μm)	t_i (μm)
A	380	84.9	4	4 – 4.2	0.5
B	380	54.8	5	4 – 4.2	0.5
C	380	38.2	6	4 – 4.2	0.5

Table 6.1: Physical dimensions of underwater CMUTs.

not an easy task. In the case of building an array of transducers, building transmit and receive elements along with the required interconnects to the dedicated transmit and receive circuitry is another challenge. For low frequency applications production of thin transducers is also a difficult task. We believe CMUTs can provide solutions to those problems, since they offer properties such as wide bandwidth, ease of array fabrication and integrating the dedicated electronics along with the transducers, thanks to the microfabrication techniques utilized during fabrication. Recent studies show that high power outputs can be obtained and high receive sensitivities can be achieved using CMUTs. CMUT's large bandwidth, high sensitivity, low cost fabrication and ease of integration with electronics make it a good candidate for an underwater transducer. However, extra care should be exercised in order to utilize the full merit of the CMUTs. Especially, nonlinear behavior during transmit mode should be taken into account.

6.1 Designing an Uncollapsed Mode Underwater Transducer

We have designed, fabricated and tested CMUTs as underwater transducers. Single CMUT membranes with three different radii and 380 μm of thickness are fabricated for the demonstration of an underwater CMUT cell. The results of the underwater measurements are reported and compared with those obtained from an equivalent circuit model.

In principle, CMUTs work with a fixed DC bias generating a static force deflecting the membrane. Therefore, any external static force changes the operating point of the device. Underwater hydrostatic pressure affects the operation of the CMUT

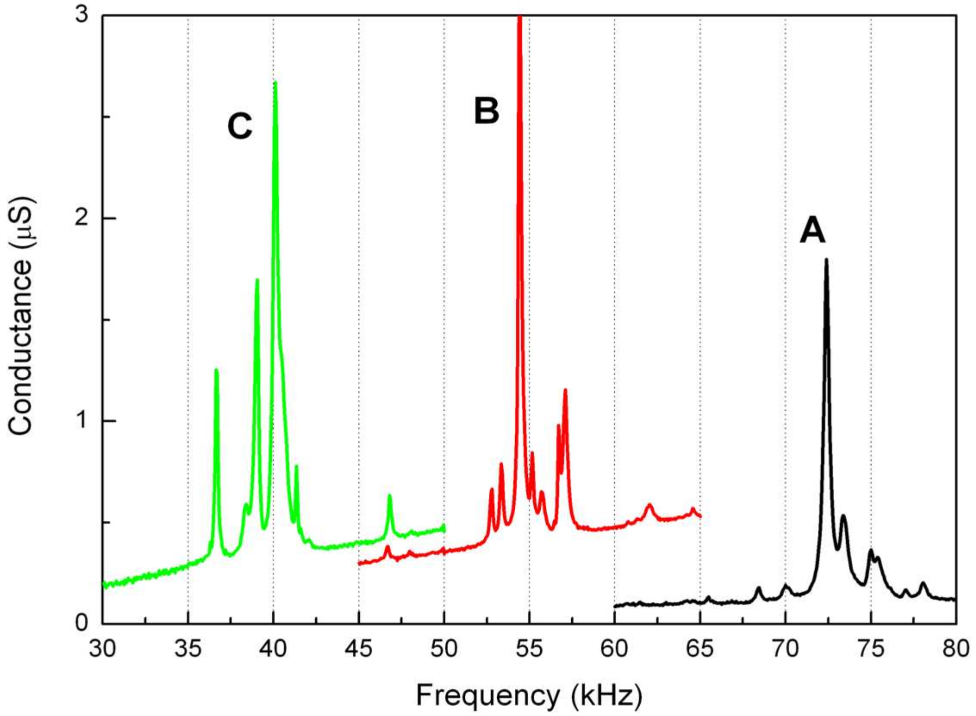

Figure 6.1: Conductance graphs of single cell CMUTs as calculated using the equivalent circuit simulations for CMUT dimensions given in Table 6.1.

membranes. In this study, we limit ourselves to the design CMUTs operating at a depth of 0-2 m. We have designed three different sized CMUT cells (A, B and C) for operation underwater. The gap height of the transducers is chosen in order to achieve a reasonable operating voltage under 250 V for cell B. A highly doped, low resistivity silicon wafer is used as the membrane. A thermally grown silicon dioxide layer is used as the insulation layer between top and bottom electrodes of the CMUT. The insulation layer should be thick enough, in order to prevent an electrical breakdown. The dielectric strength of the thermally grown oxide is typically ∼1000 V/ μm. The thickness of the isolation layer is chosen to be 500 nm in order to maintain 250 V of operation voltage. The physical parameters of the designed CMUT cells can be seen in Table 6.1, where f_r is the airborne resonance frequency of the membrane.

The conductance graphs of the single cell CMUTs are calculated using the equivalent circuit model developed in [57]. Each cell is simulated by applying 100 V peak-to-peak sinusoid on 50 V DC bias. The conductance curves are calculated by

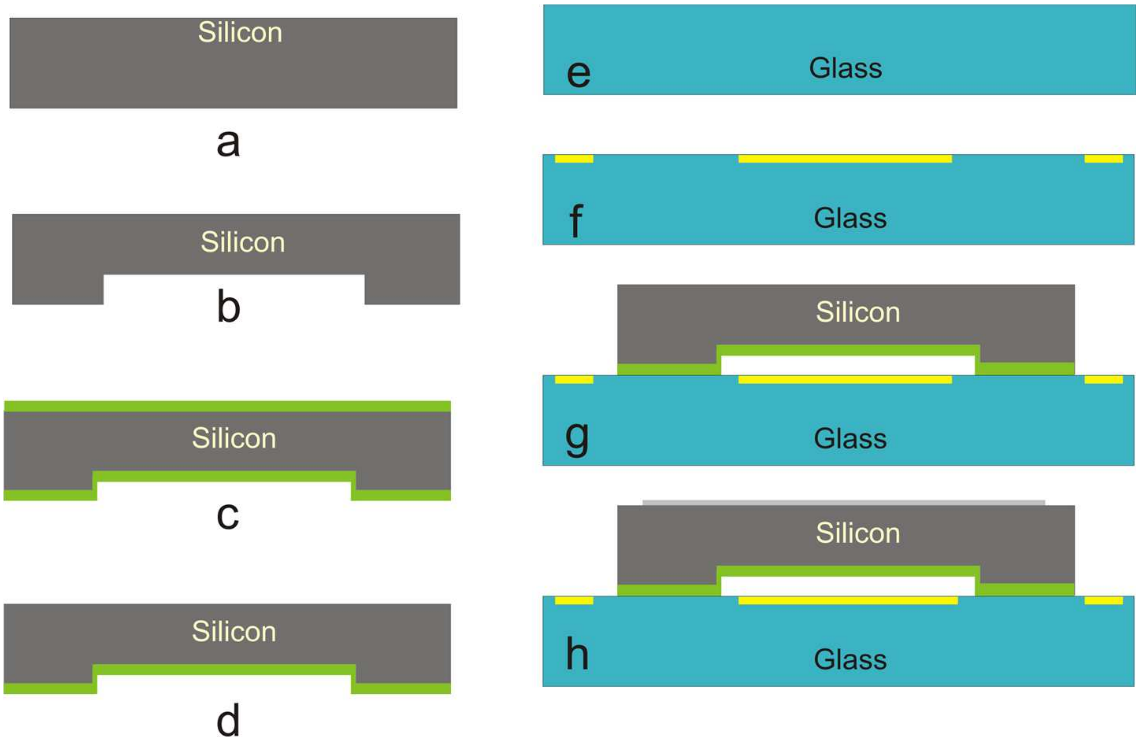

Figure 6.2: Fabrication flow of underwater CMUTs performed at Bilkent University, using an anodic wafer bonding technology.

taking the ratio of the current and voltage of the driving source. In addition to the single cell CMUTs, we have designed an array consisting of B type cells. We have packed a total of 26 cells on a 3" silicon wafer.

6.2 Fabrication

For the fabrication of the underwater CMUT transducers, we have utilized anodic wafer bonding technology. Anodic bonding is used to bond a silicon wafer to a borosilicate wafer using proper pressure, electric field and temperature. A borosilicate wafer has mobile ions at the bonding temperature in order to maintain the migration of ions and formation of a depletion layer at the interface. In this work we have used commercially available Borofloat wafers[1].

---

[1] Silicon Quest International Inc, CA, USA.

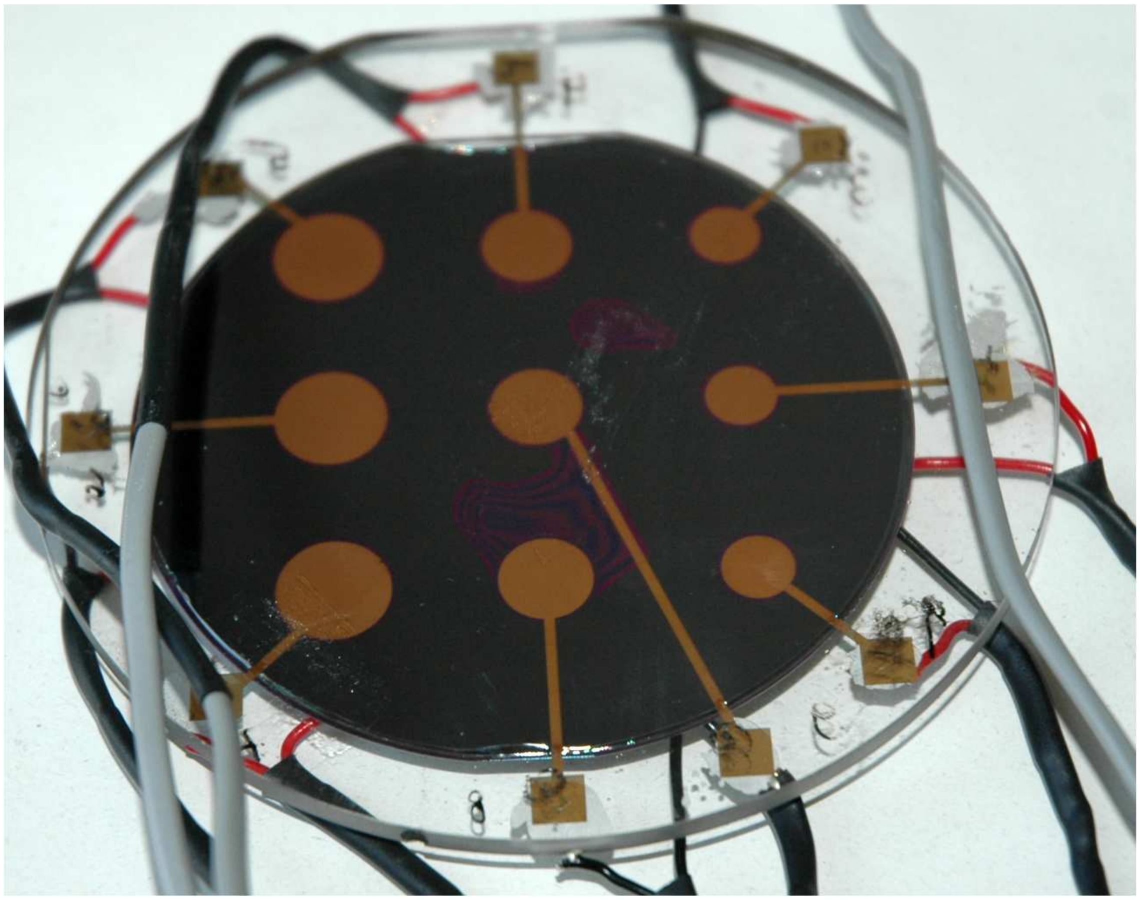

Figure 6.3: A photograph of the transducers after wafer bonding and electrical contacts are made. Single cell CMUTs (A, B and C) with three different sizes are seen.

A highly doped, double side polished silicon wafer is used at the membrane side. The thickness of the wafer determines the thickness of the membrane which is 380 μm in this case (Fig. 6.2a). First, a gap underneath the membrane of 4.5 μm is etched using a RIE reactor (Fig. 6.2b). A 250 nm of chromium layer is used as the etch mask during the RIE process. For passivation of the silicon surface 500 nm of silicon dioxide is thermally grown in a diffusion furnace. The silicon wafer is kept in the furnace at 1050°C for 1 hour in the presence of adequate water vapor (Fig. 6.2c). The silicon dioxide at the back side of the silicon wafer is etched using the RIE reactor (Fig. 6.2d).

Having completed the membrane side, the substrate side is fabricated on a 3.2 mm thick borosilicate wafer (Fig. 6.2e). This wafer is chosen to be quite thick in

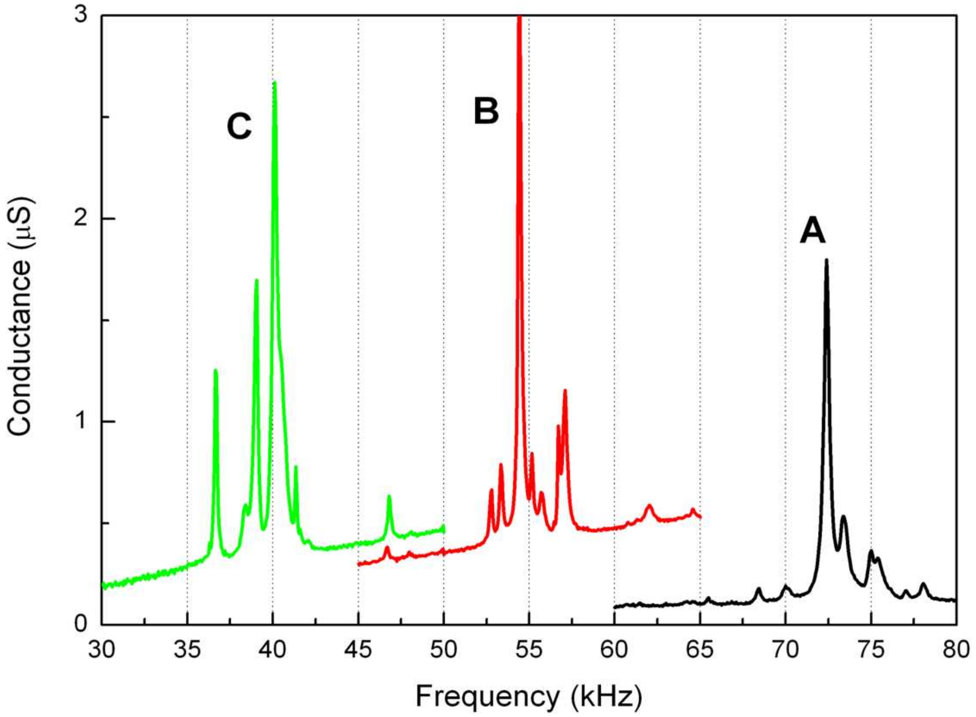

Figure 6.4: Conductances of the CMUT cells A, B and C measured by an impedance analyzer (HP4194A). The measurements are made with 40 V DC and 1 V peak-to-peak AC voltage.

order to maintain a rigid substrate. Since the smoothness of the borosilicate surface is critical for the success of the anodic bonding, the substrate electrode is buried on the glass wafer (Fig. 6.2f). An image reversal photoresist (AZ5214E) is patterned for the lift off process. Before the evaporation of the gold electrode, the glass is etched approximately by the thickness of gold to be evaporated. As the substrate electrode, 5 nm of chromium and 45 nm of gold are deposited by thermal evaporation. The borosilicate and silicon wafers are cleaned in Piranha solution for 15 minutes.

The prepared wafers are then bonded in a commercially available bonding facility[2] using their anodic bonding process (Fig.6.2g). The process has been performed at 450°C at an ambient pressure of 0.1 μbar. 1000 V has been utilized as the bonding voltage.

---

[2] Applied Microengineering Ltd., Oxfordshire, UK.

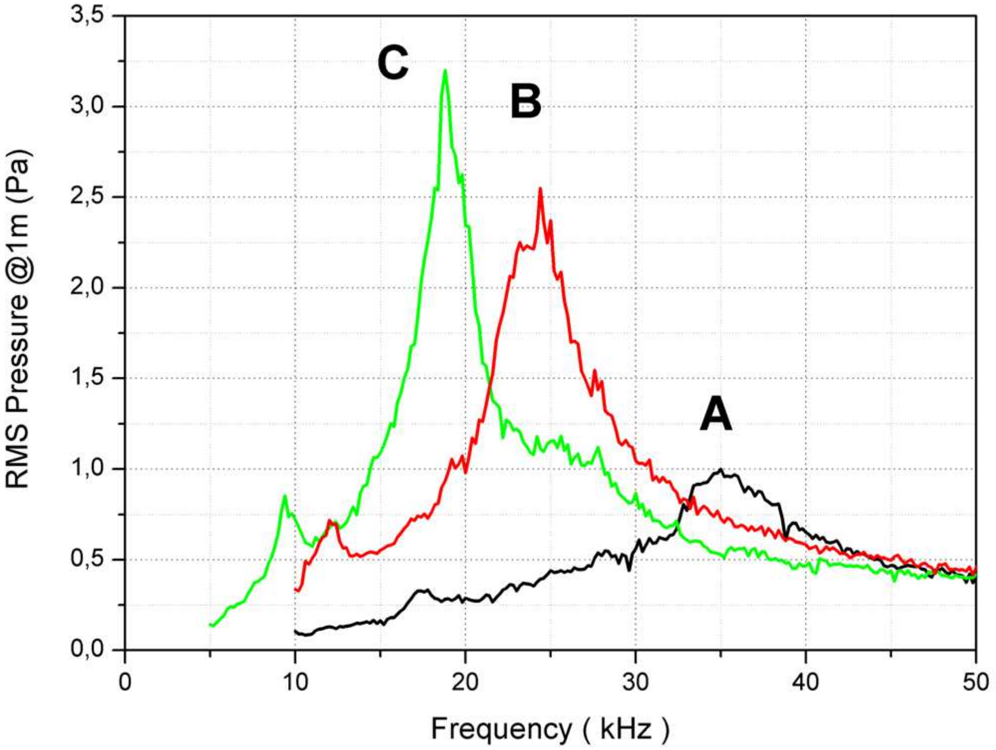

Figure 6.5: Absolute rms pressure spectra of the CMUTs A, B and C at 1 m. The results are not compensated for the diffraction losses.

Since the borosilicate wafer is larger than the silicon wafer, the substrate electrical contacts are taken from the exposed surface of the borosilicate wafer. For the top electrode of the CMUT, an aluminum layer is evaporated on top of the silicon membrane after the bonding process (Fig. 6.2h).

Although anodic bonding is a mature technology and already used in a large variety of industrial products, there are still several aspects which should be investigated [90]. It has been mentioned in the literature that suspended structures tend to stick to the glass wafer due to the applied bonding voltage [91]. In the case of CMUTs, collapse of the membrane is prevented by limiting the bonding current in order to maintain a voltage smaller than the collapse voltage across the CMUT cavity. Using limited bonding current and thin metal layers improved the bonding area and quality.

A photograph of the bonded transducers are seen in Fig. 6.3. Having completed

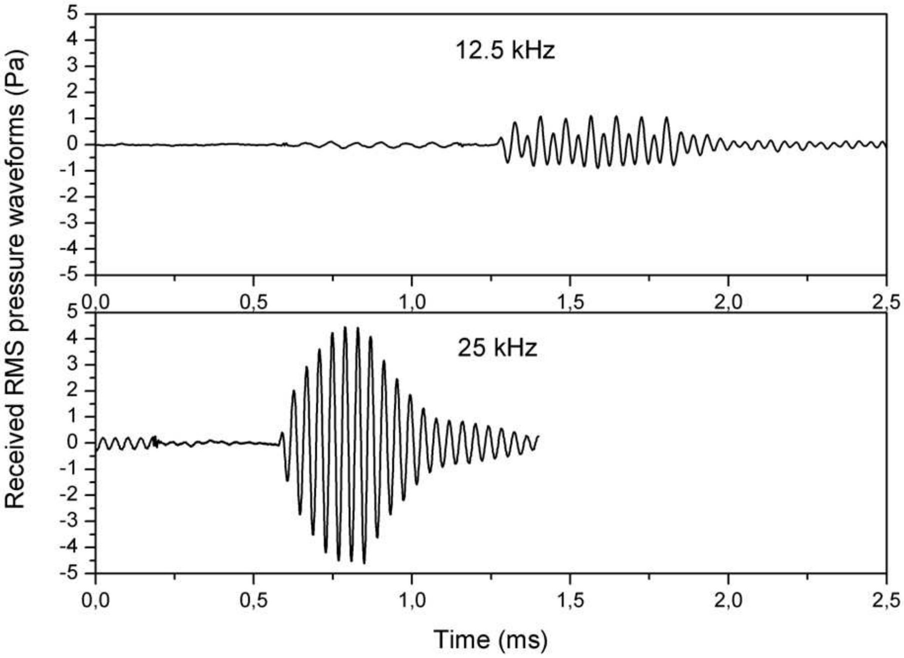

Figure 6.6: Recorded pressure waveforms for the cell B for 100V peak-to-peak sinusoidal burst excitation at 12.5 kHz and 25 kHz on 50V DC bias.

the microfabrication process steps in cleanroom, electrical contacts to the electrodes are made using a commercially available silver conductive epoxy Eccobond 83C (Emerson-Cuming). The transducers are mounted in a slightly larger holder using Eccobond 45 epoxy (Emerson Cuming). An equal sized 2 mm thick rigid foam disk (Airex) is fixed at the backside. This way the transducer is terminated by a low impedance medium at the backside. After the curing, the exposed region of the aluminum electrode, which is the active area of the transducer is painted in order achieve electrical insulation for immersion experiments.

6.3 Measurements

Fabricated transducers are first tested in air. The conductances of the transducers are measured by an impedance analyzer (HP4194A). The measurements are made

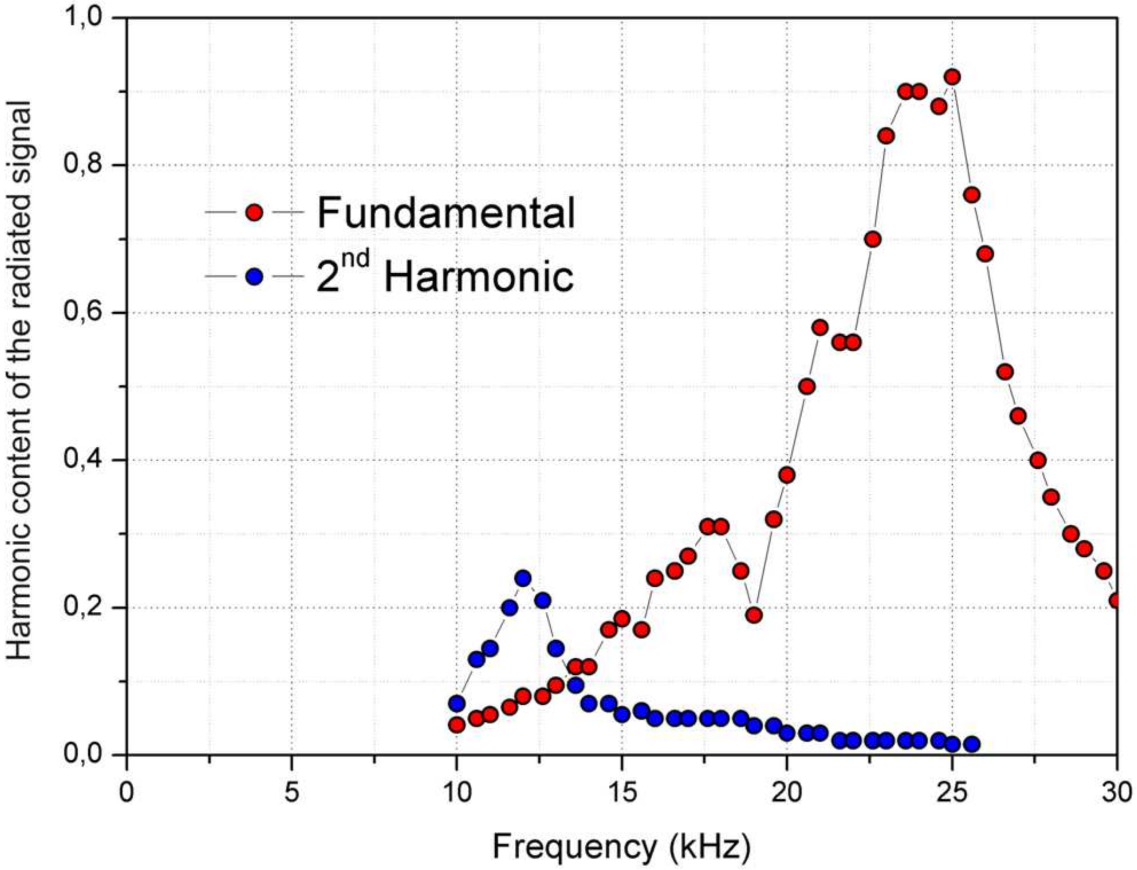

Figure 6.7: Amount of fundamental and second harmonic components at different frequencies for CMUT cell B when it is excited by 100V peak-to-peak sinusoidal burst excitation on 50V DC bias.

with 40 V of bias and 1 V peak-to-peak of AC voltage. The conductances of cells A, B and C are shown in Fig. 6.4.

The details of the experimental setup for the underwater measurements are given in Appendix B. The amplitude of the applied signal is kept at 100 V peak-to-peak. A 50 V DC bias voltage is applied in order to keep the excitation unipolar. The absolute rms pressure spectra of the CMUTs at 1 m are depicted in Fig. 6.5 The results are not compensated for the diffraction loss and given as normalized to radiation at 1 m. The differences at the peak pressures of different CMUTs can be attributed to differences in collapse voltages. Approximately, a 40% bandwidth is achieved from the cell type B.

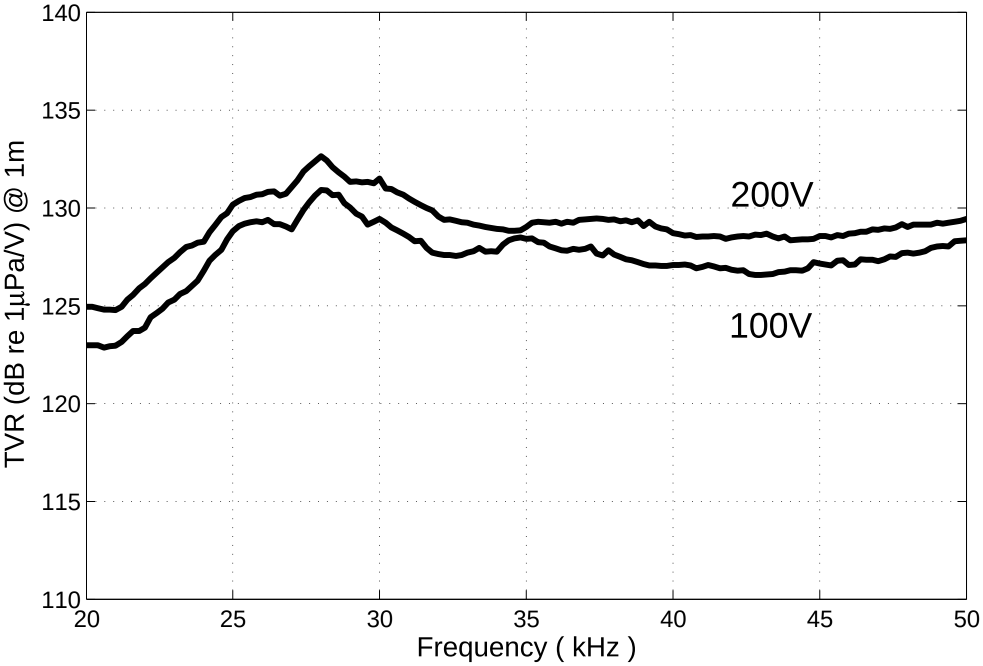

Figure 6.8: Transmitting voltage response (TVR) of a CMUT array of cell type B for 100V and 200V sinusoidal burst excitation on 50V and 100V DC bias, respectively.

Similarly, an array of type B cells has been tested both in air and underwater. Airborne impedance measurements indicate too many unaccounted resonances. Nevertheless, when immersed, we were able to achieve 300 Pa rms pressure at 1 m away from the CMUTs with 100 V peak-to-peak excitation.

During the immersion experiments of cells A, B and C, we have observed small peaks at the half of the resonance frequency as seen in Fig. 6.5. These peaks are attributed to nonlinear behavior of CMUTs. The recorded pressure waveforms are depicted in Fig. 6.6 for the cell B at 12.5 kHz and 25 kHz. As can be seen in the waveforms, the radiation in the case of 12.5 kHz excitation has a strong component at 25 kHz. That is because the second harmonic of the 12.5 kHz excitation coincides with the resonance frequency of the cell. In Fig. 6.7, we show the amount of fundamental and second harmonic components at different frequencies. The second harmonic component becomes significant only when that frequency is around the resonance of the cell. These small peaks at half the resonance are also observed in our equivalent circuit simulations results shown in Fig. 6.1.

We have fabricated and tested underwater CMUT transducers. The radiation impedance seen by a single cell is lower than that seen by an array of CMUT cells. Therefore, the bandwidth of an underwater CMUT array would be larger than the bandwidths presented. It has been demonstrated that operation of CMUTs as underwater acoustic transducers is possible and needs further investigation for optimal use.

6.4 A Deep Collapse Mode Design Example

In addition to the previous discussion about capacitive micromachined underwater transducers, deep collapse mode operation can be utilized for generating a high power, high bandwidth pulse from an underwater CMUT. Such a high intensity, high bandwidth pulse is required for echo-sounders and underwater acoustic imaging.

As a design example, we assume that the required pulse should have a center frequency of 100kHz. Available voltage for the driving circuitry is limited to 500 V. So, the insulation layer's thickness is determined to be 1μm, which would be enough to withstand the maximum field.

After determining the insulation layer's thickness, the gap height of the membrane for achieving the high pressure output at the desired frequency spectrum should be chosen. Referring to the discussion in Chapter 5, we should use a large gap height in order to provide the low frequency operation. In this particular design, we choose 3 μm as the gap height.

For achieving the deep collapse mode for high intensity acoustic pulses, we choose the parameter γ as 5. Therefore the collapse voltage of the CMUTs should be around 100V. After a few iterations using the equivalent circuit, we see that the required a/t_m ratio for this application is 18. Therefore, we calculate the dimensions of the membrane as 1.4mm radius, 75μm thickness.

Finally, the optimum pulse width is determined using the equivalent circuit simulation. For this particular example, the optimum pulse width is found to be 4.8 μm.

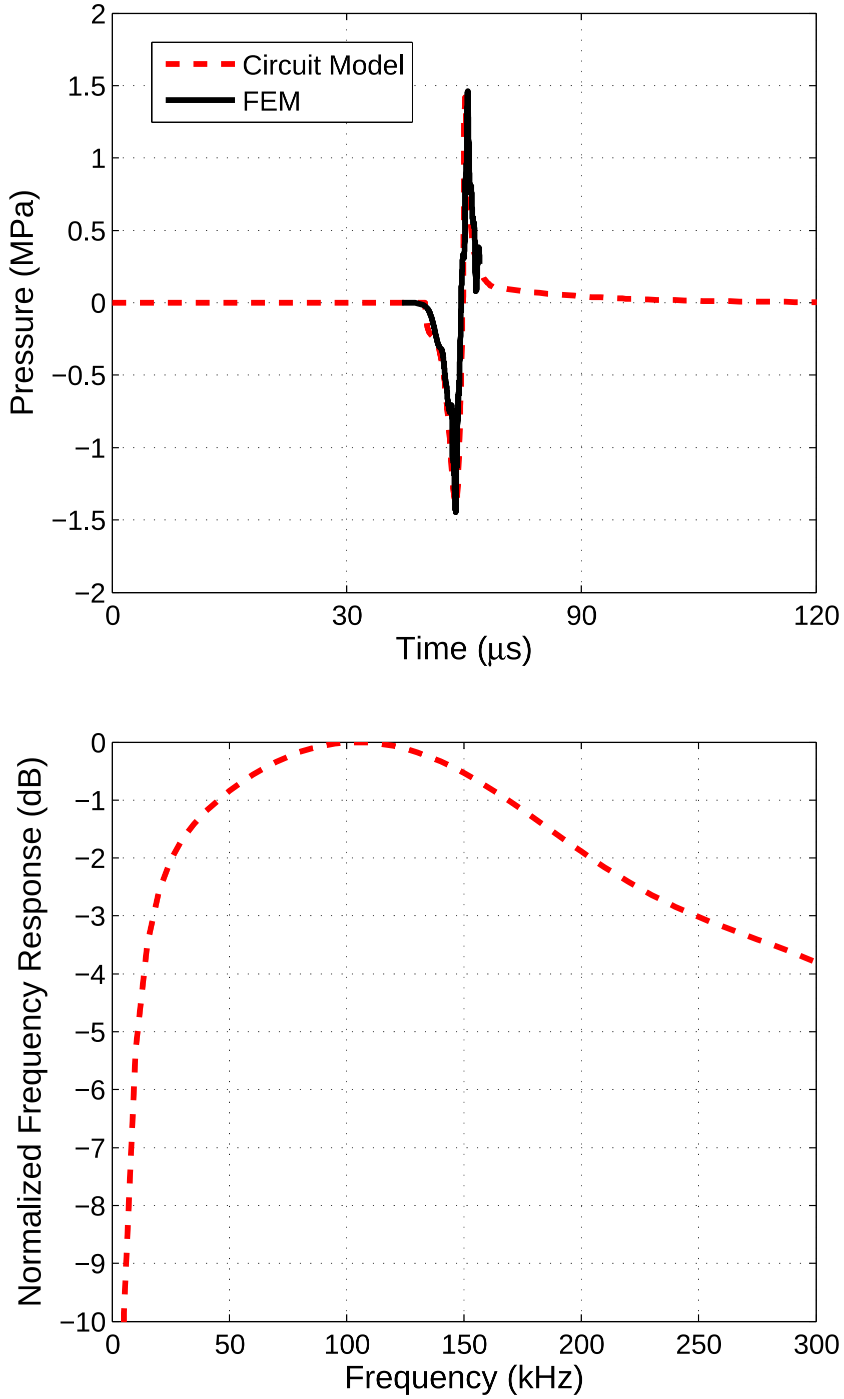

Figure 6.9: Transient FEM and equivalent circuit simulations for the acoustic pulse (top) and its spectrum (bottom) generated by the designed CMUT with dimensions: a=1.4mm, t_m=75μm, t_g=3μm, t_i=1μm. The electrical excitation is a 500V pulse with 4.8μs pulse width.

In Fig. 6.9 simulated acoustic pulse (top) and its frequency response (bottom) are depicted. The results of the equivalent circuit simulations are verified with transient FEM simulations performed on identical CMUTs and electrical excitations. The good agreement between the FEM and the circuit simulation show that the designed underwater CMUT is capable of transmitting acoustic pulses with a peak-to-peak amplitude close to 3 MPa, and a spectrum around 100 kHz as required using an electrical pulse with 500 V amplitude.

Chapter 7

Conclusions

This thesis focuses on the dynamic behavior of CMUT membranes both in the conventional uncollapsed and collapsed states. The major purpose for understanding the physics of membrane movement is to increase the power output capability of CMUTs. In terms of performance, the limited power output capability of CMUTs was their major drawback as compared to their piezoelectric rivals.

The static deflection profile of a membrane is the fundamental measure of a CMUT under any external excitation. In this thesis, we derive the analytical expressions of the membrane displacement as a function of uniform pressure excitation for both an uncollapsed and a collapsed circular clamped membrane. The analytical expressions and FEM simulation results fits perfectly. The deflection by an electrical excitation, on the other hand, is given by a simple numerical approach where electrical and mechanical forces work against each other. Forces acting on a CMUT membrane are given as a function of a lumped membrane displacement for both uncollapsed and collapsed states. The results of the numerical calculations and FEM simulation results for electrostatic deflection of a membrane are in good agreement with 1% of error. The deflection profile in the collapsed state and hysteretic snap-back behavior of CMUTs are predicted for the first time other than FEM simulations by our numerical approach.

We demonstrate that the energy stored and radiated by a CMUT membrane increase drastically when it is in the collapsed state due to the nonlinear behavior of the forces. We propose a new operation regime, the deep collapse mode, where highly nonlinear forces are utilized during the transmission cycle, well beyond the collapse point. In order to understand the dynamics of this mode, we have developed a parametric equivalent circuit model for CMUTs and implemented a non-linear circuit using LTSpice. Exact analytical equations are used to determine the relation between the deflection of a CMUT membrane and the forces acting on the membrane. The equivalent circuit includes the effects of membrane mass and the loading of the immersion medium. The simulation of the equivalent circuit can be completed much faster than FEM simulations, but the results are within 3% of each other. With an arbitrary excitation of CMUT, one can deduce the time waveform of the acoustic signal as well as the instantaneous position of the membrane. The comparison of the results that are acquired from FEM simulations lasting more than an hour to that from LTSpice simulations, which take a few seconds, is astonishing. The equivalent circuit model is a very strong design and simulation tool for CMUTs under any excitation. We note that the accuracy of the equivalent circuit can be improved by adding a more exact radiation impedance model.

Using the equivalent circuit, we determine the effects of the physical and the electrical parameters of a CMUT operation, in order to achieve the maximum pressure output at a desired frequency spectrum. In that sense the effects of the insulation layer, gap height, radius and thickness of the membrane are demonstrated on the output pressure and frequency spectrum of the radiated acoustic pulse. The parameters of the electrical pulse applied to a CMUT in order to achieve a maximum pressure intensity is discussed and clarified. Using the optimization results, design examples are demonstrated.

Furthermore, the deep collapse mode is demonstrated with experiments performed on fabricated CMUTs. The transmitted pressure waveform from a CMUT is recorded by a calibrated hydrophone during the immersion experiments. Utilizing higher restoring and electrical forces in the deep collapse region, we measure 3.5 MPa peak-to-peak pressure with 106% fractional bandwidth at the surface of the transducer when the pulse amplitude is 160 Volts. This pressure output is achieved with a negative pulse generated by a fast transistor in common-source configuration.

The experimental results are compared to dynamic FEM simulations. We conclude that the experimental results are in good agreement with simulations. As discussed, the output pressure of a collapse regime CMUT with full-electrode coverage can be further increased by using pulses with higher amplitudes, faster pulse generators, an optimal pulse shape and higher fill factors. We believe that CMUTs, with their high transmit power capability in a wide band, become a strong competitor to piezoelectrics.

Appendix A

Finite Element Method Simulations

The finite element simulations are done using ANSYS FEM Package (v12.1). A 2-D axisymmetric model of CMUT is utilized. 8-node structural solid (PLANE82) elements are combined with electromechanical transducer elements (TRANS126) under the bottom surface nodes of the membrane. A gap value (*GAP*) and a minimum gap value (*GAPMIN*) are needed to generate ground plane nodes and determine maximum possible deflection before contact. A contact stiffness factor, *FKN*=1 is used to overcome convergence problems with a reasonable penetration at contact interface.

TRANS126 elements do not accept an insulating layer between the electrodes as in the case of CMUTs. Therefore, *GAP* and *GAPMIN* parameters are modified to perform an accurate simulation. The modified parameters are defined as

$$GAP = t'_g = t_g + \frac{t_i}{\epsilon_r} \qquad GAPMIN = \frac{t_i}{\epsilon_r}$$

A static pressure with a value of 100 kPa is applied on all top nodes of the

Young's modulus, E	110 GPa
Poisson's ratio, ν	0.27
Dielectric permittivity, ϵ_r	5.4
Density, ρ	3.1 g/cm^3

Table A.1: Silicon nitride properties used in simulations.

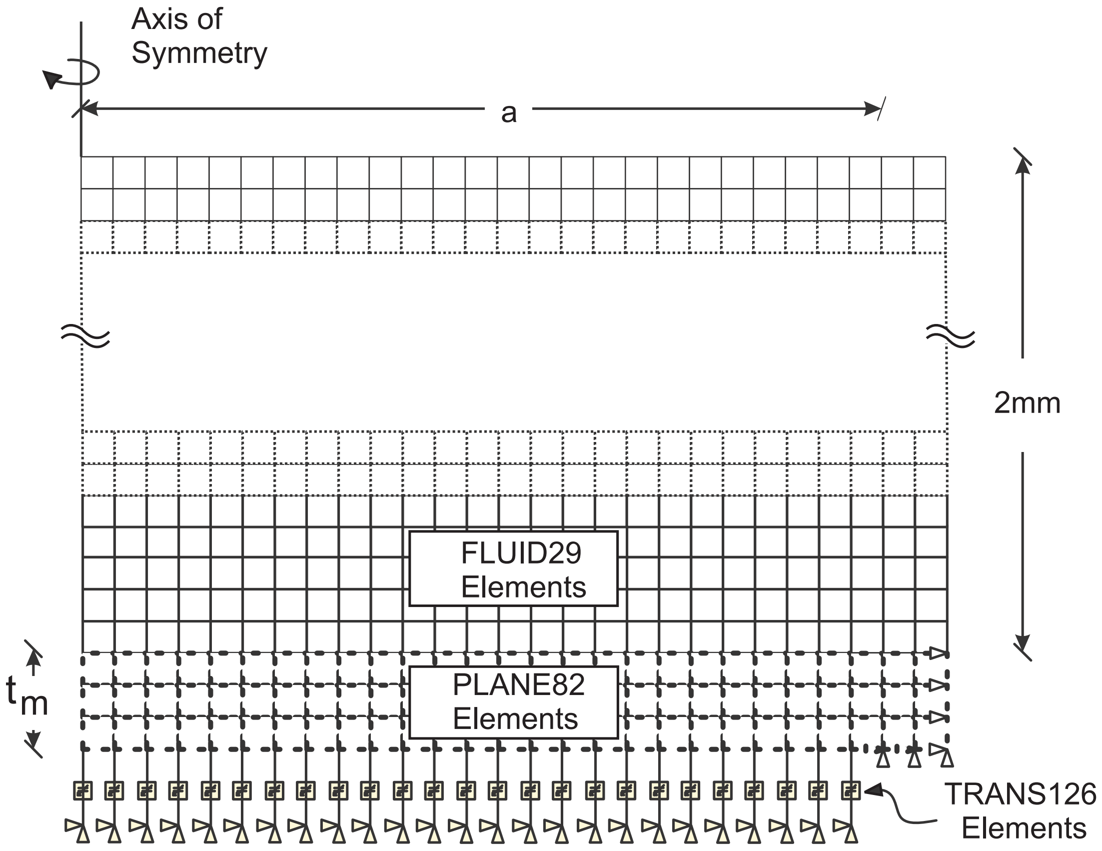

Figure A.1: FEM model used in ANSYS simulations.

membrane in order to include the effect of the atmospheric pressure. A fluid loading is included to the model for simulating the dynamic behavior of the CMUTs. A fluid column of 2 mm height is created over the membrane using 2-D axisymmetric harmonic acoustic fluid (FLUID29) elements. The fluid-structure flags are enabled for coupling the structural motion as an acoustic wave in the medium. In order to ensure the DC stability, the transient effects are turned off in the first step and turned on at the rest of the simulation. The total duration of the simulation is fixed to 1 μsec and average pressure is recorded at 1 mm above the membrane surface.

Appendix B

Experimental Setup

B.1 CMUT IC Handling

Fabricated wafers are dices to 1 cm by 1 cm dies using a Disco DAD3220 Dicing Saw. In order to protect the CMUT dies from the debris of the dicing saw, a thick layer of photoresist is spun on the wafer and hard baked for 10 minutes at 120°C, before the dicing operation.

The die to be tested is removed from the plastic holder and cleaned in acetone bath for 5 minutes in order to get rid of the photoresist laid for protection. Operational dies are determined by testing electrical properties of CMUTs using a custom made probe station and a network analyzer (Agilent E5071C) calibrated at the tip of the probes. A die, if operational, is then placed to a 40-pin ceramic dual-in-line package (CERDIP) chip holder[1] with 1 cm by 1 cm cavity as seen in Fig. B.1. For bonding the CMUT die to the chip holder a commercially available silver conductive epoxy Eccobond 83C (Emerson-Cuming) is used. Since the silicon wafer has a very low conductivity due to its high doping, a ground connection has been made through the back-side of the CMUT die. The ground of the chip holder is later connected to the ground of the measurement system in order to facilitate a good grounding and reduce parasitics effects.

---

[1] Spectrum Semiconductor Materials Inc., San Jose, CA, USA.

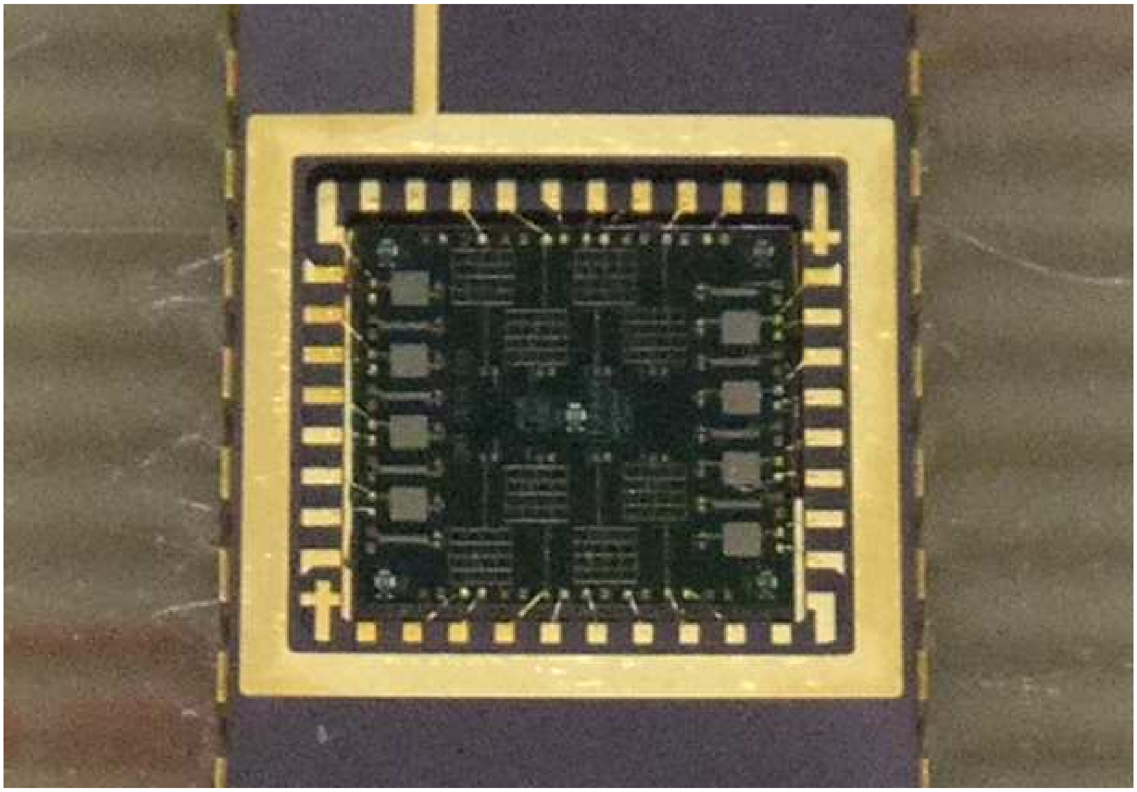

Figure B.1: A CMUT die bonded to a ceramic chip holder before testing. The chip holder is soldered to a PCB for external electrical connections.

Electrical connections between the chip holder and the CMUT die are made using a K&S 4700AD ball/wedge bonder[2]. The ball bond is made on the die side and the wedge bond is placed on the gold coated pad of the chip holder. The chip holder is later solderer to a PCB for external electrical connections.

B.2 Transmit Experiments

Transmit experiments in immersion medium are carried out in a vegetable oil filled tank (see Fig. B.2) using CMUT arrays as the acoustic source and a calibrated hydrophone 1 cm away as the receiver. Vegetable oil has similar mechanical properties to water, and can be used with electrically unisolated CMUTs, since it is a poor conductor of electricity.

---

[2] Kulicke & Soffa Industries, PA, USA.

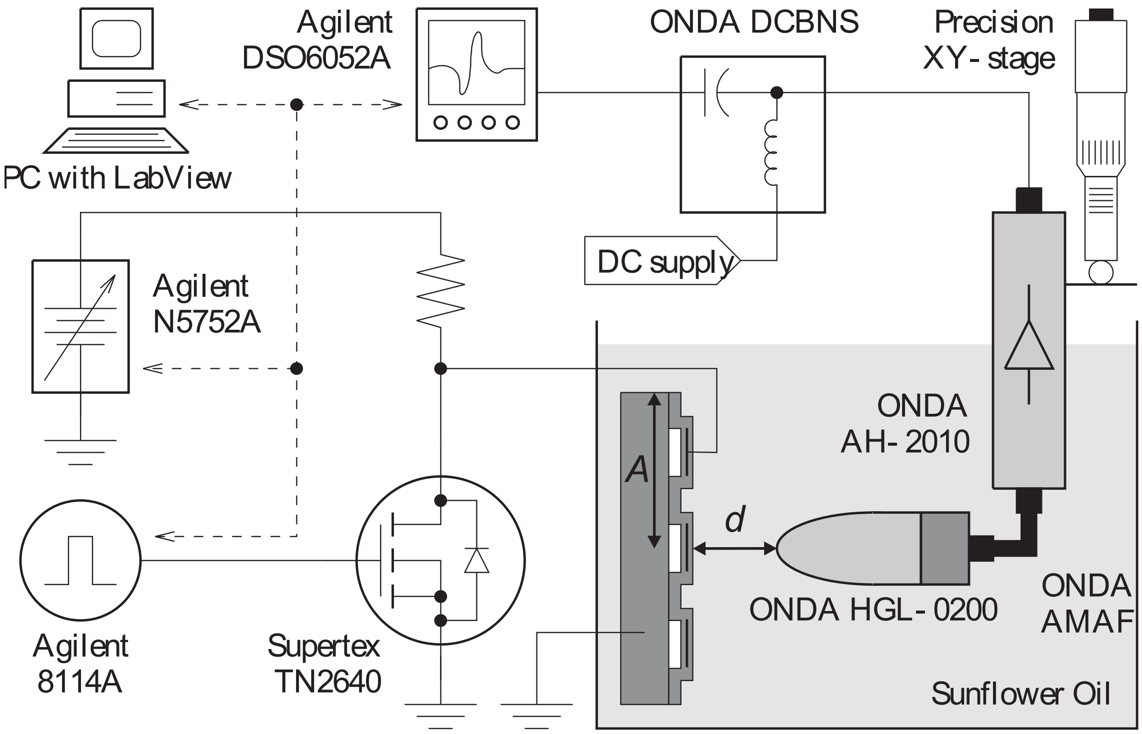

Figure B.2: A schematic of the experimental setup used during the transmission experiments. A calibrated hydrophone (ONDA HGL-0200) with a preamplifier (ONDA AH-2010) is used for recording the transmitted pressure waveform.

The alignment of the hydrophone with respect to the firing CMUT is done by maximizing the received signal amplitude using a precision mechanical stage controlling the position of the hydrophone. The CMUTs are driven with a commercially available pulser (Agilent 8114A) for the small signal experiments and with a fast NMOS transistor (Supertex TN2640) in common source configuration for the large signal experiments. All experiments are performed using a LabView control program. The bias voltage is applied by a DC power supply (Agilent N5752A). For large signal experiments, the control software triggers a pulse applied by the HP8114A to the fast transistor. The amplitude of the applied pulse to the CMUT is controlled by 8114A. Received acoustical signal by the calibrated hydrophone is transferred to an electrical signal and recorded by a digital oscilloscope (Agilent DSO6052A) with 50Ω termination.

B.2.1 Calibration

Pulsed electrical excitations are used in the CMUT transmit experiments, which generate a pulse shaped acoustical waveform. Since the calibration and loss mechanisms are functions of frequency, any corrections and conversions should be performed in the frequency domain and the resulting waveform should then be converted back to a time domain waveform. Therefore we use the fourier transform of the recorded electrical waveform in oscilloscope, $v(t)$:

$$V_r(w) = \mathscr{F}\{v_r(t)\} \qquad \text{(V)} \tag{B.1}$$

The hydrophone is a calibrated receiver. Therefore the received electrical waveform at the oscilloscope can be converted to a pressure waveform as if generated at the CMUT surface by proper conversions and corrections. The conversion from electrical waveform to acoustical waveform requires four correction terms, hydrophone sensitivity, effect of amplifier load and gain, attenuation losses and diffraction losses.

The hydrophone sensitivity, H_S is a function of frequency, ω with the units of V/μPa. The hydrophone, ONDA HGL-0200, is provided with a sensitivity calibration between 1—20 MHz into a 50Ω load. In our experiments we use this hydrophone with a 20 dB preamplifier, ONDA AH-2010. Because a hydrophone's sensitivity depends on the electrical impedance of the detector or amplifier it is attached to, the overall sensitivity should be determined. If the hydrophone and pre-amplifier impedances are primarily capacitive, as in our case, the overall sensitivity of the hydrophone system, H_T is written as follows:

$$H_T(\omega) = G_A(\omega)\, H_S(\omega)\, \frac{C_H}{C_H + C_C + C_A} \qquad \text{(V/Pa)} \tag{B.2}$$

where, G_A is the preamplifier gain, C_H, C_C and C_A are the input capacitances of the hydrophone, connector and preamplifier respectively. The hydrophone is connected to the preamplifier by a right angle SMA connector (ONDA AR-AMAF) with a capacitance of C_C=1.6 pF. The output capacitance of the hydrophone is C_H=10.3 pF and the input capacitance of the preamplifier is C_A=7 pF. Therefore the pressure generated by a CMUT at the location of the hydrophone, $p_h(t)$ is calculated as:

$$p_h(t) = \mathscr{F}^{-1}\{P_h(\omega)\} \qquad \text{(Pa)} \tag{B.3}$$

$$P_h(\omega) = \frac{V_r(\omega)}{H_T(\omega)} \tag{B.4}$$

To find the pressure at the surface of source CMUTs diffraction and attenuation losses are compensated. The diffraction loss of a pressure waveform radiated from a source with a rectangular shape of size, $2A$ by $2A$ is

$$D_L(\omega) = \frac{d}{R_0(\omega)} \tag{B.5}$$

where d is the distance to the source and R_0 is the rayleigh distance of the source, which is given in [92] as:

$$R_0(\omega) = \frac{4A^2}{\lambda} = \frac{4A^2 f}{c_0} = \frac{2A^2\omega}{\pi c} \tag{B.6}$$

Substitution (B.6) to (B.5) the diffraction loss as a function of frequency can be expressed as:

$$D_L(\omega) = \frac{\pi d c}{2A^2\omega} \tag{B.7}$$

The attenuation in the sunflower oil as a function of frequency is calculated using the expressions and constants in [93] as:

$$A_L(\omega) = e^{\alpha d} = e^{A_1(\frac{\omega}{2\pi})^n d} \tag{B.8}$$

where attenuation constant, α is defined in terms of the factors A_1 and n, which are equal to 5.68×10^{12} m^{-1}Hz^{-1} and 1.85, respectively, for sunflower oil. Therefore the pressure waveform generated at the surface of a source CMUT, $p_s(t)$ is calculated in terms of the received electrical waveform, $v(t)$ in (B.1):

$$p_s(t) = \mathscr{F}^{-1}\{P_s(\omega)\} \qquad \text{(Pa)} \tag{B.9}$$

$$P_s(\omega) = P_h(\omega)D_L(\omega)A_L(\omega) = V_r(\omega) \times \frac{D_L(\omega)A_L(\omega)}{H_T(\omega)} \tag{B.10}$$

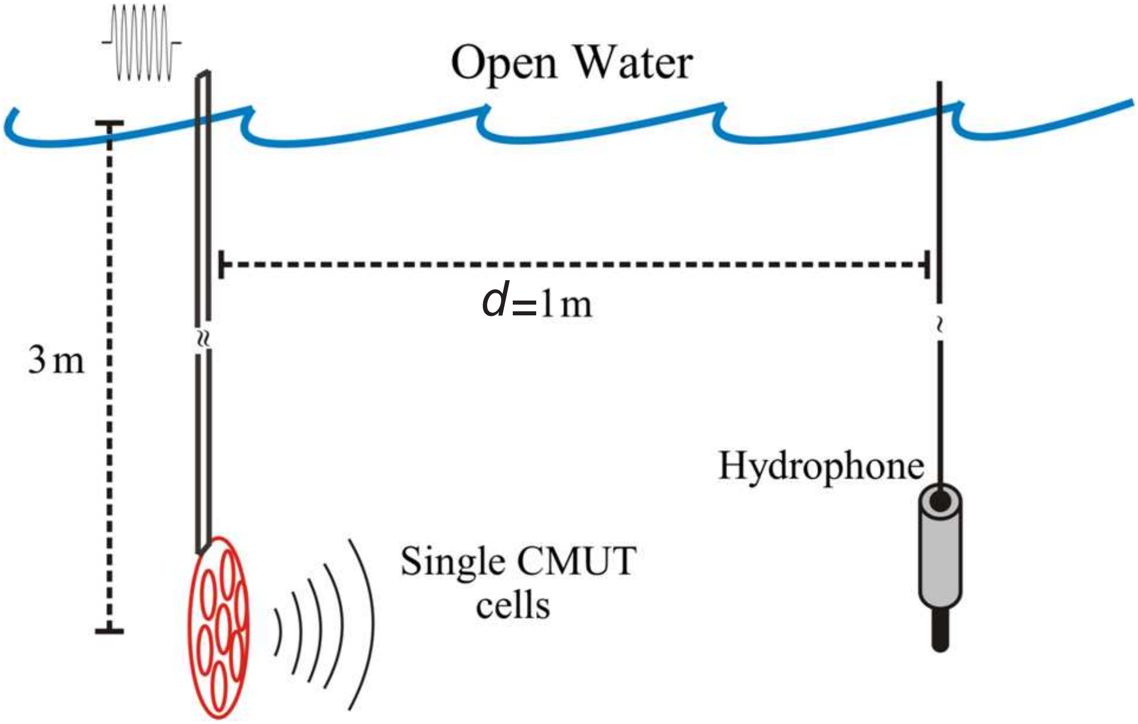

Figure B.3: A schematic of the experimental setup used for underwater experiments performed at Bilkent University Lake.

B.3 Underwater Experiments

Underwater performances of the CMUT cells are tested in our open water testing facility on Bilkent University Lake. The a diagram of the experimental setup is seen in Fig. B.3. CMUTs are driven with multiple cycles bursts of sinusoids amplified by a power amplifier. The signal generated from the signal source (SRS DS345) is amplified (20dB) by a power amplifier (Krohn-Hite 7500). The radiated acoustical energy is detected by a calibrated hydrophone (Neptune D70H).

The frequency response of CMUT cells has been determined by use of testing software running on LabView. The hydrophone is kept at approximately 1 m away from the radiating CMUTs. The received signal is corrected with the calibration data of the hydrophone.

B.3.1 Calibration

We represent the sensitivity of the hydrophone used in the experiments as a function of frequency as H_S with the units of decibels relative to 1 V/μPa. Therefore the source pressure level (SPL) at position of the hydrophone is defined as a function of pressure:

$$\text{SPL} = 20 \log \left(\frac{P_{rms}}{1\mu\text{Pa}} \right) \tag{B.11}$$

where, P_{rms} is the root mean square pressure generated by the source at the hydrophone location with the units of Pascal an is expressed as:

$$P_{rms} = \frac{V_{rms}}{10^{H_S/20}} \times \frac{1}{10^{G_A/20}} \times 1\mu\text{Pa} \quad (\text{Pa}) \tag{B.12}$$

Therefore, SPL in terms of the electrical parameters is expressed as:

$$\text{SPL} = 20 \log(V_{rms}) - H_S - G_A \qquad (\text{dB re. } 1\mu\text{Pa}) \tag{B.13}$$

where V_{rms} is the root mean square of the detected electrical signal at the oscilloscope and G_A is the gain of the amplifier between the hydrophone and the oscilloscope in decibels. SPL has the units of debicels relative to 1 μPa.

The performance of a source is quantified by the amount of pressure generated relative to a reference pressure in decibels at a unit distance, which is called the source level (SL). We shall calculate the sound pressure level at 1 m in order to find the source level as:

$$\text{SL} = \text{SPL} + 20 \log(d) \qquad (\text{dB re. } 1\mu\text{Pa @ 1m}) \tag{B.14}$$

$$= 20 \log(V_{rms}) - H_S - G_A + 20 \log(d) \tag{B.15}$$

where d is the distance of the hydrophone to the source in meters as seen in Fig. B.3.

Usually, the performance of a transmitting transducer is quantified by the amount of pressure generated relative to a reference pressure in decibels at a unit distance when a unit voltage excitation is applied to the transducer. This quantification is called the transmit voltage response (TVR) and can be expressed as follows using the above expressions:

$$\text{TVR} = \text{SL} - 20 \log(V_{in}) \qquad (\text{dB re. } 1\mu\text{Pa/V @ 1m}) \tag{B.16}$$

$$= 20 \log(V_{rms}) - H_S - G_A + 20 \log(d) - 20 \log(V_{in}) \tag{B.17}$$

where, V_{in} is the root mean square of the input excitation voltage.

We shall note here that the expressions above are valid for sinusoidal acoustic and electrical signals. Therefore they can be used for the measurement when a continuous wave excitation or a burst excitation at the source is utilized. For a measurement, where there is a pulsed excitation at the source, a correction method similar to that discussed in Appendix B.2.1 should be used.

Nomenclature

α	Attenuation factor
ϵ_0	Permittivity of free space
ϵ_r	Relative permittivity
γ	Ratio of the maximum of an input excitation voltage to the collapse voltage
κ	Correction factor due to lumped displacement measures
λ	Wavelength of an acoustic wave in the immersion medium
ν	Poisson's ratio
ω	Angular frequency
ρ	Density
ρ_0	Density of the medium, where CMUT is coupled to
A	Total radius of an array of CMUT cells
a	Radius of a circular CMUT membrane
A_1	Multiplier of the attenuation factor
a_i	Radial distance of a point force, F_i from the center of a circular membrane
A_L	Attenuation loss
b	Contact radius of a collapsed CMUT membrane

C	Input capacitance of a deflected CMUT cell
C_0	Input capacitance of an undeflected CMUT cell
c_0	Speed of sound in the medium, where CMUT is coupled to
C_A	Input capacitance of an amplifier
C_C	Capacitance of the connector between a hydrophone and an amplifier
C_H	Input capacitance of an hydrophone
C_S	Sensitivity of a CMUT receiver
D	Flexural rigidity of a CMUT membrane
d	Distance between the source and the receiver in an acoustic experiment
D_L	Diffraction loss
E	Young's modulus
E_k	Kinetic energy of a CMUT membrane
E_p	Potential energy stored in a deflected CMUT membrane
E_{brk}	Breakdown field of the insulation layer material
F	Lumped force on the membrane surface
F_e	Lumped electrical attraction force on a CMUT membrane
F_i	Electrical attraction force between the electrodes at a radial distance, a_i
F_r	Lumped restoring force generated by a deflected CMUT membrane
f_r	Resonance frequency of a CMUT membrane in vacuum
F_{atm}	Force generated by atmospheric pressure on a CMUT membrane
F_{net}	Net total force generated on a CMUT membrane
G_A	Gain of an amplifier

H_S	Sensitivity of a hydrophone
H_T	Sensitivity of a hydrophone including the effects of amplification and loading
L_m	Inductance representing the mass of a CMUT membrane in an eq. circuit
m	Mass of a CMUT membrane
n	Exponent of the attenuation factor
P	Uniform pressure over a CMUT membrane
P_0	Atmospheric pressure
P_h	Spectrum of the pressure waveform at the location of a hydrophone
p_h	Pressure waveform at the location of a hydrophone
P_s	Spectrum of the pressure waveform at the surface of a CMUT transmitter
p_s	Pressure waveform at the surface of a CMUT transmitter
P_{out}	Average acoustical pressure at the surface of a CMUT
P_{rms}	RMS voltage recorded by a hydrophone
q_x	Charge, which represents the displacement in an equivalent circuit
r	Radial distance from the center of a CMUT membrane
R_0	Rayleigh distance
T	Intrinsic stress of a mechanical film
t_g	Height of the cavity underneath a CMUT membrane, gap height
t'_g	Effective gap height
t_i	Insulation layer thickness between the top and bottom electrodes of a CMUT
t_m	Thickness of a CMUT membrane
v	Velocity of a CMUT membrane

V_r	Spectrum of the voltage waveform reccorded by an oscilloscope
v_r	Voltage waveform recorded by an oscilloscope
V_{atm}	Voltage source representing the force generated by atmospheric pressure
v_{avg}	Average velocity of a CMUT membrane
V_{col}	Collapse voltage of a CMUT membrane
V_e	Controlled voltage source representing the electrical attraction force
V_{in}	Applied voltage signal to a CMUT
V_{max}	Maximum value of the amplitude of an input excitation voltage
V_{out}	Output voltage, voltage across Z_r of the transmit equivalent circuit
V_{rms}	RMS voltage recorded by an oscilloscope
v_{rms}	Root mean square velocity of a CMUT membrane
V_r	Controlled voltage source representing the restoring force
x	Displacement of a CMUT membrane
x_{avg}	Average displacement of a CMUT membrane
x_{rms}	Root mean square displacement of a CMUT membrane
Z_r	Radiation impedance seen by a CMUT
Z_{ring}	Radiation impedance of a ring shaped piston transducer
SiN_x	Silicon nitride deposited by a PECVD reactor
SL	Source Level of an acoustic source
SPL	Source Pressure Level of an acoustic source
t	Time

Bibliography

[1] M. I. Haller and B. T. Khuri-Yakub, “A surface micromachined electrostatic ultrasonic air transducer,” IEEE Trans. Ultrason., Ferroelect., Freq. Contr., vol. 43, pp. 1–6, 1996.

[2] M. I. Haller and B. T. Khuri-Yakub, “A surface micromachined electrostatic ultrasonic air transducer,” in Proc. IEEE Ultrason. Symp., pp. 1241–1244, 1994.

[3] I. Ladabaum, B. T. Khuri-Yakub, and M. I. H. D. Spoliansky, “Micromachined ultrasonic transducers (muts),” in Proc. IEEE Ultrason. Symp., pp. 501–504, 1995.

[4] X. Jin, I. Ladabaum, and B. T. Khuri-Yakub, “The microfabrication of capacitive micromachined ultrasonic transducers,” J. Microelectromech. Syst., vol. 7, pp. 295–302, 1998.

[5] I. Ladabaum, X. Jin, H. T. Soh, A. Atalar, and B. T. Khuri-Yakub, “Surface micromachined capacitive ultrasonic transducers,” IEEE Trans. Ultrason., Ferroelect., Freq. Contr., vol. 45, pp. 678–690, 1998.

[6] R. A. Noble, R. R. Davies, M. M. Day, L. Koker, D. O. King, K. M. Brunson, A. R. D. Jones, J. S. McIntosh, D. A. Hutchins, T. J. Robertson, and P. Saul, “A cost-effective and manufacturable route to the fabrication of high-density 2D micromachined ultrasonic transducer arrays and CMOS signal conditioning electronics on the same silicon substrate,” in Proc. IEEE Ultrason. Symp., pp. 941–945, 2001.

[7] R. A. Noble, R. R. Davies, D. O. King, M. M. Day, A. R. D. Jones, J. S. McIntosh, D. A. Hutchins, and P. Saul, "Low-temperature micromachined cMUTs with fully-integrated analogue front-end electronics," in Proc. IEEE Ultrason. Symp., pp. 1045–1050, 2002.

[8] C. Daft, S. Calmes, D. Graca, K. Patel, P. Wagner, and I. Ladabaum, "Microfabricated ultrasonic transducers monolithically integrated with high voltage electronics," in Proc. IEEE Ultrason. Symp., pp. 493–496, 2004.

[9] A. S. Ergun, Y. Huang, X. Zhuang, O. Oralkan, G. G. Yaralioglu, and B. T. Khuri-Yakub, "Capacitive micromachined ultrasonic transducers: fabrication technology," IEEE Trans. Ultrason., Ferroelect., Freq. Contr., vol. 52, pp. 2242–2258, 2005.

[10] Y. Huang, A. S. Ergun, E. Hæggström, M. H. Badi, and B. T. Khuri-Yakub, "Fabricating capacitive micromachined ultrasonic transducers with wafer-bonding technology," J. Microelectromech. Syst., vol. 12, pp. 128–137, 2003.

[11] MEMSCAP SA., Cedex, France.

[12] J. Liu, C. Oakley, and R. Shandas, "Capacitive micromachined ultrasonic transducers using commercial multi-user MUMPs process: Capability and limitations," Ultrasonics, vol. 49, pp. 765–773, 2009.

[13] I. J. Oppenheim, A. Jain, and D. W. Greve, "MEMS ultrasonic transducers for the testing of solids," IEEE Trans. Ultrason., Ferroelect., Freq. Contr., vol. 50, pp. 305–311, 2003.

[14] I. J. Oppenheim, A. Jain, and D. W. Greve, "Electrical characterization of coupled and uncoupled MEMS ultrasonic transducers," IEEE Trans. Ultrason., Ferroelect., Freq. Contr., vol. 50, pp. 297–304, 2003.

[15] E. Cianci, A. Schina, A. Minotti, and S. Q. V. A. Foglietti, "Dual frequency PECVD silicon nitride for fabrication of CMUTs' membranes," Sens. Act. A., vol. 127, pp. 80–87, 2006.

[16] M. Mikolajunas, R. Kaliasas, M. Andrulevicius, V. Grigaliunas, J. Baltrusaitis, and D. Virzonis, "A study of stacked PECVD silicon nitride films used for surface micromachined membranes," Thin Solid Films, vol. 23, pp. 8788–8792, 2008.

[17] J. Knight, J. McLean, and F. L. Degertekin, "Low temperature fabrication of immersion capacitive micromachined ultrasonic transducers on silicon and dielectric substrates," IEEE Trans. Ultrason., Ferroelect., Freq. Contr., vol. 51, pp. 1324–1333, 2004.

[18] B. Belgacem, D. Alquier, P. Muralt, J. Baborowski, S. Lucas, and R. J. R, "Optimization of the fabrication of sealed capacitive transducers using surface micromachining," J. Micromech. Microeng., vol. 14, pp. 299–304, 2003.

[19] K. K. Park, H. J. Lee, P. Crisman, M. Kupnik, Ö. Oralkan, and B. T. Khuri-Yakub, "Optimum design of circular cmut membranes for high quality factor in air," in Proc. IEEE Ultrason. Symp., pp. 504–507, 2008.

[20] B. T. Khuri-Yakub, K. K. Park, H. J. Lee, G. G. Yaralioglu, S. E. O. Oralkan, M. Kupnik, C. F. Quate, T. Braun, H. P. Lang, M. Hegner, J. P. Ramseyer, C. Gerber, and J. Gimzewski, "The capactive micromachined ultrasonic transducer (CMUT) as a Chem/Bio sensor," in Proc. IEEE Ultrason. Symp., pp. 472–475, 2007.

[21] A. Bozkurt, I. Ladabaum, A. Atalar, and B. T. Khuri-Yakub, "Theory and analysis of electrode size optimization for capacitive microfabricated ultrasonic transducers," IEEE Trans. Ultrason., Ferroelect., Freq. Contr., vol. 46, pp. 1364–1374, 1999.

[22] R. O. Guldiken, J. McLean, and F. L. Degertekin, "CMUTs with dual-electrode structure for improved transmit and receive performance," IEEE Trans. Ultrason., Ferroelect., Freq. Contr., vol. 53, pp. 483–491, 2006.

[23] R. O. Guldiken, J. Zahorian, F. Y. Yamaner, and F. L. Degertekin, "Dual-electrode CMUT with non-uniform membranes for high electromechanical coupling coefficient and high bandwidth operation," IEEE Trans. Ultrason., Ferroelect., Freq. Contr., vol. 56, pp. 1270–1276, 2009.

[24] Y. L. Huang, X. F. Zhuang, E. O. Haeggstrom, A. S. Ergun, C. H. Cheng, and B. T. Khuri-Yakub, "Capacitive micromachined ultrasonic transducers with piston-shaped membranes: Fabrication and experimental characterization," IEEE Trans. Ultrason., Ferroelect., Freq. Contr., vol. 56, pp. 136–145, 2009.

[25] A. Logan and J. T. W. Yeow, "Fabricating capacitive micromachined ultrasonic transducers with a novel silicon-nitride-based wafer bonding process," IEEE Trans. Ultrason., Ferroelect., Freq. Contr., vol. 56, pp. 1074–1084, 2009.

[26] M. Kupnik, S. Vaithilingam, K. Torashima, I. O. Wygant, and B. T. Khuri-Yakub, "Cmut fabrication based on a thick buried oxide layer," in Proc. IEEE Ultrason. Symp., 2010.

[27] I. O. Wygant, X. Zhuang, D. T. Yeh, Ö. Oralkan, A. S. Ergun, M. Karaman, and B. T. Khuri-Yakub, "Integration of 2D CMUT arrays with front-end electronics for volumetric ultrasound imaging," IEEE Trans. Ultrason., Ferroelect., Freq. Contr., vol. 55, pp. 327–342, 2008.

[28] X. F. Zhuang, I. O. Wygant, D. S. Lin, M. Kupnik, O. Oralkan, and B. T. Khuri-Yakub, "Wafer-bonded 2-D CMUT arrays incorporating through-wafer trench-isolated interconnects with a supporting frame," IEEE Trans. Ultrason., Ferroelect., Freq. Contr., vol. 55, pp. 182–192, 2009.

[29] A. Nikoozadeh, I. O. Wygant, D. Lin, O. Oralkan, A. S. Ergun, D. N. Stephensen, K. E. Thomenius, A. M. D. D. Wildes, G. Akopyan, K. Shivkumar, A. Mahajan, D. J. Sahn, and B. T. Khuri-Yakub, "Forward-looking intercardiac ultrasound imaging using a 1-D CMUT array integrated with custom front-end electroncis," IEEE Trans. Ultrason., Ferroelect., Freq. Contr., vol. 55, pp. 2651–2660, 2008.

[30] X. Zhuang, D.-S. Lin, Ö. Oralkan, and B. T. Khuri-Yakub, "Fabrication of flexible transducer arrays with through-wafer electrical interconnects based on trench refilling with PDMS," J. Microelectromech. Syst., vol. 17, pp. 446–452, 2008.

[31] Ö. Oralkan, A. S. Ergun, J. A. Jhonson, M. Karaman, U. Demirci, K. Kaviani, T. H. Lee, and B. T. Khuri-Yakub, "Capacitive micromachined ultrasonic transducers: Next-generation arrays for acoustic imaging?," IEEE Trans. Ultrason., Ferroelect., Freq. Contr., vol. 49, pp. 1596–1610, 2002.

[32] Ö. Oralkan, A. S. Ergun, C.-H. Cheng, J. A. Jhonson, M. Karaman, T. H. Lee, and B. T. Khuri-Yakub, "Volumetric ultrasound imaging using 2-D cMUT arrays," IEEE Trans. Ultrason., Ferroelect., Freq. Contr., vol. 50, pp. 1581–1594, 2003.

[33] U. Demirci, A. S. Ergun, Ö. Oralkan, M. Karaman, and B. T. Khuri-Yakub, "Forward-viewing CMUT arrays for medical imaging," IEEE Trans. Ultrason., Ferroelect., Freq. Contr., vol. 51, pp. 886–894, 2004.

[34] G. Caliano, R. Carotenuto, E. Cianci, V. Foglietti, A. Caronti, A. Iula, and M. Pappalardo, "Design, fabrication and characterization of a capacitive micromachined ultrasonic probe for medical imaging," IEEE Trans. Ultrason., Ferroelect., Freq. Contr., vol. 52, pp. 2259–2269, 2005.

[35] A. Caronti, G. Caliano, R. Carotenuto, A. Savoia, M. Pappalardo, E. Cianci, and V. Foglietti, "Capacitive micromachined ultrasonic transducer (CMUT) arrays for medical imaging," Microelect. J., vol. 37, pp. 770–777, 2006.

[36] I. O. Wygant, N. S. Jamal, H. J. Lee, A. Nikoozadeh, Ö. Oralkan, M. Karaman, and B. T. Khuri-Yakub, "An integrated circuit with transmit beamforming flip-chip bonded to a 2-D CMUT array for 3-D ultrasound imaging," IEEE Trans. Ultrason., Ferroelect., Freq. Contr., vol. 56, pp. 2145–2156, 2009.

[37] S. H. Wong, R. D. Watkins, M. Kupnik, K. B. Pauly, and B. T. Khuri-Yakub, "Feasibility of MR-temperature mapping of ultrasonic heating from a CMUT," IEEE Trans. Ultrason., Ferroelect., Freq. Contr., vol. 55, pp. 811–818, 2008.

[38] S. H. Wong, M. Kupnik, R. D. Watkins, K. Butts-Pauly, and B. T. Khuri-Yakub, "Capacitive micromachined ultrasonic transducers for therapeutic ultrasound applications," IEEE Trans. Ultrason., Ferroelect., Freq. Contr., vol. 57, pp. 114–123, 2010.

[39] F. L. Degertekin, R. O. Guldiken, and M. Karaman, “Annular-ring cmut arrays for forward-looking ivus: transducer characterization and imaging,” IEEE Trans. Ultrason., Ferroelect., Freq. Contr., vol. 53, pp. 474–482, 2006.

[40] D. T. Yeh, Ö. Oralkan, I. O. Wygantand, M. O’Donnel, and B. T. Khuri-Yakub, “3-D ultrasound imaging using a forward-looking CMUT ring array for intravascular/intercardiac applications,” IEEE Trans. Ultrason., Ferroelect., Freq. Contr., vol. 53, pp. 1202–1211, 2006.

[41] D. N. Stephens, M. O’Donnell, K. Tomenius, A. Dentinger, D. Wildes, P. Chen, K. K. Shung, J. Cannata, B. T. Khuri-Yakub, O. Oralkan, A. Mahajan, K. Shivkumar, and D. J. Sahn, “Experimental studues with a 9f forward-looking intercardiac imaging and ablation catheter,” J. Ultrason. in Med., vol. 28, pp. 207–215, 2009.

[42] W. Liu, J. A. Zagzebski, T. J. Hall, E. L. Madsen, T. Varghese, M. A. Kliewer, S. Panda, C. Lowery, and S. Barnes, “Acoustic backscatter and effective scatterer size estimates using a 2D CMUT transducer,” Phys. Med. Bio., vol. 53, pp. 4169–4183, 2008.

[43] J. K. Chen, X. Y. Cheng, C. C. Chen, P. C. Li, J. H. Liu, and Y. T. Cheng, “A capacitive micromachined ultrasonic transducer array for minimally invasive medical diagnosis,” J. Microelectromech. Syst., vol. 17, pp. 599–610, 2008.

[44] J. K. Chen, “Capacitive micromachined ultrasonic transducer arrays for minimally invasive medical ultrasound,” J. Micromech. Microeng., vol. 20, p. 023001, 2010.

[45] X. Y. Cheng, J. K. Chen, and C. A. Li, “A miniature capacitive micromachined ultrasonic transducer array for minimally invasive photoacoustic imaging,” J. Microelectromech. Syst., vol. 19, pp. 1002–1011, 2010.

[46] S. Vaithilingam, T. J. Ma, Y. Furukawa, I. O. Wygant, X. F. Zhuang, A. D. la Zerda, Ö. Oralkan, A. Kamaya, S. S. Gambhir, R. B. Jeffrey, and B. T. Khuri-Yakub, “Three-dimensional photoacoustic imaging using a two-dimensional CMUT array,” IEEE Trans. Ultrason., Ferroelect., Freq. Contr., vol. 56, pp. 2411–2419, 2009.

[47] T. G. Fisher, T. J. Hall, S. Panda, M. S. Richards, P. E. Barbone, J. F. Jiang, J. Resnick, and S. Barnes, "Volumetric elasticity imaging with a 2-D CMUT array," Ultrasound Med. Bio., vol. 36, pp. 978–990, 2010.

[48] I. O. Wygant, M. Kupnik, J. C. Windsor, W. M. Wright, M. S. Wochner, G. G. Yaralioglu, M. F. Hamilton, and B. T. Khuri-Yakub, "50 kHz capacitive micromachined ultrasonic transducers for generation of highly directional sound with parametric arrays," IEEE Trans. Ultrason., Ferroelect., Freq. Contr., vol. 56, pp. 193–203, 2009.

[49] S. T. Hansen, A. S. Ergun, W. Liou, B. A. Auld, and B. T. Khuri-Yakub, "Wideband micromachined capacitive microphones with radio frequency detection," J. Acst. Soc. Am., vol. 116, pp. 828–842, 2004.

[50] Personal communication with Dr. Christophe Antoine, Analog Devices Inc., Boston, MA, USA, 2010.

[51] S. H. Wong, M. Kupnik, X. Zhuang, D.-S. Lin, K. Butts-Pauly, and B. T. Khuri-Yakub, "Evaluation of wafer bonded CMUTs with rectangular membranes featuring high fill factor," IEEE Trans. Ultrason., Ferroelect., Freq. Contr., vol. 55, pp. 2053–2065, 2008.

[52] B. Bayram, Ö. Oralkan, A. S. Ergun, E. Hæggström, G. G. Yaralioglu, and B. T. Khuri-Yakub, "Capacitive micromachined ultrasonic transducer design for high power transmission," IEEE Trans. Ultrason., Ferroelect., Freq. Contr., vol. 52, pp. 326–339, 2005.

[53] Ö. Oralkan, B. Bayram, G. G. Yaralioglu, A. S. Ergun, M. Kupnik, D. T. Yeh, I. O. Wygant, and B. T. Khuri-Yakub, "Experimental characterization of collapse-mode CMUT operation," IEEE Trans. Ultrason., Ferroelect., Freq. Contr., vol. 53, pp. 1513–1523, 2006.

[54] Y. Huang, E. Hæggstrom, B. Bayram, X. Zhuang, A. S. Ergun, C.-H. Cheng, and B. T. Khuri-Yakub, "Comparison of conventional and collapsed region operation of capacitive micromachined ultrasonic transducers," IEEE Trans. Ultrason., Ferroelect., Freq. Contr., vol. 53, pp. 1918–1932, 2006.

[55] B. Bayram, G. G. Yaralioglu, M. Kupnik, A. S. Ergun, Ö. Oralkan, A. Nikoozadeh, and B. T. Khuri-Yakub, "Dynamic analysis of capacitive micromachined ultrasonic transducers," IEEE Trans. Ultrason., Ferroelect., Freq. Contr., vol. 52, pp. 2270–2275, 2005.

[56] W. P. Mason, Electromechanical Transducers and Wave Filters. Van Nostrand, New York, 1942.

[57] H. K. Oguz, S. Olcum, M. N. Senlik, V. Tas, A. Atalar, and H. Köymen, "Nonlinear modeling of an immersed transmitting capacitive micromachined ultrasonic transducer for harmonic balance analysis," IEEE Trans. Ultrason., Ferroelect., Freq. Contr., vol. 57, pp. 438–447, 2010.

[58] S. Olcum, M. N. Senlik, and A. Atalar, "Optimization of the gain-bandwidth product of capacitive micromachined ultrasonic transducers," IEEE Trans. Ultrason., Ferroelect., Freq. Contr., vol. 52, pp. 2211–2219, 2005.

[59] H. Köymen, M. N. Senlik, A. Atalar, and S. Olcum, "Parametric linear modeling of circular CMUT membranes in vacuum," IEEE Trans. Ultrason., Ferroelect., Freq. Contr., vol. 54, pp. 1229–1239, 2007.

[60] A. Lohfink and P. C. Eccardt, "Linear and nonlinear equivalent circuit modeling of CMUTs," IEEE Trans. Ultrason., Ferroelect., Freq. Contr., vol. 52, pp. 2163–2172, 2005.

[61] A. Caronti, G. Caliano, A. Iula, and M. Pappalardo, "An accurate model for capacitive micromachined ultrasonic transducers," IEEE Trans. Ultrason., Ferroelect., Freq. Contr., vol. 49, pp. 159–167, 2002.

[62] G. Caliano, A. Caronti, M. Baruzzi, A. Rubini, A. Iula, R. Carotenuto, and M. Pappalardo, "PSpice modeling of capacitive microfabricated ultrasonic transducers," Ultrasonics, vol. 40, pp. 449–455, 2002.

[63] X. Jin, Ö. Oralkan, F. L. Degertekin, and B. T. Khuri-Yakub, "Characterization of one-dimensional capacitive micromachined ultrasonic immersion transducer arrays," IEEE Trans. Ultrason., Ferroelect., Freq. Contr., vol. 48, pp. 750–759, 2001.

[64] M. Buigas, F. M. Espinosa, G. Schmitz, I. Ameijeiras, P. Masegosa, and M. Dominguez, "Electro-acoustical characterization procedure for cMUTs," Ultrasonics, vol. 5, pp. 383–390, 2005.

[65] G. G. Yaralioglu, A. S. Ergun, and B. T. Khuri-Yakub, "Finite-element analysis of capacitive micromachined ultrasonic transducers," IEEE Trans. Ultrason., Ferroelect., Freq. Contr., vol. 52, pp. 2185–2198, 2005.

[66] B. Bayram, E. Hæggström, G. G. Yaralioglu, and B. T. Khuri-Yakub, "A new regime for operating capacitive micromachined ultrasonic transducers," IEEE Trans. Ultrason., Ferroelect., Freq. Contr., vol. 50, pp. 1184–1190, 2003.

[67] M. N. Senlik, S. Olcum, H. Köymen, and A. Atalar, "Radiation impedance of an array of circular capacitive micromachined ultrasonic transducers," IEEE Trans. Ultrason., Ferroelect., Freq. Contr., vol. 57, pp. 969–976, 2010.

[68] A. Caronti, A. Savoia, G. Caliano, and M. Pappalardo, "Acoustic coupling in capacitive microfabricated ultrasonic transducers: Modeling and experiments," IEEE Trans. Ultrason., Ferroelect., Freq. Contr., vol. 52, pp. 2220–2234, 2005.

[69] V. Bavaro, G. Caliano, and M. Pappalardo, "Element shape design of 2-D CMUT arrays for reducing grating lobes," IEEE Trans. Ultrason., Ferroelect., Freq. Contr., vol. 55, pp. 308–318, 2008.

[70] B. Bayram, M. Kupnik, G. G. Yaralioglu, O. Oralkan, D. Lin, X. Zhuang, A. S. Ergun, A. F. Sarioglu, S. H. Wong, and B. T. Khuri-Yakub, "Characterization of cross-coupling in capacitive micromachined ultrasonic transducers," in Proc. IEEE Ultrason. Symp., pp. 601–604, 2005.

[71] B. Bayram, G. G. Yaralioglu, M. Kupnik, and B. T. Khuri-Yakub, "Acoustic crosstalk reduction method for cmut arrays," in Proc. IEEE Ultrason. Symp., pp. 590–593, 2006.

[72] S. Ballandras, M. Wilm, W. Daniau, A. Reinhardt, V. Laude, and R. Armati, "Periodic finite element/boundary element modeling of capacitive micromachined ultrasonic transducers," J. Appl. Phys., vol. 97, p. 034901, 2005.

[73] A. Novell, M. Legros, N. Felix, and A. Bouakaz, “Exploitation of capacitive micromachined transducers for nonlinear ultrasound imaging,” IEEE Trans. Ultrason., Ferroelect., Freq. Contr., vol. 56, pp. 2733–2743, 2009.

[74] G. G. Yaralioglu, A. S. Ergun, B. Bayram, E. Hæggström, and B. T. Khuri-Yakub, “Calculation and measurement of electromechanical coupling coefficient of capacitive micromachined ultrasonic transducers,” IEEE Trans. Ultrason., Ferroelect., Freq. Contr., vol. 50, pp. 449–456, 2003.

[75] A. Caronti, R. Carotenuto, and M. Pappalardo, “Electromechical coupling factor of capacitive micromachined ultrasonic transducers,” J. Acoust. Soc. Am., vol. 113, pp. 279–288, 2003.

[76] A. Caronti, E. Carotenuto, G. Caliano, and M. Pappalardo, “The effects of membrane metallization in capacitive microfabricated ultrasonic transducers,” J. Acoust. Soc. Am. , vol. 115, pp. 651–657, 2004.

[77] D. Certon, F. Teston, and F. Patat, “A finite difference model for cmut devices,” IEEE Trans. Ultrason., Ferroelect., Freq. Contr., vol. 52, pp. 2199–2210, 2005.

[78] I. O. Wygant, M. Kupnik, and B. T. Khuri-Yakub, “Analytically calculating membrane displacement and the equivalent circuit model of a circular cmut cell.,” in Proc. IEEE Ultrason. Symp., pp. 2111–2114, 2008.

[79] S. Timoshenko and S. Woinowsky-Krieger, Theory of Plates and Shells. New York: McGraw Hill, second ed., 1959.

[80] H. K. Oğuz, “Nonlinear modelling of an immersed transmitting capacitive micromachined ultrasonic transducer for harmonic balance analysis,” Master’s thesis, Bilkent University, 2010.

[81] A. Nikoozadeh, B. Bayram, G. G. Yaralioglu, and B. T. Khuri-Yakub, “Analytical calculation of collapse voltage of cMUT membrane,” in Proc. IEEE Ultrason. Symp., pp. 256–259, 2004.

[82] P. R. Stepanishen, “Impulse response and radiation impedance of an annular piston,” J. Acoust. Soc. Am., vol. 56, pp. 305–312, 1974.

[83] J. M. Bustillo, R. T. Howe, and R. S. Muller, "Surface micromachining for microelectromechanical systems," Proc. IEEE, vol. 86, pp. 1552–1574, 1998.

[84] N. Tas, T. Sonnenberg, H. Jansen, R. Legtenberg, and M. Elwenspoek, "Stiction in surface micromachining," J. Micromech. Microeng., vol. 6, pp. 385–397, 1996.

[85] C. H. Ng, K. W. Chew, and S. F. Chu, "Characterization and comparison of PECVD silicon nitride and silicon oxynitride dielectric for MIM capacitors," IEEE Elect. Dev. Lett., vol. 24, pp. 506–508, 2003.

[86] Y. L. Huang, E. O. Haeggstrom, X. F. Zhuang, A. S. Ergun, and B. T. Khuri-Yakub, "A solution to the charging problems in capacitive micromachined ultrasonic transducers," IEEE Trans. Ultrason., Ferroelect., Freq. Contr., vol. 52, pp. 578–580, 2005.

[87] K. Midtbo and A. Ronnekleiv, "Analysis of charge effects in high frequency CMUTs," in Proc. IEEE Ultrason. Symp., pp. 379–382, 2008.

[88] H. Martinussen, A. Aksnes, and H. E. Engan, "Investigation of charge diffusion in CMUTs using optical interfermetry," in Proc. IEEE Ultrason. Symp., pp. 1218–1221, 2008.

[89] S. Machida, S. Migitaka, H. Tanaka, K. Hashiba, H. Enomoto, Y. Tadaki, and T. Kobayashi, "Analysis of the charging problem in capacitive micro-machined ultrasonic transducers," in Proc. IEEE Ultrason. Symp., pp. 383–385, 2008.

[90] K. M. Knowles and A. T. J. van Helvoort, "Anodic bonding," Int. Mat. Rev., vol. 51, pp. 273–311, 2006.

[91] W. P. Shih, C. Y. Hui, and N. C. Tien, "Collapse of microchannels during anodic bonding: Theory and experiments," J. Appl. Phys., vol. 95, pp. 2800–2808, 2004.

[92] G. S. Kino, Acoustic Waves: Devices, Imaging, and Analog Signal Processing. New York: Englewood Cliffs, NJ: Prentice Hall, 1987.

[93] R. Chanamai and D. J. McClements, "Ultrasonic attenuation of edible oils," J. Amer. Oil. Chem., vol. 75, pp. 1447–1448, 1998.